Observational constraints on dark energy parameters

A thesis
submitted by

Archana Sangwan

in partial fulfillment of
the requirements for the degree of

Doctor of Philosophy

Indian Institute of Science Education and Research (IISER) Mohali

September, 2018

Certificate of Examination

This is to certify that the dissertation titled *Observational constraints on dark energy parameters* submitted by **Ms. Archana Sangwan** (Reg. No. PH12118) for the partial fulfillment of Doctor of Philosophy programme of the Institute, has been examined by the thesis committee duly appointed by the Institute.The committee finds the work done by the candidate satisfactory and recommends that the report be accepted.

Professor Sudeshna Sinha Professor Jasjeet Singh Bagla Dr. Harvinder Kaur Jassal

(Supervisor)

Declaration

The work presented in this dissertation has been carried out by me under the guidance of Dr. Harvinder Kaur Jassal at the Indian Institute of Science Education and Research Mohali.

This work has not been submitted in part or in full for a degree, a diploma, or a fellowship to any other university or institute. Whenever contributions of others are involved, every effort is made to indicate this clearly, with due acknowledgement of collaborative research and discussions. This thesis is a bonafide record of original work done by me and all sources listed within have been detailed in the bibliography.

Archana Sangwan

(Candidate)

In my capacity as the supervisor of the candidates doctoral thesis, I certify that the above statements by the candidate are true to the best of my knowledge.

Dr. Harvinder Kaur Jassal

(Supervisor)

Acknowledgements

I would like to express my deep gratitude and sincere thanks to my thesis supervisor, Dr. Harvinder Kaur Jassal, for her guidance and support in every step of my research work at Indian Institute of Science Education and Research, Mohali. I would also like to thank her for being supportive of every crazy idea that I had present her during our innumerable discussions. She has always emphasized on the development of intuitive understanding of a problem which has helped me look beyond the numbers and equations. Her curiosity and positive approach towards every problem has been a great source of motivation for me. I will always be grateful to her for this.

I am thankful to my doctoral committee members, Prof. Jasjeet Singh Bagla and Prof. Sudeshna Sinha for giving me invaluable time, support and sharing their knowledge. I am grateful to all the faculty members in the department of physical sciences for their direct and in-direct encouragement and support.

I am also thankful to IISER mohali for providing the financial support, high-performance computing facility, softwares and other resources useful for research.

No journey is fun without the a good company of friends. I would like to begin by thanking my friend and colleague, Ashutosh Tripathi who has helped me with both academic and non-academic problems and for expressing his genuine concern at various stages of my PhD. I would also like to thank my friend Shradha Gandhi who always acted like a sister and has been very supportive and kept on encouraging me throughout. My sincere thanks to all my friends Renu, Pranay, Chandrakala, Gaurav, Ashutosh (Tiwari), Richa, Khushbu and Nisha for moral support and making life at IISER lively and happily going. I also acknowledge my colleagues Sandeep, Ankit, Avinash, Manvendra, Ranbir, Ashish, Juhi, Ankan, Varinder and others for their moral support and delightful discussions.

Finally, I would like to thank my parents for always believing in me. All could have been possible only because of their unconditional love, care, support and patience. I especially want to thank my Mother for always being with me and my Father for providing me invaluable guidance. I shall be forever grateful to my elder sister, Kalpana and younger brother, Ankit for their amazing understanding and taking care of almost everything so that I could concentrate on my research.

Preface

Our universe is undergoing an accelerated expansion. This acceleration has been confirmed by various observations. The acceleration of the expansion is caused by a component of universe with negative pressure; this component is called *dark energy* which contributes to almost three-quarters of the total energy of the universe. How the dark energy came to be or the nature of dark energy is still a mystery, and is the most pertinent question in cosmology at present. In the lack of a fundamental theory explaining such a component, a large number of models have been proposed to explain dark energy.

The models include the cosmological constant which has had a history of being favoured and unfavoured. Observations, however, favour the cosmological constant model and this is also the most elegant explanation of dark energy. For a cosmological constant, the equation of state parameter is constant and is always equal to -1. Theoretically, this model suffers from the fine tuning problems, i.e., the value predicted from field theory vacuum energy is 121 orders of magnitude larger than the value required by observations. To circumvent this problem, many other models were proposed and have been studied in order to understand dark energy.

The condition for acceleration is that the ratio of pressure to energy density, which is equation of state parameter, must be $w = P/\rho \leq -1/3$. The equation of state parameter can be a constant or a function of time. It can be that of a barotropic fluid and within this description, the equation of state parameter can also be a function of time. Alternatively, scalar fields naturally have a negative equation of state parameter with the condition that the kinetic energy is subdominant to the potential energy. The potential dominated scalar field, requires a fine tuning of its own; the amplitude and the shape of the potential needs to be fine tuned. The work in this thesis focuses on studying fluid models of dark energy, and canonical scalar field models. We also attempt to reconcile the two different descriptions of dark energy by way of using parametric forms of dark energy to obtain information about the form of scalar field models.

To study these models, we first solve the cosmological equations for the models mentioned above and determine their respective parameters using different datasets. We focus mainly on the low redshift data constraints, namely Supernova type Ia data, Baryon Acoustic Oscillation data and direct measurements of Hubble parameter dataset. The constraints are based mainly on distance measurements, based on standard candles and standard rulers. We also check the consistency of constraints obtained with distant measurements namely the Cosmic Microwave Background (CMB) observations. We introduce

and review the Friedmann Robertson Walker (FRW) cosmology and distance measurements in the first chapter of the thesis.

In the second chapter, we study the fluid dark energy models in the context of present observations. We consider four different scenarios; a constant equation of state parameter of dark energy, and three different dramatization's of dark energy equation of state parameter, i.e., with a variable equation of state parameter. The case with a constant equation of state consists of two parameters (equation of state of dark energy, and matter density parameter) description of dark energy, and is called wCDM model. We have assumed the universe to be spatially flat, which is a reasonable assumption as CMB observations severely constrain the curvature to be very near flat. We show that the constraints are consistent with the ΛCDM model while a small range in the equation of state is allowed. The variable equation of state, is described by the present day value of the equation of state parameter and its first derivatives at present or a parameter of a function of the scale factor. We consider three different parametric forms, one with allows only a slow variation and becomes a constant at large redshifts (CPL parameterization), one which allows a large variation at low redshifts and reverts back to its original value at high redshift and one which increases slowly and monotonically as a function of redshift.

At lower redshifts, all the parameterizations are equivalent but at higher redshifts they show different behaviour in the evolution of equation of state parameters. The dark energy parameters are then constrained using different observations. We concentrate on dark energy equation of state parameter value and its evolution at low redshifts and study whether one functional form of the dark energy parameters is preferred over the others by observations. We find that the combined analysis from these datasets constrain the allowed range of parameters significantly. The constraints obtained from observations are consistent with a cosmological constant.

Scalar fields in cosmology provides another viable description of dark energy. In this case, equation of state parameter for the field changes as the field evolves. There are different types of scalar fields which have been introduced in extensive literature. We study the quintessence scalar field, which is a minimally coupled canonical scalar field. The equation of state parameter for quintessence is a function of time; the value of the equation of state parameter depends upon the functional form of the potential and the kinetic energy of the field. To obtain the accelerated expansion, the scalar field potential must be dominant over the kinetic energy. The scalar fields, in general, have been categorised into two broad classes depending upon the evolution of equation of state parameter; "freezing" and "thawing" scalar fields. In thawing case, at early times,

the scalar field is frozen at the initial state due to large Hubble damping term and the equation of state of the field is same as that of the cosmological constant. Very recently, when the Hubble damping decreases, the field begins to roll towards the minimum of the potential and the equation of state starts to deviate from that of a cosmological constant like equation of state. In the freezing behaviour, the field is already rolling towards the minimum of its potential and hence the kinetic energy term is non-zero. The scalar potential becomes shallower at later times and the field comes to a halt and kinetic term becomes negligible and the value of the equation of state parameter freezes. Using the same three different observations as before, i.e., type Ia supernova (SNIa) data, Baryonic Acoustic Oscillation(BAO) data and Hubble parameter (H(z)) data, we present constraints on the scalar field parameters in chapter 3.

In continuation, we reconcile the two above mentioned approaches to dark energy. In this work, we study the form of potentials which are consistent with different parameterizations mentioned in Chapter 2. We reconstruct the evolution of the scalar field associated with the canonical and phantom scalar field using current data considered above. we reconstruct the quintessence and phantom scalar field potentials and study the evolution of the scalar field as a function of scale factor. Then, using the three observations mentioned earlier, show the limits on the reconstructed potential and field parameters. We find that the wCDM model prefers a slow rolling potential and a tracker behaviour can not be accommodated in the reconstructed potential, for CPL and logarithmic dark energy equation of state. The quintessence and phantom class of dark energy tend to converge to a cosmological constant as the scale factor increases. In chapter 4, we study these aspects of dark energy.

The work in the thesis explores different aspects of dark energy, in the light of currently available observational datasets. In the lack of a fundamental theory, it is imperative to study different models of dark energy, and to constrain its parameter from observations. In this thesis, we obtain constraints on dark energy parameters in different scenarios using a diverse set of observations.

List of Publications

1) Ashutosh Tripathi, Archana Sangwan and H. K. Jassal, "Dark energy equation of state parameter and its evolution at low redshift," JCAP **1706**, no. 06, 012 (2017) [arXiv:1611.01899 [astro-ph.CO]].

2) Archana Sangwan, Ankan Mukherjee and H. K. Jassal, "Reconstructing the dark energy potential," manuscript submitted in JCAP, arXiv:1712.05143 [astro-ph.CO].

3) Archana Sangwan, A. Tripathi and H. K. Jassal, "Observational constraints on quintessence models of dark energy" arXiv:1804.09350 [astro-ph.CO].

Contents

Chapter 1

Introduction

Cosmology attempts to answer the questions related to the origin and evolution of the Universe and its properties at large scales. This branch of astronomy and astrophysics is based on the cosmological principle where one assumes a homogeneous and isotropic Universe at large scale. This leads to formulation of the standard model of cosmology. The standard cosmological model is well studied and is consistent with different observations. Observations have confirmed the standard model, and more and more observations have substantiated our understanding of the Universe. The observations are broadly based on distance measurements or based on observations of the large scale structures. Various surveys are currently on and are planned to further our understanding and to validate the standard model of cosmology to higher precision. Various unresolved issues remain. For instance, the nature of dark matter and dark energy are two such pertinent ones.

Dark energy derives the current acceleration of the Universe and is the most dominant component. A large amount of effort is going on to understand its nature. The attempts to understanding from high energy particle physics are largely unsuccessful as the energy scales are very low in the case of dark energy. Therefore, the approach to its understanding is phenomenological and is largely model building based. In this chapter we discuss the background cosmology, the Friedmann equations and solution of Friedmann equations for different scenarios. We also review a few viable models of dark energy.

This chapter is organised as follows. In the first section (1.1) we discuss the Friedmann-Robertson-Walker (FRW) metric that explains the homogeneous and isotropic Universe. In the second section (1.2), Einstein's field equations are explained which tell about the effect of gravity on a particle. The study of field equations require the understanding

of the concepts such as energy momentum tensor or stress tensor and the conservation of energy momentum tensor, which we discuss in detail in this section. In section three (1.3), we discuss the concept of redshift and the Hubble law. In fourth section (1.4), we discuss Friedmann equations and their solutions and in section (1.5), we focus on different types of distance measurements to the position of objects in the Universe such as the luminosity distance and the angular diameter distance. We then briefly review the current observations and how cosmological parameters are determined using the observational datasets.

1.1 Friedmann-Robertson-Walker (FRW) metric

Despite having high density structures (stars, galaxies etc.), at large scales the matter in the Universe is uniformly distributed. If we observe in any direction, the Universe appears to be the same. The structure of the Universe is identical in all the directions, i.e., there is no special direction, the Universe is isotropic. Isotropy at different points implies that the Universe is also homogeneous. The Universe will be the same no matter where the observer is located. These two properties together define the cosmological principle. In brief, the cosmological principle is stated as *'Universe is homogeneous and isotropic'*. We assume this principle to be true at large scales and so far, there is no observation which disproves this assumption.

The cosmological principle describes a highly symmetric Universe. In four dimensions, it is described by the Friedmann-Robertson-Walker (FRW) metric (also called Friedmann-Lematre-Robertson-Walker (FLRW)) which is a maximally symmetric metric in four dimensions. A metric, represented by a rank-2 tensor, is a mathematical quantity which tells us about the geometry of spacetime and its dynamics is described by Einstein's field equations, discussed in Sec. (1.2). In spherical co-ordinate system (t, r, θ, ϕ), the line element for FRW metric in comoving coordinates is given by

$$ds^2 = dt^2 - a^2(t)\left(\frac{1}{1-kr^2}dr^2 + r^2(d\theta^2 + \sin^2\theta d\phi^2)\right). \tag{1.1}$$

Here, cosmic time is represented by t and $a(t)$, called the scale factor, contains information about the nature of evolution of Universe i.e whether it is expanding or contracting. The scale factor is a function of time. Coordinates r, θ and ϕ are the comoving coordinates. The constant k determines the curvature of space. If $k = 0$, the FRW metric describes a spatially flat Universe (open and infinite), if $k = +1$, the Universe has positive curvature

(finite and closed Universe). If $k = -1$, then the metric describes a Universe with a negative curvature (infinite and open Universe). Comoving coordinates remain constant in an observer's frame i.e. an observer at rest will continue to be at rest in the comoving frame for all t. The scale factor, $a(t)$, describes the dynamics of the Universe.

1.2 Einstein's Field Equation

According to Einstein's General Relativity, the force of gravity is a result of the curvature introduced in spacetime due to matter and energy and it is governed by Einstein's field equations, a set of ten equations[1]. The Einstein field equation is

$$R_{\mu\nu} - \frac{1}{2}Rg_{\mu\nu} = \kappa^2 T_{\mu\nu} \tag{1.2}$$

where the metric tensor is denoted by the covariant tensor $g_{\mu\nu}$ and $R_{\mu\nu}$ represents Ricci tensor, $R = g^{\mu\nu}R_{\mu\nu}$ is called Ricci scalar which is a result of contraction of the Ricci tensor and the energy momentum tensor is denoted by $T_{\mu\nu}$ [2]. The energy momentum tensor describes the matter distribution in the Universe [3]; it contains all the information about mass, temperature, shear, momentum etc. In four dimensions, it is represented by a 4×4 matrix and, as it is symmetric, it has only ten independent components[4]. The constant, $\kappa^2 = \frac{8\pi G}{c^4}$ in natural units ($c = 1$ $\hbar = 1$). The tensor $g^{\mu\nu}$ is a contravariant metric tensor. Covariant and contravariant tensors are inverse of each other.

The right hand side of the equation contains information about energy and momentum density in the form of a symmetric tensor which is also conserved and the left hand side also has symmetric tensors which are obtained from $g_{\mu\nu}$ and its derivatives. We can also write this equation as

$$G_{\mu\nu} = \kappa^2 T_{\mu\nu} \tag{1.3}$$

where $G_{\mu\nu} = R_{\mu\nu} - \frac{1}{2}Rg_{\mu\nu}$ is called the Einstein's tensor. The field equation relates 4×4 tensors which are symmetric in nature and have ten independent components each.

1.2.1 Energy-Momentum Tensor

As explained above, the energy momentum tensor is represented by a 4×4 matrix, and, in general, it is given by

$$T^{\mu\nu} = \begin{pmatrix} T^{00} & T^{01} & T^{02} & T^{03} \\ T^{10} & T^{11} & T^{12} & T^{13} \\ T^{20} & T^{21} & T^{22} & T^{23} \\ T^{30} & T^{31} & T^{32} & T^{33} \end{pmatrix}. \tag{1.4}$$

It is a tensor of rank two, which has sixteen components in four dimensional spacetime. The component T^{00} represents the density of relativistic mass and is called the energy density. T^{0i} is the flux energy in x^i and i varies from 1 to 3. The components T^{i0} determine momentum density in directions i. The stress component with $i = j$, that is, T^{ii} denotes the pressure, which is the normal stress. When $i \neq j$, the components T^{ij} denotes the shear stress. As this tensor is symmetric, $T^{ij} = T^{ji}$ and $T^{i0} = T^{0i}$ (see [3], page 141). Therefore, we have only ten independent components representing the energy momentum tensor.

Vacuum: In vacuum, the components of the energy momentum tensor do not contribute, i.e.,

$$T^{\mu\nu} = 0 \tag{1.5}$$

and the Einstein's tensor vanishes. As, in the absence of any form of matter, there is nothing to cause gravitation and nothing to experience the effects of gravitation, therefore one can assume the gravitational field to be zero in vacuum.

Dust: It is a distribution of non-interacting particles of identical masses. There does not exist any internal motion, heat conduction or stress. Since these are non-interacting particles, it implies that they are electrically neutral so that there are no electrostatic forces influencing these particles. As these 'identical' particles have same rest mass, they must experience the gravitational force due to other particles. Since these particles are non-interacting, we assume that the particles are very small in size compared to the distance between them and the gravitational effects can be ignored. For this fluid, pressure is zero.

The energy momentum tensor for *dust* is given by

$$T^{\mu\nu} = \rho u^\mu u^\nu \tag{1.6}$$

here u^μ describes a tangent to the world lines of particles. If we consider the rest frame of

dust, then 4-velocity becomes $u^\mu = (1, 0, 0, 0)$ and the energy-momentum tensor becomes

$$T^{\mu\nu} = \begin{pmatrix} \rho & 0 & 0 & 0 \\ 0 & 0 & 0 & 0 \\ 0 & 0 & 0 & 0 \\ 0 & 0 & 0 & 0 \end{pmatrix}. \tag{1.7}$$

In earlier times, during matter domination era, dust was the main component of the Universe, which existed between radiation dominated era and the current dark energy dominated era.

Perfect fluid: An ideal fluid is characterised by the absence of heat conduction (which means $T^{i0} = T^{0i} = 0$) and no viscosity (implying $T^{ij} = 0$ if $i \neq j$) . Similar to *dust* particles, the particles in the fluid exhibit rest mass, but unlike *dust* particles, fluid particles also have internal motions and hence the pressure is non-zero. This fluid, in its rest frame, is described by its mass density ρ and a pressure P.

The energy momentum tensor for perfect fluid is

$$T^{\mu\nu} = (\rho + P)u^\mu u^\nu + P g^{\mu\nu} \tag{1.8}$$

In the rest frame of the fluid, $\mathrm{u}^\mu = (1, 0, 0, 0)$ and the energy momentum tensor can be rewritten as

$$T^{\mu\nu} = \begin{pmatrix} \rho & 0 & 0 & 0 \\ 0 & P & 0 & 0 \\ 0 & 0 & P & 0 \\ 0 & 0 & 0 & P \end{pmatrix}. \tag{1.9}$$

If there is no pressure or internal motion of particles, a perfect fluid becomes dust like. At earlier times, when the Universe was radiation dominant, the main component of the Universe was a perfect fluid which is characterized only by its mass density and by its pressure.

1.2.2 Conservation of Energy Momentum Tensor

The conservation equation is given as

$$\nabla_\alpha T^{\mu\nu} \equiv T^{\mu\nu}_{;\alpha} = 0. \tag{1.10}$$

This equation tells us about the conservation of energy and momentum both and for a flat spacetime it can be rewritten as

$$\frac{\partial T^{\mu\nu}}{\partial x^\alpha} = T^{\mu\nu}_{\alpha} = 0. \tag{1.11}$$

Energy Evolution: From the conservation law, Eq. (1.10), we can determine the evolution of components of the stress tensor. Let us consider the case of perfect fluid. The mixed energy momentum tensor in this case is given by

$$T^\mu_\nu = \begin{pmatrix} \rho & 0 & 0 & 0 \\ 0 & -P & 0 & 0 \\ 0 & 0 & -P & 0 \\ 0 & 0 & 0 & -P \end{pmatrix}. \tag{1.12}$$

The conservation equation for energy momentum tensor can be written as

$$\nabla_\mu T^\mu_\nu \equiv T^\mu_{\nu;\mu} \equiv T^\mu_{\nu,\mu} + \Gamma^\mu_{\alpha\mu} T^\alpha_\nu - \Gamma^\alpha_{\mu\nu} T^\mu_\alpha = 0, \tag{1.13}$$

which generates four separate equations. Using,

$$g_{\mu\nu} = \begin{pmatrix} 1 & 0 & 0 & 0 \\ 0 & -a(t)^2 & 0 & 0 \\ 0 & 0 & -a(t)^2 & 0 \\ 0 & 0 & 0 & -a(t)^2 \end{pmatrix}, \tag{1.14}$$

the FRW metric tensor for expanding flat spacetime and Christoffel symbols, we can find out how the components evolve. The Christoffel symbol ($\Gamma^\alpha_{\mu\nu}$) is defined as

$$\Gamma^\alpha_{\mu\nu} = \frac{1}{2} g^{\alpha\beta}(g_{\nu\beta,\mu} + g_{\beta\mu,\nu} - g_{\mu\nu,\beta}). \tag{1.15}$$

where g's represent the components of the metric. In case of $\nu = 0$ component, the equation becomes:

$$\frac{\partial T_0^\mu}{\partial x^\mu} + \Gamma^\mu_{\alpha\mu} T_0^\alpha - \Gamma^\alpha_{0\mu} T^\mu_\alpha = 0. \tag{1.16}$$

Since the Universe is assumed to be isotropic, the off-diagonal terms in the energy momentum tensor are zero, i.e. $T^{\mu\nu} = 0$ if $\mu \neq \nu$. The only term that contributes is T_0^0, and all other terms (T_0^1, T_0^2 and T_0^3) vanish. This implies that $\mu = 0$ in first term and $\alpha = 0$ in second term. Therefore,

$$\frac{\partial T_0^0}{\partial x^0} + \Gamma^\mu_{0\mu} T_0^0 - \Gamma^\alpha_{0\mu} T^\mu_\alpha = 0. \tag{1.17}$$

Coordinate x^0 is the time coordinate and T_0^0 is the energy density denoted by ρ. Therefore, we can write the above equation as

$$\frac{\partial \rho}{\partial t} + \Gamma^\mu_{0\mu} \rho - \Gamma^\alpha_{0\mu} T^\mu_\alpha = 0. \tag{1.18}$$

For the metric given in Eq. (1.14), the only surviving Christoffel symbols are $\Gamma^i_{0i} = \dot{a}/a$ for $i = 1, 2$ or 3, where a is the scale factor and $\dot{a}$ is the derivative of scale factor with time component.

$$\frac{\partial \rho}{\partial t} + 3\frac{\dot{a}}{a}\rho - \Gamma^\alpha_{0\mu} T^\mu_\alpha = 0 \tag{1.19}$$

Here, μ is a dummy index and can be replace by α. As only Γ^i_{0i} components contributes and $T^i_i = -P$, the above equation becomes

$$\frac{\partial \rho}{\partial t} + 3\frac{\dot{a}}{a}(\rho + P) = 0. \tag{1.20}$$

This equation describes the evolution of the Universe; how the energy density scales as a function of a depending upon the content of the Universe. For example, in the case of **non-relativistic (dust)** particles, the pressure is zero, the conservation equation (1.20) is

$$\frac{\partial \rho}{\partial t} + 3\frac{\dot{a}}{a}\rho = 0 \tag{1.21}$$

Integrating equation (1.21) will give

$$\rho_m = \rho_0 \left(\frac{a_0}{a}\right)^3 \tag{1.22}$$

where ρ_0 is the energy density at a_0 (the subscript '0' is used for values of different quantities at the present epoch). If we consider a_0 to be the value of scale factor at present then $a_0 = 1$. The subscript 'm' is for the nonrelativistic matter. The above equation (Eq. 1.22) implies that if the Universe consists of only matter then energy density of the Universe will scales as $\rho_m \propto a^{-3}$. As the number of particles, n_m, in the Universe is fixed and the volume of the Universe will scale as $V \propto a^3$, which gives $\rho_m = (n_m/V) \propto a^{-3}$ and the result remains the same.

For **relativistic** particles **(radiation)**, the pressure is one third of the energy density, $P = \rho/3$, which gives

$$\frac{\partial \rho}{\partial t} + 3\frac{\dot{a}}{a}(\rho + \rho/3) = 0 \tag{1.23}$$

On integration of this equation we have

$$\rho_R = \rho_0 \left(\frac{a_0}{a}\right)^4 \tag{1.24}$$

the subscript 'R' denotes radiation or relativistic matter. In this case, energy density evolves as $\rho_R \propto a^{-4}$. The volume of this Universe evolves in the same manner as in the case of nonrelativistic Universe, i.e., $V \propto a^3$. The difference in the evolution of energy density, when compared to energy density of non-relativistic matter, arises because of the nature of the particles. For relativistic particles, say photons, the energy is given by $E \propto h\nu \propto h/\lambda$. Therefore, energy density becomes $\rho_R \propto (h/V\lambda)$. As, λ is proportional to the scale factor, a, we have $\rho \propto a^{-4}$. The energy density of a Universe with radiation as its sole component decreases faster than a Universe which is composed of only non-relativistic matter.

So far we have discussed the energy density evolution in case of non-relativistic and relativistic matter. A generalized expression for any fluid with equation of state $P = P(\rho)$ is determined as follows. Consider a perfect fluid with $P = w\rho$, where w is the equation of state parameter. The energy conservation equation (Eq. 1.20) takes the form,

$$\frac{\partial \rho}{\partial t} + 3\frac{\dot{a}}{a}(\rho + w\rho) = 0 \tag{1.25}$$

and the energy density as a function of scale factor is given by

$$\rho = \rho_0 \left(\frac{a_0}{a}\right)^{3(1+w)} \tag{1.26}$$

These are the necessary elements required to understand Einstein's field equation to

understand the behaviour of particles under the influence of gravity and the gravitational effects of particles. For a particular stress-energy tensor, we can find out the metric tensor of that spacetime using Einstein's field equations.

1.3 Hubble's Law

In 1929, Edwin Hubble studied distances and the recession velocities of twenty-five galaxies and concluded that the galaxies are receding from us and this leads to the discovery that the Universe is expanding[5]. He found that these galaxies are moving away from each other at a speed that is proportional to the distance between them. This was discovered as a redshift in the galaxy spectra. Redshift of a galaxy tells about its radial velocity. The further away a galaxy is, faster it recedes and the larger is the redshift introduced in the spectrum. Consider a galaxy at a distance r from earth, it will move away with a velocity $v \propto r$, or

$$v = H_0 r \tag{1.27}$$

the proportionality constant H_0 is called the Hubble constant or Hubble parameter. At a particular time H assumes a value that is same at all points in space, in that sense it is a constant. It is more appropriate, therefore, to use the term Hubble parameter.

The Hubble parameter is a measure of the rate at which Universe is expanding and its units is time inverse. At present, $H(\text{present}) \equiv H_0$ and its value ranges between 65-75 $km/s/Mpc$ [6, 7]. This means that a galaxy which is 1Mpc away from us will be moving with a speed of 65-75 km/s. Although the receding velocity of a galaxy can be calculated from its redshifted spectrum, it is very difficult to measure the exact value of Hubble parameter today because of the uncertainty in measurements of distance to the galaxy. The inverse of the Hubble constant gives the age of Universe to be about 13 billion years.

The *Proper distance* is the actual or physical distance that separates two objects. It is represented as r as in Eq. (1.27). It changes with time as the Universe undergoes expansion. On the other hand, the *comoving distance* or the coordinate distance is not a function of time. In an expanding or a contracting Universe, it remains the same. It acts as label of points and is denoted by x. The relation between physical distance and the comoving distance is given by

$$r(t) = a(t)x \tag{1.28}$$

where $a(t)$ is scale factor which is a function of time, as described earlier. The information about the evolution of Universe is contained in the scale factor and it is a dimensionless quantity. At present, $a(t = t_0) = a_0$, and is assumed to be unity, implying that comoving distance is same as physical distance. On differentiating Eq. (1.28) w.r.t. time, we get

$$\dot{r}(t) = \dot{a}(t)x \tag{1.29}$$

$$v = \dot{a}(t)x = \frac{\dot{a}(t)}{a(t)}a(t)x \tag{1.30}$$

$$v = \frac{\dot{a}(t)}{a(t)}r(t). \tag{1.31}$$

Compare this equation with Eq. (1.27), we get Hubble parameter in terms of scale factor

$$H = \frac{\dot{a}(t)}{a(t)} \tag{1.32}$$

The information of motion of galaxies relative to us is embedded in their spectra. When a galaxy is moving away from us, the photons emitted by the galaxies have a lower frequency. The resulting spectral lines have a longer wavelength. This is redshifting of photons and is denoted by *redshift*, z. If λ_o and λ_e are the observed wavelength and emitted wavelength of photons from a galaxy, then the redshift is defined as the change in wavelength divided by the wavelength of emitted photons

$$z = \frac{\lambda_o - \lambda_e}{\lambda_e} \tag{1.33}$$

$$1 + z = \frac{\lambda_o}{\lambda_e}. \tag{1.34}$$

The redshift can be related to scale factor[8] as

$$1 + z = \frac{a(t_0)}{a(t)} = \frac{a_0}{a(t)} = \frac{1}{a(t)} \tag{1.35}$$

here, $a_0 = a(t_0)$ is the scale factor at present which is equal to unity. Once redshift is known, we can easily see if objects are moving away from each other or coming closer i.e. if the Universe is expanding or contracting. If z is negative, the photons are blueshifted and Universe is contracting. If z is positive, the Universe is undergoing expansion.

1.4 Friedmann Equations and Solutions

Friedmann equations describe a relativistic, homogeneous and isotropic Universe. Friedmann first derived these equations by solving Einstein's field equations using the Friedmann-Robertson-Walker (FRW) metric. (These equations can also be derived by using Newtonian mechanics[8, 9, 10].) From the solution of Einstein's equations, we obtain a set of coupled differential equation. These coupled equations are described in terms of scale factor, $a(t)$, energy density of matter, $\rho(t)$ and pressure, $P(t)$.

$$\dot{a}^2 + k = \frac{8\pi G}{3}\rho a^2. \tag{1.36}$$

This equation is obtained from the 00 component of the Einstein equations. Scale factor, a(t), describes the relative expansion of the Universe and k in this equation, is the curvature of the Universe. The equation (1.36) can be rewritten as

$$\frac{\dot{a}^2}{a^2} + \frac{k}{a^2} = \frac{8\pi G}{3}\rho. \tag{1.37}$$

The contribution of the diagonal component of the metric in Einstein's equation yields another equation

$$\ddot{a} + \frac{2\dot{a}^2}{a} - \frac{2k}{a} = 4\pi G(\rho - P)a. \tag{1.38}$$

Using Eq. (1.37), we can rewrite this equation as

$$\frac{\ddot{a}}{a} = -\frac{4\pi G}{3}(\rho + 3P), \tag{1.39}$$

this is also called acceleration equation. When $\ddot{a}$ is positive, or the quantity $(\rho + 3P)$ is negative, the expansion of the Universe is undergoing acceleration. If $(\rho + 3P)$ is positive or $\ddot{a}$ is negative, the Universe is decelerating. For a fluid with equation of state $P = w\rho$, if $w > -1/3$, according to equation (1.39), the Universe undergoes a decelerated expansion. For non-relativistic or relativistic matter, pressure is either zero or positive, therefore these two components account only for a decelerated expansion, and cannot account for an accelerated expansion.

In 1998, two teams observing distant Type Ia Supernovae independently found that the expansion of the Universe is accelerating[11, 12]. This discovery is one of the most important development in Cosmology, which indicates existence of some form of fluid responsible for this accelerated Universe[13]. Observations suggest that ordinary matter or baryons (atoms) contributes to approximately 4% of the total energy of the Universe

only, another 23% is some form of dark matter and the rest is 73% is some form of energy, yet to be discovered, sometimes called dark energy. Equation (1.39) indicates that when pressure is sufficiently negative or when the equation of state parameter for a fluid is less than $-1/3$, then the Universe undergoes accelerated expansion. The evolution of the Universe for these components is shown in figure 1.1.

To understand the accelerated expansion, many models have been proposed. One such explanation is by way of a *cosmological constant*, which was introduced by Einstein himself in an attempt to achieve a static, finite Universe. The cosmological constant, Λ was invoked in general relativity in order to counter the gravitational repulsive terms, which would, otherwise, gives a Universe that will eventually collapse. The cosmological constant was introduced in 1917, but later in 1929, when Hubble discovered that the Universe is expanding, it was dropped. The equation of state parameter for cosmological constant is $w = -1$, therefore, if it is the component that describes dark energy then it can, cause the recent cosmic acceleration. In particle physics, cosmological constant is considered as the vacuum energy density. However, the energy scale of Λ in the field theories is much larger than that of the present Hubble constant H_0.This is the cosmological constant problem [14]. A few more models have been proposed in support of dark energy analysis. We will discuss a few of these models below.

1.4.1 Cosmological constant

Einstein first introduced the cosmological constant Λ in order to explain a static Universe. It was assumed that the Universe is dominated by non-relativistic matter and the contribution of relativistic component is negligible and, hence, the energy density is positive but the pressure in the Universe is almost zero. However, the Universe containing only matter cannot be static. Therefore, to have a static Universe, Einstein introduced an additional term containing Λ in field equations, which became

$$R_{\mu\nu} - \big(\frac{1}{2}R - \Lambda\big)g_{\mu\nu} = \kappa^2 T_{\mu\nu}. \tag{1.40}$$

For the FRW spacetime, the Friedmann equations take the form

$$\frac{\dot{a}^2}{a^2} + \frac{k}{a^2} = \frac{8\pi G}{3}\rho + \frac{\Lambda}{3}, \tag{1.41}$$

here, $\rho = \rho_m + \rho_R$, P is the pressure and the acceleration equation becomes

$$\frac{\ddot{a}}{a} = -\frac{4\pi G}{3}(\rho + 3P) + \frac{\Lambda}{3}. \tag{1.42}$$

From equation (1.41) we can say that this addition of cosmological constant term is equivalent to introducing another component in the Universe. The energy density of this component is given by $\rho_\Lambda \equiv \Lambda/8\pi G$, which is constant. The fluid equation (1.20), which remains unchanged by addition of Λ term, states that in order to have a constant energy density, the pressure for cosmological constant must be

$$P_\Lambda = -\rho_\Lambda = -\frac{\Lambda}{8\pi G}. \tag{1.43}$$

So, a static model of the Universe is achieved by introducing the Λ term. In this model, $\dot{a}$ is zero and $\ddot{a}$ also vanishes and equation (1.42) becomes

$$0 = -\frac{4\pi G}{3}(\rho + 3P) + \frac{\Lambda}{3}. \tag{1.44}$$

Therefore, $\Lambda = 4\pi G\rho$ for the case of static Universe. Using condition $\dot{a} = 0$, the equation (1.41) becomes

$$\frac{k}{a^2} = \frac{8\pi G}{3}\rho + \frac{\Lambda}{3} = 4\pi G\rho. \tag{1.45}$$

This shows that the Einstein's Universe which is dominated by non-relativistic matter, is static and has a positive curvature. However, Hubble published his results on the relationship between redshift-distance in 1929, which stated that the Universe is, infact, expanding and not static. This discovery made Einstein drop the term cosmological constant Λ term by taking the value of Λ to be zero in the field equations. In 1998, the observations of redshift-distance relationship for Type-Ia supernovae suggested that the Universe is undergoing accelerated expansion. In order to explain this accelerating expansion, the cosmological constant is reintroduced in the field equations.

Cosmological constant provides the simplest explanation of this accelerated expansion but it is not the only candidate. The accelerated expansion of the Universe is caused by a component of the Universe which has a negative pressure, called 'dark energy'. Many other models have, also, been introduced that have an equation of state which is less than $-1/3$ and gives rise to late time accelerated expansion.

1.4.2 Dark energy

In the absence of any consensus on the model for the accelerated expansion, it is a challenge to connect theory with observations. However, for dark energy, the equation of state provides a useful phenomenological description. As equation of state is the ratio of pressure to energy density, it is also closely connected to the underlying physics. We will now discuss a variety of formalisms that have been used to describe dark energy.

Parameterizations: The simplest parameterization of dark energy is $w =$ constant. This form fully describes vacuum energy ($w = -1$) and together with Ω_{DE} and Ω_m, provides a two-parameter description of the dark energy for a flat Universe (three-parameter description if curvature is assumed).

A number of two-parameter descriptions of w have been explored, a few are given below:

- $w(z) = w_0 + w' \frac{z}{1+z}$ (the Chevallier-Polarski-Linder (CPL) parameterization [15, 16]),
- $w(z) = w_0 + w' \frac{z}{(1+z)^2}$, the Jassal-Bagla-Padmanabhan parameterization [17]
- $w(z) = w_0 + w' log(1+z)$, the logarithmic parameterization[18],
- $w(z) = w_0 + w' sin(z)$, the sine parameterization [19],
- $w(z) = w_0 + w' z$, the linear parameterization [20],
- $w(z) = w_0 + w' \frac{z}{1+z^2}$, Feng-Shen-Li-Li (FSLL) model[21].

For low redshift they are all essentially equivalent, but for larger redshift they exhibit different behavior. The CPL parameterization is the most commonly used description of dark energy. The cosmological parameters in all parameterizations mentioned above are $\Omega_m, \Omega_{DE}, w_0$ and w'.We try to understand whether the dark energy is a constant or if it varies with time. we will discuss a few of these parameterizations and their cosmological implications in chapter 2. There exists other models of dark energy in which the late-time acceleration of the Universe is derived by the scalar field models.

Scalar fields: The fine tuning problem facing dark energy models with a constant equation of state can be avoided if the equation of state is assumed to be time dependent. Models based on scalar fields alleviates this problem. In these models the equation of state evolves depending upon the form of scalar field potential. There are many types of

scalar fields introduced in the literature such as quintessence [22, 23, 24, 25, 26, 27, 28], phantom fields [29], tachyonic scalar fields [30, 31, 32, 33], etc. The scalar fields are also divided into two categories depending upon the evolution of w; thawing fields and freezing fields. In some freezing models, the scalar field energy density tracks that of the dominant component (radiation or matter) at early times and then dominates at late times, providing a dynamical origin for the coincidence. In thawing models, the coincidence is transitory and reflects the mass scale of the scalar field. The motivation for using scalar fields is that it is easy to arrive at conditions for the accelerating state of the Universe using scalar fields and, also, for suitable choices of potentials, we see that this model satisfies conditions for all the previous epochs, i.e., the radiation and matter dominated epochs (see chapter 3).

1.4.3 Solutions of Friedmann equations

In a homogeneous and isotropic Universe, for a barotropic fluid with equation of state $P = w\rho$, the relationship between energy density ρ, pressure P, and scale factor $a(t)$ is given by Friedmann equation (1.37). Observations suggests that the curvature of the Universe, although non-zero, is very small [34]. We will, therefore, assume a spatially flat Universe. For a spatially flat Universe, k is zero, in which case Friedmann equation takes the form

$$H^2 = \frac{\dot{a}^2}{a^2} = \frac{8\pi G}{3}\rho. \tag{1.46}$$

Here, ρ denotes the total energy density of the Universe. It can be written as

$$\rho = \rho_m + \rho_R + \rho_{DE} \tag{1.47}$$

where, ρ_m, ρ_R and ρ_{DE} denotes the energy density of non-relativistic contents, relativistic contents and the dark energy respectively. The density of the Universe when it is flat or expanding critically, for a particular H is called the critical density, ρ_c, is given by

$$\rho_c = \frac{3H^2}{8\pi G}. \tag{1.48}$$

At present, if $\rho_{c,0}$ is the critical density, the Friedmann equation becomes

$$H^2 = H_0^2 \frac{\rho}{\rho_{c,0}} = H_0^2 \left(\frac{\rho_m}{\rho_{c,0}} + \frac{\rho_R}{\rho_{c,0}} + \frac{\rho_{DE}}{\rho_{c,0}} \right). \tag{1.49}$$

We can now define a dimensionless quantity called density parameter, Ω_i (where $i = m, R$ or DE),

$$\Omega_i(a) = \frac{\rho_i(a)}{\rho_c(a)}. \tag{1.50}$$

Then, we will get

$$H^2 = H_0^2 \left(\frac{\Omega_{m,0}}{a^3} + \frac{\Omega_{R,0}}{a^4} + \frac{\Omega_{DE,0}}{a^{3(1+w)}} \right). \tag{1.51}$$

At present time, $H(a) = H_0$, if we use the definition of critical density in Friedmann equation we get,

$$1 = \Omega_{m,0} + \Omega_{R,0} + \Omega_{DE,0} \tag{1.52}$$

this is true at all times. The total sum of all energy density parameter components is equal to one. Now we will consider a Universe with only one kind of matter present in it.

1.4.4 Non-relativistic matter dominated flat Universe

In this case $\Omega_{m,0} = 1$ while $\Omega_{R,0}$=$\Omega_{DE,0} = 0$. The Friedmann equation becomes

$$H^2 = H_0^2 \Omega_{m,0} = H_0^2 \left(\frac{a_0}{a} \right)^3 \tag{1.53}$$

$$\left(\frac{da}{dt} \right)^2 = H_0^2 \frac{1}{a} \tag{1.54}$$

a_0 is the scale factor at present which is equal to one. In the limit of early time, that is, at time $t = 0$ scale factor vanishes,$a = 0$, the solution of the above equation is

$$a(t) = \left(\frac{3}{2} H_0 t \right)^{2/3} \tag{1.55}$$

or the age of the Universe is

$$t = \frac{2}{3H_0} a^{3/2} \tag{1.56}$$

and at present it is $t_0 = \frac{2}{3H_0}$. The evolution of scale factor with cosmic time is shown in figure 1.1 by red solid curve. In this case $H(t) \propto (1/t)$ and hence it is a decelerating Universe. This is Einstein-de Sitter Universe.

1.4.5 Relativistic matter dominated flat Universe

In this case $\Omega_{R,0} = 1$ while $\Omega_{m,0}$=$\Omega_{DE,0} = 0$. The Friedmann equation becomes

$$H^2 = H_0^2 \Omega_{R,0} = H_0^2 \left(\frac{1}{a}\right)^4. \tag{1.57}$$

At $t = 0$, $a = 0$, the solution is

$$a(t) = (2H_0 t)^{1/2} \tag{1.58}$$

and the age of Universe is

$$t = \frac{a^2}{2H_0}. \tag{1.59}$$

This is also a decelerating Universe as $H(t) \propto (1/t)$ and the age of Universe is $t_0 = 1/(2H_0)$. For this case, the evolution of scale factor as a function of cosmic time is shown in figure 1.1 by blue solid curve.

1.4.6 Cosmological constant dominated flat Universe

In this case $\Omega_{DE,0} = 1$ while $\Omega_{m,0}$=$\Omega_{R,0} = 0$.The Friedmann equation becomes

$$H^2 = H_0^2 \Omega_{DE,0} = H_0^2 \tag{1.60}$$

as for Λ dominated Universe $w = -1$. The solution of this equation is obtained by assuming $t = 0$ at $a = 1$, i.e. today, which is

$$a(t) = e^{H_0 t}. \tag{1.61}$$

In this case, the age of the Universe is infinite and it is a Universe which is exponentially expanding. For a Λ dominated Universe, the evolution of scale factor with time is shown in figure 1.1 by the gray solid curve.

The figure 1.2 represents the evolution of the Universe as a function of scale factor. Here, we considered a flat Universe with non-relativistic, relativistic matter and dark energy. The energy density parameter for relativistic component is obtained from the non-relativistic one ($\Omega_r = \Omega_m/3000$). The different curves are obtained for different Ω_m values. Green curve represents a Universe with Ω_m=0.1, black curve is drawn for Ω_m=0.27, red curve is for a Universe containing Ω_m=0.4, the orange curve is for Ω_m=0.6

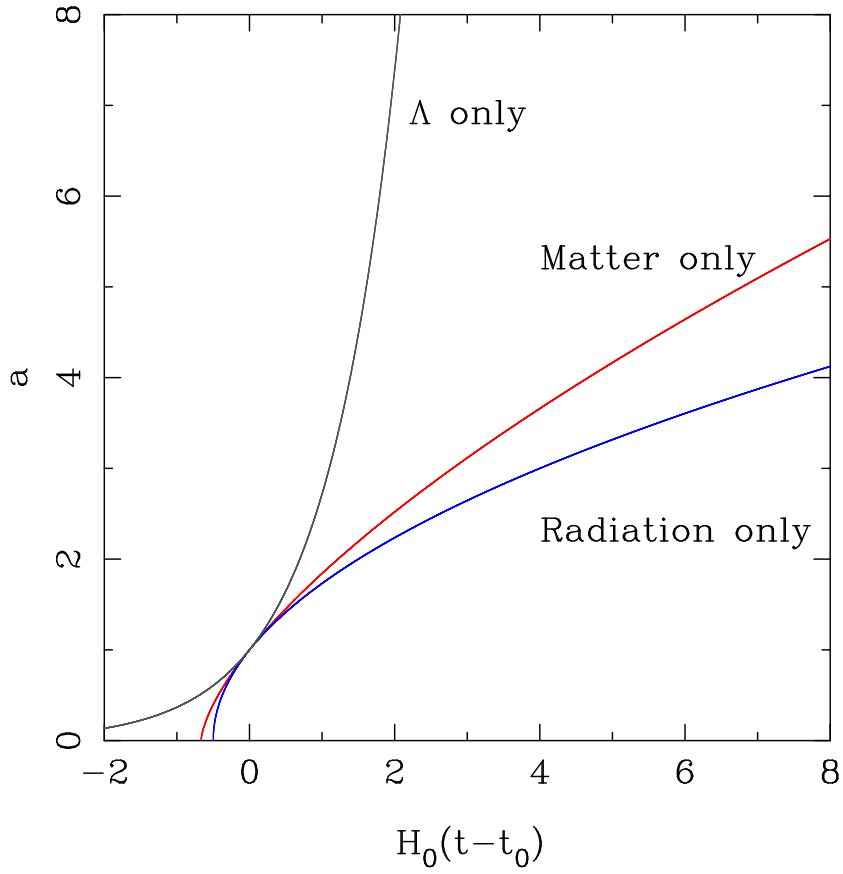

Figure 1.1: The scale factor as a function of cosmic time t is shown for an expanding single component flat Universe. The cosmic time is plotted in terms of $H_0(t - t_0)$. The red curve is for a matter only flat Universe, the blue line shows the evolution of scale factor in radiation only flat Universe, while the gray solid line is obtained by assuming a flat Universe containing cosmological constant only.

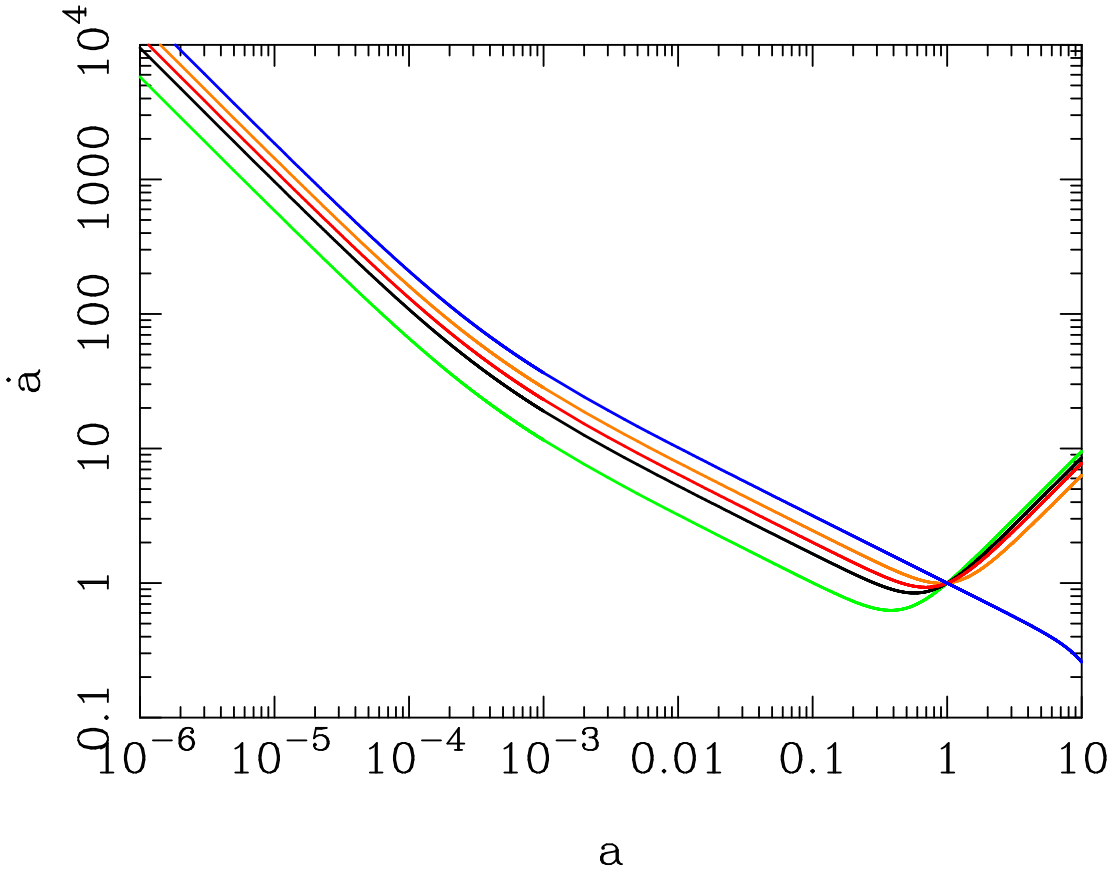

Figure 1.2: The figure shows the evolution of the Universe as a function of scale factor. The y-axis shows the 'velocity' of the Universe with which it expands and x-axis denotes the scale factor. To obtain the plot a flat Universe with non-relativistic, relativistic matter and dark energy is considered. The figure shows the expansion of Universe in radiation dominated era (before a $\sim \times 10^{-3}$, depending upon the value of Ω_m), matter dominated era (10^{-3} to 0.4) and then dark energy dominated era. The different curves shows are drawn for Ω_m= 0.1, 0.27, 0.4, 0.6, 1 respectively.

and the blue curve is for a Universe with Ω_m=1. The slope of the curves at any time gives us the value of Hubble parameter at that time, which in turn, gives us the information about the rate of expansion of the Universe. The velocity of expansion decreases very fast at smaller scale factor, this is because at earlier times the Universe is dominated by relativistic matter and the Universe undergoes decelerated expansion (as $\dot{a} \propto \frac{1}{a}$). After radiation dominated era is the non-relativistic matter dominated era, in which $\dot{a} \propto \frac{1}{a^{1/2}}$ and the Universe will continue to undergo decelerated expansion. But the rate of rate of deceleration in this case is smaller than that in relativistic matter dominated case. Then, at scale factor $a \sim 1$, we have the dark energy dominated era in which the Universe enters an accelerated expansion phase. The rate of acceleration depends upon the dark energy content of the Universe, $\Omega_{DE} = 1 - \Omega_m - \Omega_R$.

1.5 Distance Measurements

To get a sense of separation of objects, we need a measure of distances in cosmology. As it is not possible to directly measure the distance of objects from us, the distance is associated with some observable quantity of the object such as its luminosity or the redshift of galaxy or the angular diameter of an object etc. These observables depends upon the electromagnetic radiation which is emitted by the object and collected by the receiver or the observer.

Let's consider a far away source located at $r = r_e$, which emits the light (electromagnetic radiation) at time $t = t_e$ and the receiver which (observer) is situated at position $r = r_0 = 0$ collects the radiation at time $t = t_0$. The coordinates (t_e, r_e) are associated with the object, when the light is emitted, and the coordinates (t_0, 0) describes the observer. The coordinates of these two points (when the light is emitted and when it is observed) in spacetime are connected by null geodesic ($ds^2 = 0$). If we assume the radiation wave is propagating along $\theta = constant$ and $\phi = constant$, the Eq. (1.1) gives

$$dt^2 = a^2(t)\frac{dr^2}{1 - kr^2}, \tag{1.62}$$

integrating this equation will give a relation between r_e and t_e

$$\int_{t_0}^{t_e} \frac{dt}{a(t)} = \int_0^{r_e} \frac{dr}{\sqrt{1 - kr^2}}. \tag{1.63}$$

The function $r_e(z)$ relates the radial distance of a light emitting source and the redshift when the light emission occurs and hence its very useful. Now, we will define a quantity that is also a function of redshift called the Hubble radius

$$d_H(t) = d_H(z) = \frac{a}{\dot{a}} \tag{1.64}$$

and using the definition of Hubble radius we can easily interchange time derivatives to redshift as

$$dt = \frac{dt}{da}\frac{da}{dz}dz = -d_H(z)\frac{dz}{1 + z}. \tag{1.65}$$

So, the equation (1.63) becomes,

$$\frac{1}{a_0}\int_0^z d_H(z)dz = S_k^{-1}(r_e) \tag{1.66}$$

where $S_k^{-1} = [sinh^{-1}(r_e), r_e, sin{-}1(r_e)]$ for $k = -1, 0, +1$ respectively. The function r_e

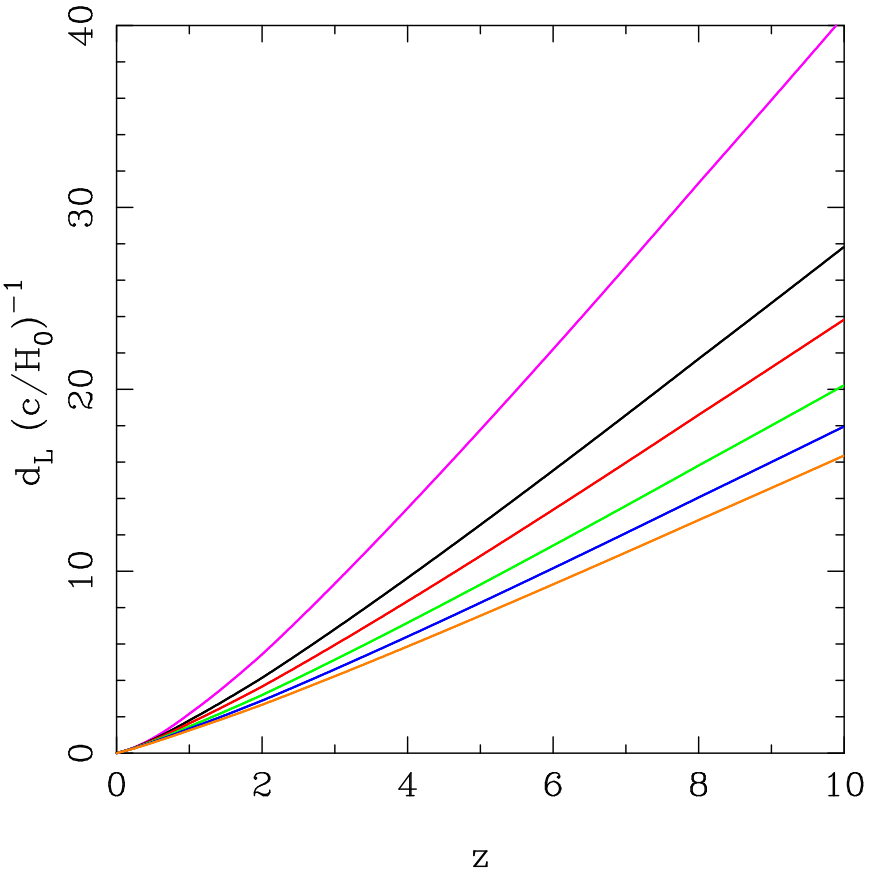

Figure 1.3: In this figure the variation of luminosity distance d_L as a function of redshift, z, is shown. These curves are plotted for a flat wCDM model containing non-relativistic matter (Ω_m), relativistic matter ($\Omega_R = \frac{\Omega_m}{3000}$) and dark energy Ω_{DE}. The curves corresponds to different values of Ω_m. The pink curve is for Ω_m= 0.1, black curve shows the luminosity distance for Ω_m=0.27, red, green , dark blue and light blue curve are drawn for Ω_m= 0.4, 0.6, 0.8 and 1 respectively. Luminosity distance is in units of c/H_0.

can be written as

$$r_e(z) = S_k(\alpha), \qquad \alpha = \frac{1}{a_0}\int_0 z d_H(z) dz. \tag{1.67}$$

The quantity r_e is of much use in cosmology as it helps us calculating two important quantities. First quantity is the luminosity distance of cosmological objects. This quantity relates the luminosity with the observed flux from which we can calculate the luminosity distance. Also, the second quantity we can calculate using this function is the angular sizes of objects. Consider a source of luminosity L which emits photons at

redshift z, then the flux F observed is given by

$$F = \frac{1}{area}\frac{dE_o}{dt_o} \tag{1.68}$$

where, dE_o is the amount of energy observed in dt_o time. If ω is the frequency of photon and intensity is denoted by I, then the quantity I/ω^3 is invariant. As a consequence of this, in the expanding Universe the intensity scales as a^{-3}. In terms of redshift its variation is represented as

$$I(\omega(1+z); z) = I(\omega; 0)(1+z)^3. \tag{1.69}$$

At instant t=0 or at $a = a_0$, a sphere with radius r_e which is the coordinate radius, has an area of $4\pi a_0^2 r_e^2$. The flux observed is, then, given by

$$F = \frac{1}{4\pi a_0^2 r_e^2}\frac{1}{(1+z)^2}\left(\frac{dE_e}{dt_e}\right) = \frac{1}{4\pi a_0^2 r_e^2}\frac{1}{(1+z)^2}L \tag{1.70}$$

where $L = dE_e/dt_e$ and dE_e is the energy emitted in time dt_e. As the flux of any object at a distance d is given as flux = luminosity/4r^2, the *luminosity distance*, d_L, can be defined as

$$d_L = \left(\frac{Luminosity}{4\pi flux}\right)^{1/2} = a_0 r_e(z)(1+z) = a_0(1+z)S_k(\alpha). \tag{1.71}$$

For a flat Universe with dark energy, non-relativistic and relativistic matter as its constituents, the luminosity distance is given by

$$d_L = \frac{c(1+z)}{H_0}\int_0^z \frac{dz'}{\sqrt{\Omega_m(1+z')^3 + \Omega_R(1+z')^4 + \Omega_{DE}(1+z')^{3(1+w)}}}, \tag{1.72}$$

where w is the dark energy equation of state parameter. The behaviour of luminosity distance is shown in figure 1.3. The figure shows luminosity distance d_L in units of c/H_0 as a function of redshift, z. In the figure we consider a flat Universe containing non-relativistic matter (Ω_m), relativistic matter ($\Omega_R = \frac{\Omega_m}{3000}$) and dark energy Ω_{DE}. The different curves corresponds to different values of Ω_m considered. The pink curve is for Ω_m= 0.1, black curve shows the luminosity distance for Ω_m=0.27, red, green, blue and orange curve are drawn for Ω_m= 0.4, 0.6, 0.8 and 1.0 respectively.

Another important quantity that make use of $r_e(z)$ is the *angular diameter* of an object. Consider a source with a physical size D. When observed from large distances it

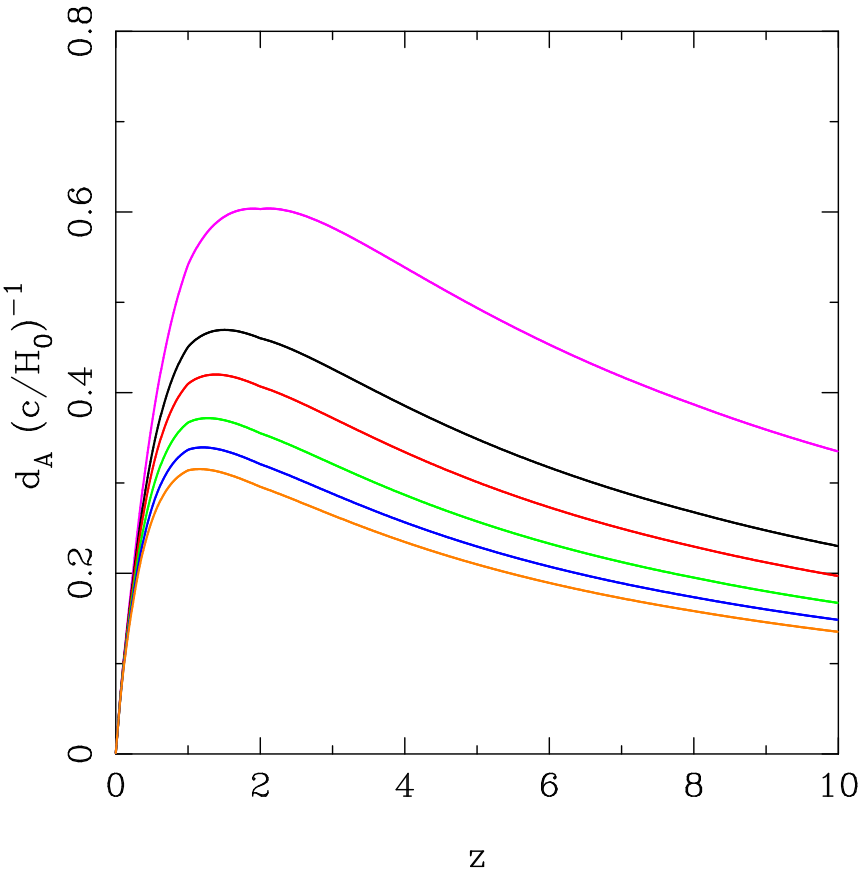

Figure 1.4: In this figure the variation of angular diameter distance d_A as a function of redshift, z, is shown. These curves are plotted for a flat wCDM model containing non-relativistic matter (Ω_m), relativistic matter ($\Omega_R = \frac{\Omega_m}{3000}$) and dark energy Ω_{DE}. The different curves corresponds to different values of Ω_m (from top to bottom curve corresponds to Ω_m = 0.1, 0.27, 0.4, 0.6, 0.8, 1 respectively).

subtends an angle δ. Let d_A denotes the angular diameter distance to the source then $\delta = D/d_A$. In the limits of small δ, $D = r_e a(t_e)\delta$ and angular diameter distance becomes

$$d_A(z) = r_e(z)a(t_e) = a_0 r_e(1+z)^{-1}. \tag{1.73}$$

From equations (1.71) and (1.73), we can see that $d_L = (1+z)^2 d_A$. The figure 1.4 shows the variation of angular diameter distance as a function of redshift for a flat Universe containing non-relativistic matter (Ω_m), relativistic matter ($\Omega_R = \frac{\Omega_m}{3000}$) and dark energy Ω_{DE}. The angular diameter distance is plotted in units of c/H_0. The different curves shows the evolution of d_A in a Universe with different value of non-relativistic contents. Pink curve is drawn for Ω_m=0.1, black corresponds to Ω_m=0.27. The red, green, blue and orange curves corresponds to Ω_m = 0.4, 0.6, 0.8 and 1 respectively.

Distance Modulus: The apparent magnitude, m, of a celestial object is the apparent

flux of the object with respect to some reference flux,

$$m = -2.5 \log_{10}\left(\frac{\mathcal{F}}{\mathcal{F}_{\rm ref}}\right). \tag{1.74}$$

It measures how bright an object appear to us. The absolute magnitude, M, is defined as the magnitude the object would have if it were located at a distance of 10 pc away from the observer. The difference between apparent magnitude and absolute magnitude is called distance modulus and is given by:

$$\begin{aligned}
\mu \equiv m - M &= -2.5 \log_{10}\left(\frac{\mathcal{F}}{\mathcal{F}_{\rm ref}}\right) - (-2.5) \log_{10}\left(\frac{\mathcal{F}_{10\ \rm pc}}{\mathcal{F}_{\rm ref}}\right), \\
&= -2.5 \log_{10}\left(\frac{L}{4\pi d_L^2} \cdot \frac{4\pi (10\ \rm pc)^2}{L}\right), \\
&= 5 \log_{10}\left(\frac{d_L}{10\ \rm pc}\right).
\end{aligned} \tag{1.75}$$

Using the definition of luminosity distance (Eq. (1.72)), distance modulus can be written as

$$\begin{aligned}
\mu &= 5 \log_{10}\left(\frac{d_L}{10\ \rm pc}\right), \\
&= 5 \log_{10}\left[\frac{c}{H_0}(1+z)\frac{\int_0^z \frac{dz'}{\sqrt{\Omega_m(1+z')^3+\Omega_R(1+z')^4+\Omega_{DE}(1+z')^{3(1+w)}}}}{10\ \rm pc}\right].
\end{aligned} \tag{1.76}$$

This is the equation we will use in the supernovae (SNIa) analyses.

1.6 Observational data

In this section, we discuss the different types of observations that we used in our analysis. These observations include Type Ia Supernovae (SNIa), Baryon Acoustic Oscillations (BAO) data and the Hubble parameter (H(z)) measurements.

1.6.1 Type Ia supernovae data

The evidence for recent accelerating expansion came from the study of Type Ia supernova observations. Two independent groups, the Supernova Cosmology Project (SCP) [11] and the High-z Supernova Search Team [12], studied these cosmic objects and reported the

same discovery, individually. In the original observations, the SCP team had observed 42 Type Ia supernovae (SNIa), while the other team had studied 34 closeby SNIa and 16 high-z supernovae. With improved technology, the number of SNIa observed has improved drastically.

Supernovae are believed to be created by two types of processes: (i) a massive star in later stages of its life undergoing gravitational collapse of core, or (ii) a thermonuclear explosion in a white dwarf star [35]. The first mechanism is called the *core collapse* mechanism and the second mechanism is powered by the great amount of energy released during the nuclear reaction undergoing in the interior of the star under extreme conditions, and its called the *thermonuclear* mechanism.

Classification of supernovae

The supernovae are classified observationally by studying their *lightcurves* and the absence of spectral lines associated with different chemical elements. If hydrogen lines are absent in the spectra, the supernova is classified as Type I supernova, else, the presence of H-lines indicates a Type II supernova. Type I supernovae are further sub-classified into three categories; spectra of Type Ia has strong Si absorption lines, Type Ib has Helium lines, and Type Ic have none of hydrogen, silicon or helium lines in their spectra. Similarly, further sub-classification of Type II supernovae are there depending upon their light curves. All the supernovae except Type Ia are understood to be caused by core collapse of massive stars [35].

Type Ia Supernova is the result of a thermonuclear runaway in a Carbon-Oxygen white dwarf (WD) star. This star is an accreting white dwarf star in a binary system with a companion star, which could be a main sequence staror another white dwarf star.Because of the large gravity of WD, it pulls material from the binary companion, and consequently, the mass of WD increases. As the white dwarf star approaches the Chandrasekhar mass limit, the electron degeneracy pressure cannot hold the gravitational collapse any longer, and the temperature of the core increases. This leads to the fusion of Carbon inside the star, which increases the temperature even further. This gives rise to a fusion of nuclei inside the star. As a result, carbon and oxygen nuclei convert into more stable heavier elements (^{56}Ni, ^{56}Co or ^{56}Fe), releasing vast amounts of energy. The resulting energy is more than enough to unbind a star and the star explodes. The energy of this explosion is so large that it can outshine the host galaxy of the white dwarf.

Type Ia supernovae belong to a special class of objects, called the 'standard candles'[36]. These objects have a uniform intrinsic brightness, which is known. By comparing the lu-

minosity of the object to the observed brightness, one can easily calculate the distance to the object. The uniformity is believed to be due to the similarity in mass limitthe Chandrasekhar mass limit.The SNIa are not "exactly" standard candles. They have similar but not the same light curves; their peak brightness varies by a factor of two. However, as their luminosities are found to be closely related, SNIa can be standardized using empirical methods and correlations using supernovae luminosity and other variables. Two commonly used techniques for this purpose are: (i) light curve width-luminosity relationship [37] and (ii) luminosity and SN color relationship [38]. Hence, SNIa are '*standardizable*' candles. They are powerful tools to measure very large distances in Universe as they are visible at very large distances because of their extreme brightness.

We quantify the brightness of an object by way of 'magnitude'. The brighter an object is, the smaller is its magnitude and vice-versa. Apparent magnitude is the magnitude of an object measured from earth. Consider two objects A and B with apparent fluxes F_A and F_B. The apparent magnitude of these objects are defined as

$$m_A = -2.5\log_{10}\left(\frac{F_A}{F_{\rm ref}}\right), \qquad m_B = -2.5\,\log_{10}\left(\frac{F_B}{F_{\rm ref}}\right). \tag{1.77}$$

If we subtract the two, we get

$$m_A - m_B = -2.5\,\log_{10}\left(\frac{F_A}{F_B}\right). \tag{1.78}$$

This equation implies that if $m_A = 3.5$ and $m_B = 1$, then star A is 10 times fainter than the star B. Now, we define a '*absolute magnitude*', which is the apparent magnitude of an object which is placed at a distance of parsecs from the Earth. (1 parsecs = 3.26 light years.) Using Eq. 1.75, the absolute magnitude M of an object in terms of an apparent magnitude m and luminosity distance d_L is

$$\mu = m - M = 5\,\log_{10}\left(\frac{d_L}{10{\rm pc}}\right), \tag{1.79}$$

where μ is the distance modulus. From the above equation we see that by comparing the apparent magnitude of an unknown object with the object located at 10 pc away from us, we can find an estimate of distance to the unknown object. In other words, the absolute magnitude and the apparent magnitude of the object are the same if it were located at a luminosity distance of$d_L = 10$ pc from the Earth.

When distance is expressed in units of Mega-parsecs the Eq. 1.79 can be rewritten as

$$m - M = 5\ \log_{10} d_L + 25. \tag{1.80}$$

At the peak brightness, the absolute magnitude of SNIa is observed to be approximately $M = -19$. If we know the apparent magnitude of a SNIa, we can calculate the luminosity distance by using Eq. 1.80 (as SNIa are standardized candles, M is the same for all, i.e.$\sim$ -19).

These observations are used in studying the expansion history of the Universe. By studying the spectral data of a SNIa and evaluating the frequency or wavelength of the photons, the redshift corresponding to a particular SNIa can be estimated. The luminosity distance or distance modulus of a SNIa is a function of redshift. So by calculating the luminosity distance theoretically and comparing it with observed data, we can conclude the expansion history of Universe.

Consider a Universe with non-relativistic matter and dark energy as its dominant components. The evolution of the Universe is then given by the Hubble parameter as

$$H(z) = H_0 \left[\Omega_{m_0} (1+z)^3 + \ \Omega_{DE_0}\ \exp\left\{ \int_0^z \frac{3\big[1 + w_{DE}(z')\big]}{1+z'} \mathrm{d}z' \right\} + \left(1 - \Omega_{DE_0} - \Omega_{m_0}\right)(1+z)^2 \right]^{1/2}, \tag{1.81}$$

where, H_0 is the present day value of Hubble parameter, w_{DE} is the equation of state of dark energy, Ω_{m_0}, Ω_{DE_0} are the energy density of non-relativistic matter and dark energy at present. The third term describes the curvature of the Universe. When redshift is very small (i.e. $z \ll 1$), the luminosity distance is given by

$$d_L(z) = \frac{1}{H_0} \left[z + \frac{1}{4} \left(1 - 3 w_{DE} \Omega_{DE_0} + \Omega_{k0}\right) z^2 + O(z^3) \right]. \tag{1.82}$$

For a flat Universe (k=0) without dark energy ($\Omega_{DE_0} = 0$), then the luminosity distance for small redshift range ($z \ll 1$) can be written as

$$d_L(z) = \frac{1}{H_0} \left[z + \frac{1}{4} z^2 + O(z^3) \right]. \tag{1.83}$$

If we consider only non-relativistic matter ($\Omega_{DE} = 0$), then the luminosity distance to

an object is smaller than the case when dark energy component contributes to the total energy density of the Universe (for dark energy $w < -1/3$). For a fixed set of parameters, a smaller w_{DE} leads to a larger value of d_L, and the higher the value of dark energy density parameter, larger is the luminosity distance. Also, if all other parameters are fixed, and only Ω_k is varied, then an open Universe will have a higher value of luminosity distance than in the case of a flat Universe.

In case of a flat Universe ($\Omega_k = 0$), where only non-relativistic matter and dark energy (with EoS $w_{DE} = constant$) contributes to the total density of the Universe, the Hubble parameter is given by

$$H(z) = H_0\sqrt{\Omega_{m_0}(1+z)^3 + \Omega_{DE_0}(1+z)^{3(1+w_{DE})}}, \tag{1.84}$$

and the luminosity distance is given by

$$d_L(z) = \frac{(1+z)}{H_0}\int \frac{dz'}{\left[\Omega_{m_0}(1+z')^3 + \Omega_{DE_0}(1+z')^{3(1+w_{DE})}\right]^{1/2}}, \tag{1.85}$$

which we solve numerically. We calculate luminosity distance for 580 data points corresponding to each SNIa in the Union2.1 Supernovae dataset [39] and compare the theoretically calculated distance modulus to the observed one. Using this, we constrain the parameters Ω_m and w_{DE} (which we denoted by Ω_m and w respectively, in chapter 2) and the results of which are reported in next chapter.

1.6.2 Baryonic Acoustic Oscillation (BAO) Measurements

When the Universe was very young, its made up of hot plasma of photon and baryons. Photons were trapped between the atoms, bouncing back and forth. This produced density perturbations in the plasma which travelled with the speed of sound [40]. As space expanded, the density of the Universe decreases and temperature dropped low enough that the baryons could combine and become electrically neutral. Tt which point the Universe became transparent and the photons were released. The photons have been propagating freely ever since, forming the cosmic microwave background (CMB) which we can detect today. This epoch is called the epoch of "recombination."

With the freeing of the photons, the pressure that caused the baryons to oscillate was lifted, and the baryons were frozen in position. As the Universe expanded, the small density perturbations formed structures. The imprint of the acoustic peaks is still

visible in the distribution of galaxies today. The cosmological surveys have found that the galaxies tend to have excess clustering on scales of about 150 Mpc. This is the first acoustic peak.

This provides us with a new cosmological test. The length at which this excess clustering is found, is a "standard ruler" - a fixed length that doesn't change (apart from the change due to the expansion of the Universe). So this gives us a way to measure distances corresponding to different redshifts, which is quite independent of supernovae and the other distance ladder techniques. One can compare all the lengths measured directly to the size of the acoustic peak in the microwave background, and therefore much earlier times can be probed by those by any other methods. The sound horizon at which baryons became transparent to photons determines the location of the baryon acoustic oscillation peak length scale. This epoch, called the drag epoch, occurs at the redshift z_d and the length scale is

$$r_s(z_d) = \int_0^{\eta_{\rm drag}} c_s(\eta)\ \mathrm{d}\eta, \tag{1.86}$$

where c_s is the speed of acoustic wave and η is conformal time. The constraints on z_d [41, 42] and $r_s(z_d)$ [42] from WMAP fata are found to be $z_d \approx 1020.5 \pm 1.6$ and $r_s(z_d) = 153.3 \pm 2.0$ Mpc.

In principle, we can measure the angle distribution orthogonal to the line of sight $\theta_s(z)$ and the oscillation along the line of sight $\delta z_s(z)$ given by [43]

$$\theta_s(z) = \frac{r_s(z_d)}{(1+z)d_A(z)}, \qquad \delta z_s(z) = \frac{r_s(z_d)H(z)}{c}, \tag{1.87}$$

where c is the speed of light.

The ratios $\theta_s(z)$ and $\delta z_s(z)$ are obtained together from a spherically averaged spectrum as they cannot be measured independently [44]. The combined distance scale ratio for $\theta_s(z)$ and $\delta z_s(z)$ is given as

$$\left[\theta_s^2(z)\delta z_s(z)\right]^{1/3} = \frac{r_s(z_d)}{\left[(1+z)^2 d_A^2(z)c/H(z)\right]^{1/3}}, \tag{1.88}$$

or an effective distance ratio

$$D_V(z) = \left[(1+z)^2 d_A^2(z) \frac{c}{H(z)}\right]^{1/3}. \tag{1.89}$$

In 2005, Eisenstein et al. [44] obtained $D_V(z) = 1370 \pm 64$ Mpc at $z = 0.68$.

In 2007, Percival et al. [45], measured the effective distance ratio (sometimes in liturature it is denoted by d_z) defined by

$$r_{\rm BAO}(z) = \frac{r_s(z_d)}{D_V(z)}, \tag{1.90}$$

at two different redshifts. This is based on data from the 2-degree Field (2-dF) Galaxy redshift survey. In 2010, Percival et al. used SDSS data to determine the same quantity [46] and in 2011, using 6dF Galaxy Survey (6dFGS) measurements, Beutler et al.[47] provide another observation. Then in 2011, Black et al.[48] considered the acoustic parameter introduced by Eisenstein et al.[44], and based on the data from WiggleZ Dark Energy Survey found $A(z)$ at three different redshifts.

1.6.3 Hubble parameter $H(z)$ measurements

The Hubble parameter data is a data showing cosmological expansion rate as a function of redshift. The data that we used has 28 data points corresponding to redshifts ranging from $z \sim 0.07$ to 2.3. The data points are taken from a number of sources (for details see [49, 50, 51, 52, 53, 54, 55, 56, 57]).

Chapter 2

Fluid models of Dark energy

In this chapter, we constrain dark energy model parameters using different observations at low redshifts. Consider the dark energy as a barotropic fluid, with the equation of state a constant as well the case where dark energy equation of state is a function of time. We compare constraints obtained from the observations (discussed in chapter 2) and also do a combined analysis. The combined observational constraints put strong limits on variation of dark energy density with redshift. In previous chapter we discussed the ΛCDM model and its shortcomings. Subsequently we discuss some other models of dark energy. This chapter is adapted from **A. Tripathi, A. Sangwan, and H. K. Jassal, *JCAP*, 1706(06):012, 2017**[58].

2.1 wCDM model of dark energy

The cosmological constant, time-independent dark energy is a spatially homogeneous fluid with equation of state parameter given by $w_\Lambda = P_\Lambda/\rho_\Lambda = -1$, where ρ_Λ and P_Λ are the fluid energy density and pressure respectively. We can model dark energy as a spatially-homogeneous fluid with equation-of-state parameter $w = P_{DE}/\rho_{DE} < -1/3$, an arbitrary constant, where ρ_{DE} and P_{DE} are the energy density and pressure of the fluid denoting dark energy respectively. When $w = -1$ the wCDM parameterization reduces

to ΛCDM. The evolution of the universe for a homogeneous and isotropic universe is given by the evolution of Hubble parameter, which is

$$H(z) = H_0 \left[\Omega_m(1+z)^3 + \Omega_{DE}(1+z)^{3(1+w)} + \Omega_k(1+z)^2\right]^{1/2}. \tag{2.1}$$

k is the curvature at present. Since $\Omega_m + \Omega_k + \Omega_{DE} = 1$, we can write Eq. (2.1) explicitly in terms of the three free parameters as

$$H(z) = H_0 \left[\Omega_m(1+z)^3 + (1-\Omega_m-\Omega_k)(1+z)^{3(1+w)} + \Omega_k(1+z)^2\right]^{1/2}. \tag{2.2}$$

Here, $\Omega_m, w, \Omega_k)$ are the parameters that defines the model. For a spatially flat universe, $\Omega_k = 0$. In this case the rate of expansion of the Universe is given by

$$\left(\frac{\dot{a}}{a}\right) = H_0 \left[\Omega_m(1+z)^3 + (1-\Omega_m)(1+z)^{3(1+w)}\right]^{1/2}. \tag{2.3}$$

For the flat case, the wCDM model is described by parameters Ω_m and w. The second Friedmann equation or the acceleration equation in terms of energy density parameters, is

$$\left(\frac{\ddot{a}}{a}\right) = -\frac{1}{2}H_0^2 \left[\frac{\Omega_m}{a^3} + \frac{\Omega_{DE}}{a^{3(1+w)}}(1+3w)\right]. \tag{2.4}$$

For zero cosmological acceleration at the present time we set $a = a_0 = 1$, $\ddot{a} = 0$ at present time we set $a = a_0 = 1$ in Eq. (2.4), and get

$$\Omega_m + \Omega_{DE}(1+3w) = 0. \tag{2.5}$$

Using $\Omega_{DE} = (1-\Omega_m)$, in spatially-flat wCDM parameterization we can write the above equation as

$$\omega_{DE} = \frac{1}{3(\Omega_m - 1)}. \tag{2.6}$$

In general, the energy density for any fluid with an equation of state $w(z)$ is given by

$$\rho = \exp\left\{3\int_0^z \frac{dz}{1+z}\left[1+w(z)\right]\right\}. \tag{2.7}$$

For dark energy with a constant equation of state, the above equation yields

$$\rho_{DE} = \rho_{DE}(z=0)(1+z)^{3(1+w)}. \tag{2.8}$$

Here $\rho_{DE}(z=0)$ is the present value of dark energy density. In the analysis we have considered a spatially flat universe with non-relativistic matter and dark energy as its main components. As at smaller redshifts radiation is negligible, the relativistic component can be ignored.

2.1.1 Constraints on cosmological parameters

By solving the cosmological equation 2.3 we get the evolution of the universe and to constrain the parameters we use different observations discussed in previous chapters. For the analysis we use χ^2 technique,(see 5). For the wCDM model, the only parameters we have to constrain are matter density parameter Ω_m and equation of state of dark energy w. The priors considered are listed in table 2.1. However, the evolution of the universe also depends upon the present value of Hubble parameters. So we will also see the variation in constraints as the value of Hubble parameter is changed. The Hubble parameter is taken to be equal to 70 $km/s/Mpc$. This is because the absolute magnitude of supernova is a nuisance parameter and as the determination of absolute magnitude is degenerate with determination of the value of Hubble constant, and the latter is also then a nuisance parameter [39]. Therefore, for consistency with the earlier analyses we fix the value of H_0 to 70 $km/s/Mpc$. Similarly, while analyzing the BAO observations, the $D_v(z)$ and $A(z)$ have been determined using H_0= 70 $km/s/Mpc$. But in case of $H(z)$ data we marginalize over the present value of Hubble parameter.

Constraints from Supernova Type Ia (SNIa) data: We minimize χ^2 for supernovae data with respect to the model parameters to find the best-fit parameter values and constraint contours. Figure 2.1 shows constraints obtained from SNIa data on the dark energy model we consider here. This figure shows 1σ, 2σ and 3σ contours corresponding to 67.3%, 95% and 99% confidence levels in the Ω_m-w plane. Different contours corresponds to different confidence levels.

The contours are obtained when Hubble parameter is considered to be equal to $H_0 =$ 70 $km/s/Mpc$. The minimum value $\chi^2_m = 562.29$ corresponds to the values $w = -1.04$ and $\Omega_m = 0.29$. The allowed range for equation of state parameter is -1.57 to -0.66 and $\Omega_m = 0.05$ to 0.43. This model is consistent with cosmological constant. Also, we found that for SNIa data, if the value of Hubble parameter at present increases, the 3σ allowed range decreases. From the results we found that if $H_0 = 70$ $km/s/Mpc$, the model is consistent with the cosmological constant model but as we go away from this value, in both directions, our model shows less and less agreement with cosmological

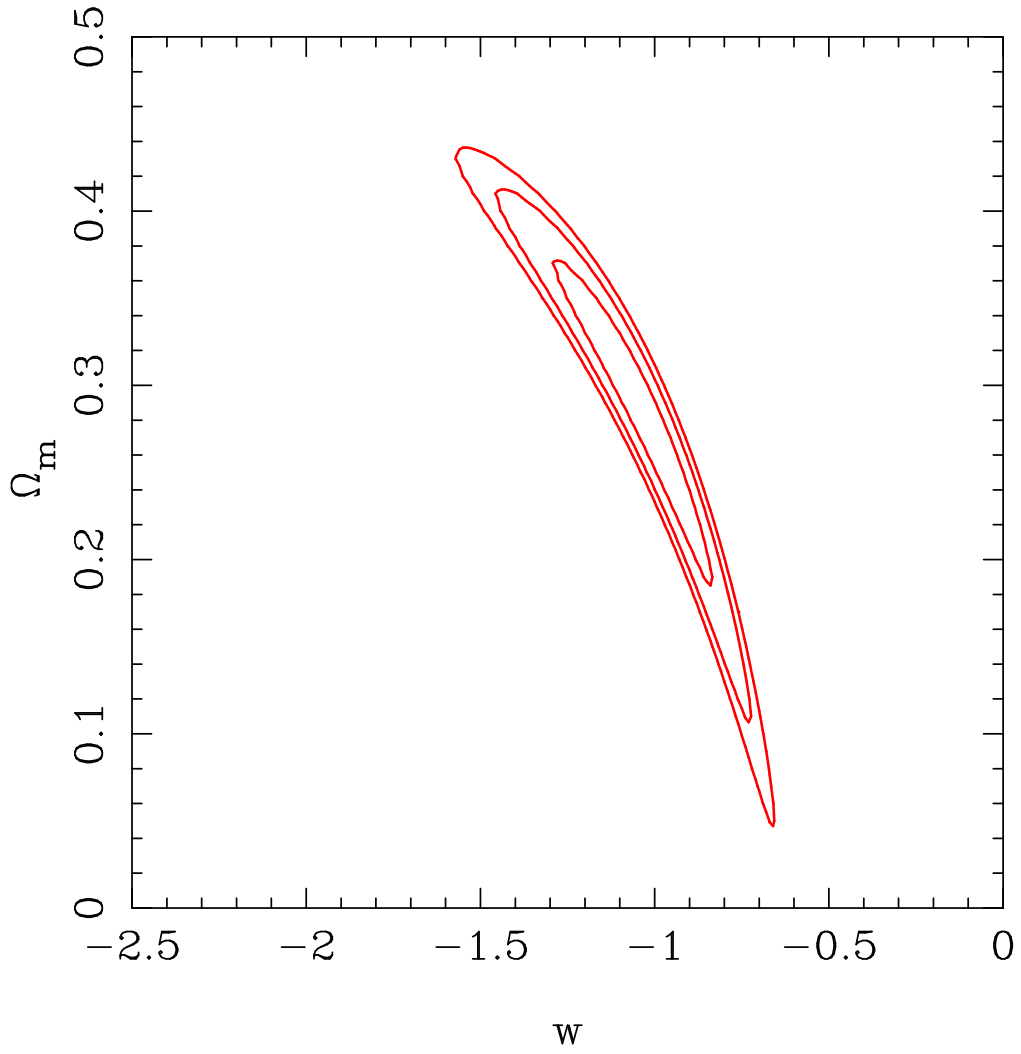

Figure 2.1: In figure we show the 1σ, 2σ and 3σ confidence contours obtained from the analysis of SNIa data in Ω_m-w plane. To obtain these contours we set Hubble parameter H_0=70 $km/s/Mpc$.

constant model.

The figure 2.2 represents dark energy density versus redshift. To obtain this figure we assumed $H_0 = 70\ km/s/Mpc$. The white region in the middle is the allowed range of dark energy density at 1σ level and the regions with slanted lines (Blue) and hatched lines (red) allowed 2σ and 3σ ranges respectively. The solid blue region is ruled out. The dotted line corresponds to $w = -1/3$ and the dotted-dashed line is drawn for $w = -1$, cosmological constant.

Constraints from Baryon Acoustic Oscillation data: In an attempt to further tighten the cosmological parameter constraints, we now include BAO data in the analysis. To constrain cosmological parameters using BAO data we follow the procedure of Blake *et*

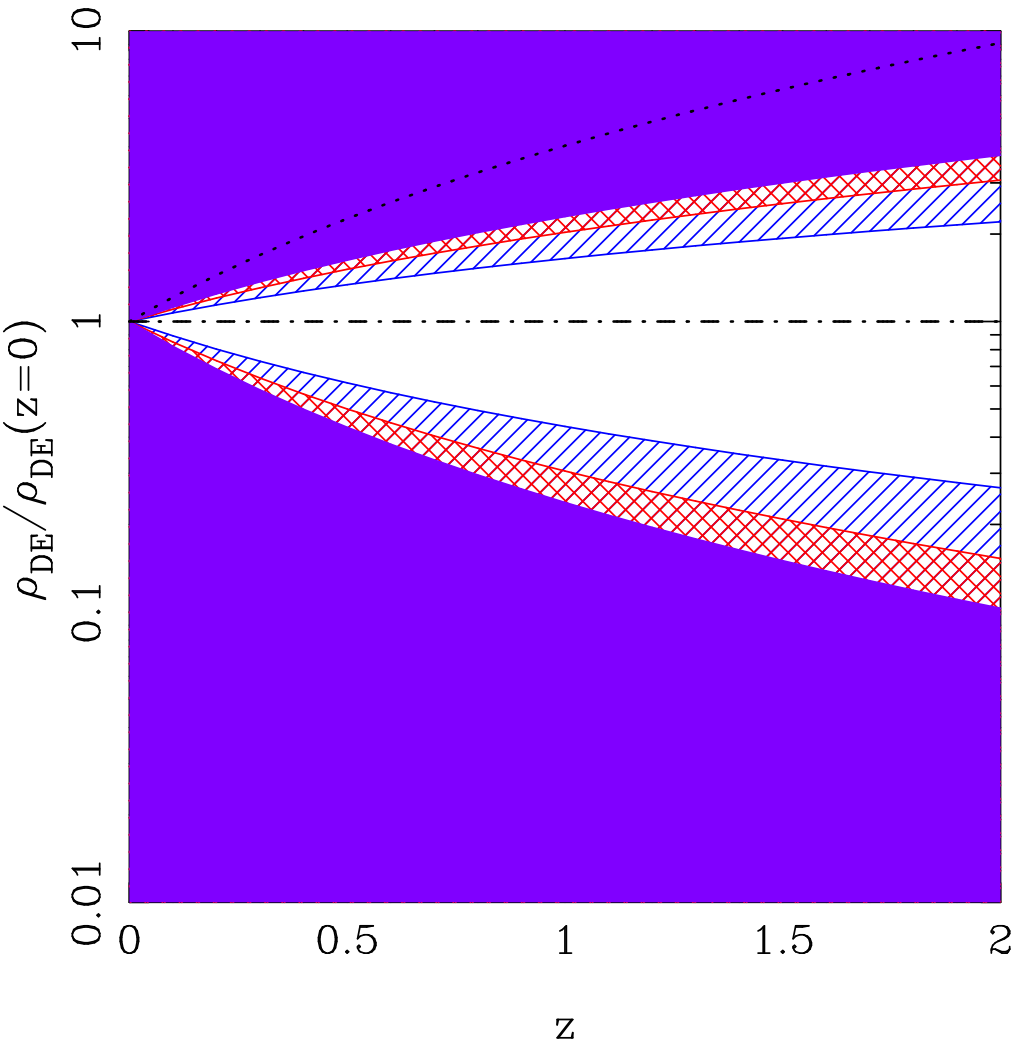

Figure 2.2: The figure represents dark energy density versus redshift for the SNIa observations. The figure is plotted for $H_0 = 70\ km/s/Mpc$. The white region in the middle is the allowed range of dark energy density at 1σ level and the regions with slanted lines (Blue) and hatched lines (red) allowed 2σ and 3σ ranges respectively. The solid blue region is ruled out. The dotted line corresponds to $w = -1/3$ and the dotted-dashed line is drawn for $w = -1$, cosmological constant.

Parameter	Lower Limit	Upper Limit
Ω_m	0.01	0.6
w	-4.0	0.0

Table 2.1: This table lists the priors used for parameter fitting in case of wCDM model.

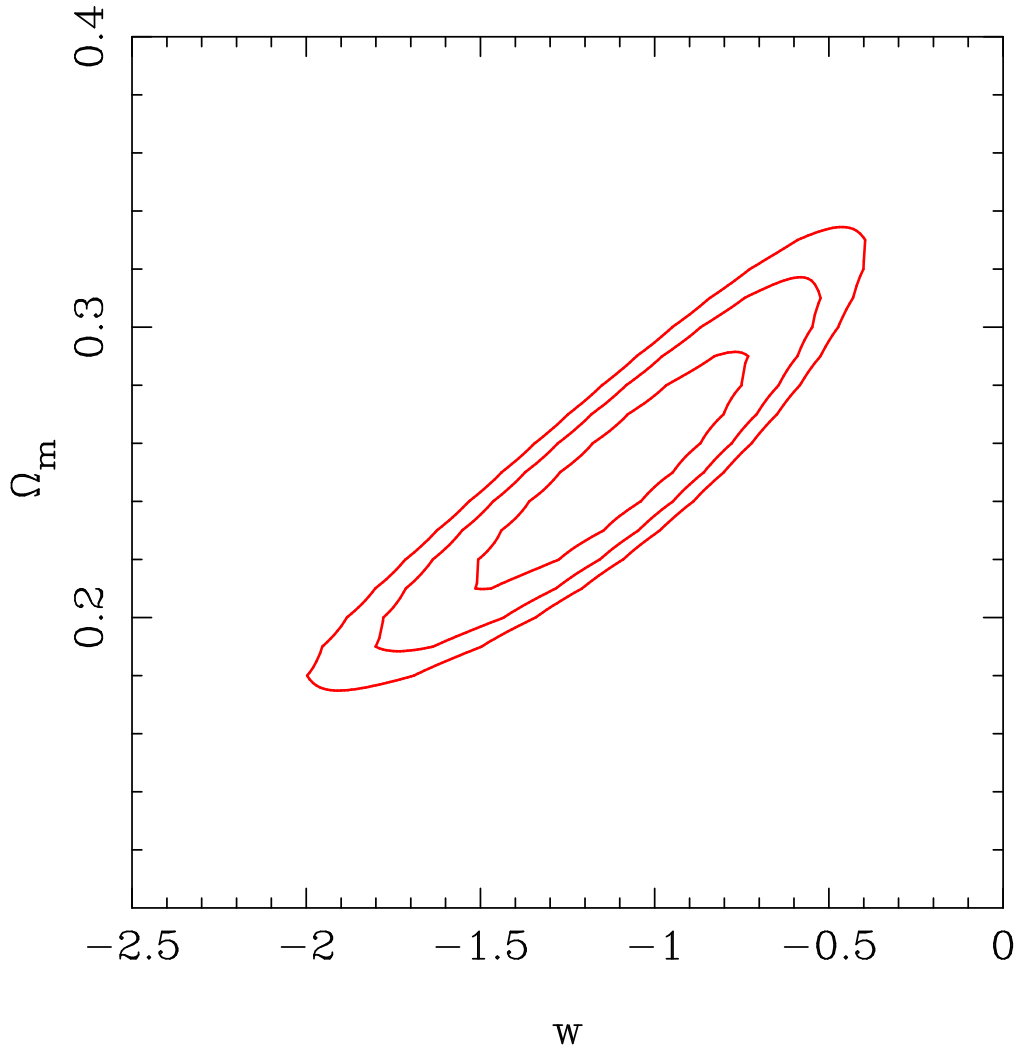

Figure 2.3: The figure represents 1σ, 2σ and 3σ confidence contours obtained from the analysis of Baryon Acoustic Oscillation data in Ω_m-w plane. The contours are for H_0=70 $km/s/Mpc$.

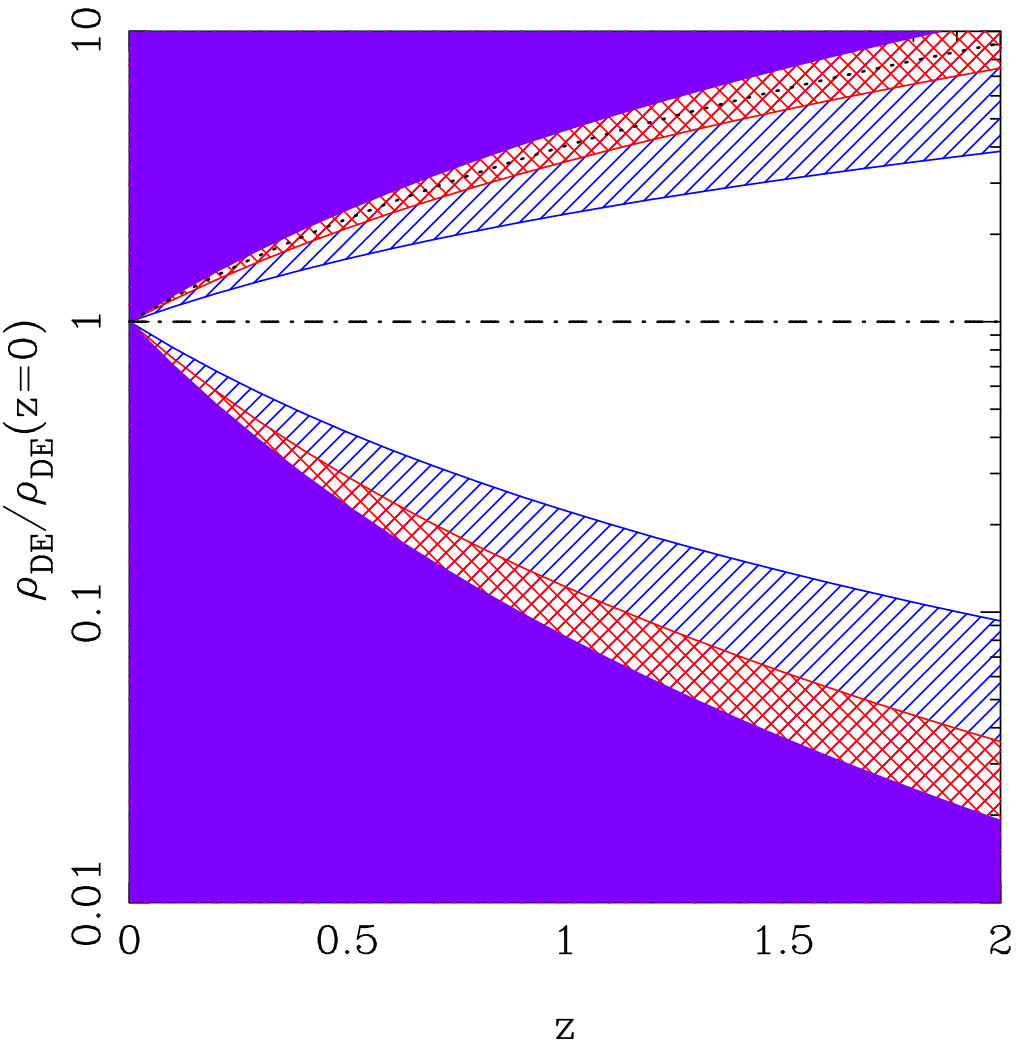

Figure 2.4: The figure represents dark energy density versus redshift for the Baryon Acoustic oscillation observations. The figure is plotted for $H_0 = 70\ km/s/Mpc$. The white region in the middle is the allowed range of dark energy density at 1σ level and the regions with slanted lines (Blue) and hatched lines (red) allowed 2σ and 3σ ranges respectively. The solid blue region is ruled out. The dotted line corresponds to $w = -1/3$ and the dotted-dashed line is drawn for $w = -1$, cosmological constant.

al[48]. To derive the BAO constraints we make use of the distance parameter $D_V(z)$, a combination of the angular diameter distance and the Hubble parameter, given by:

$$D_V(z) = \left[(1+z)^2 d_A(z)^2 \frac{c\ z}{H(z)}\right]^{1/3}. \tag{2.9}$$

Here $d_A(z)$ is the angular diameter distance (discussed in chapter 1). We use measurements of the acoustic parameter $A(z)$ from Blake *et al*,[48] where the theoretically-predicted $A_{\rm th}(z)$ is given in Eq. (5) of Eisenstein *et al.*:[44]

$$A_{\rm th}(z) = \frac{100\ D_V(z)\ \sqrt{\Omega_m h^2}}{z}. \tag{2.10}$$

We maximize the likelihood by minimizing χ^2 for BAO data with respect to the model parameters to get best-fit parameter values and constraint contours. Figure 2.3 shows the constraints from the BAO data on the dark energy model parameters we consider here. These value of Hubble parameter is considered to be 70 $km/s/Mpc$ and the results are shown in contours. The minimum value $\chi^2_m = 0.96$ corresponds to $w = -1.17$ and $\Omega_m = 0.27$. 3σ allowed range for w is -2.19 to -0.42 and for Ω_m is $0.19 - 0.36$.

Also, we found that as the value of H_0 increases, the allowed range of parameter increases. The model is consistent with the cosmological constant model at this values of H_0 considered in the analysis.

In figure 2.4, we show the variation of dark energy density versus redshift for BAO observations. The figure is plotted for $H_0 = 70\ km/s/Mpc$. The white region in the middle is the allowed range of dark energy density at 1σ level and the regions with slanted lines (Blue) and hatched lines (red) allowed 2σ and 3σ ranges respectively. The solid blue region is ruled out. The dotted line corresponds to $w = -1/3$ and the dotted-dashed line is drawn for $w = -1$, cosmological constant. In this case we found that the allowed range of dark energy is bigger than that we obtained for $SNIa$ case. The wCDM parameterization constraints shown in this figure are in good agreement with those shown in Blake *et al*[48].

Constraints from Hubble Parameter (Hz) measurements: The $H(z)$ data contains the value of Hubble parameter at different redshifts along with errors associated with it. We minimize χ^2 for the model parameters to get the best fit value. Figure 2.5 shows the constraints from the Hubble parameter measurements data on the dark energy model considered. The contours are obtained when Hubble parameter is marginalised. For this

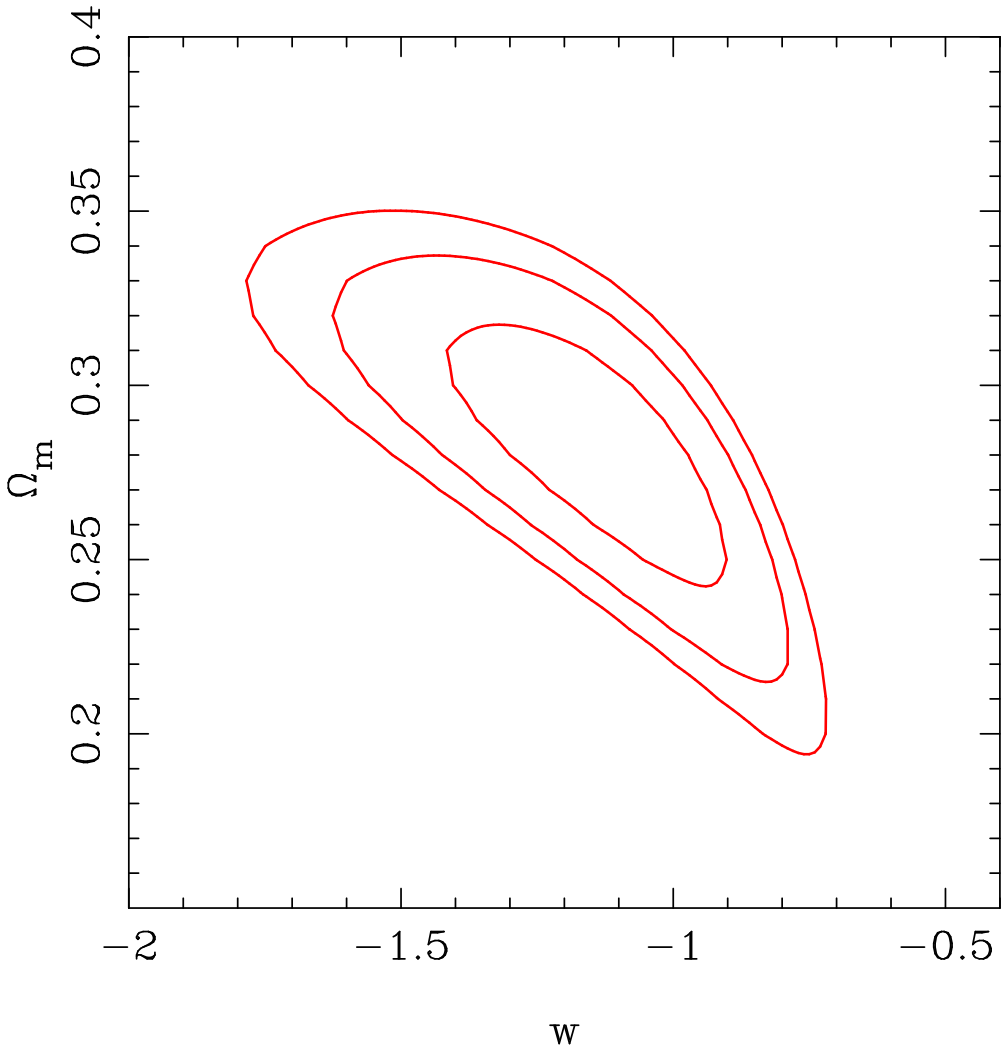

Figure 2.5: The figure represents 1σ, 2σ and 3σ confidence contours obtained from the analysis of Hubble parameter measurement data in Ω_m-w plane. The contour is obtained by marginalising over H_0.

case, $\chi^2_m = 16.27$ for $w = -1.12$ and $\Omega_m = 0.28$. Allowed range for Ω_m is 0.2 to 0.35 and for equation of state parameter it is given by -1.78 to -0.72. The cosmological constant model is consistent within 3σ limit.

The figure 2.6 represents dark energy density versus redshift for Hubble parameter measurements. The different region corresponding to white color or blue and red colors with lines show the allowed range of dark energy density at 1σ level, 2σ and 3σ ranges respectively. The solid blue region is ruled out. The dotted line corresponds to $w = -1/3$ and the dotted-dashed line is drawn for $w = -1$, cosmological constant.

Combined Constraints: To constrain cosmological parameters from a joint analysis of

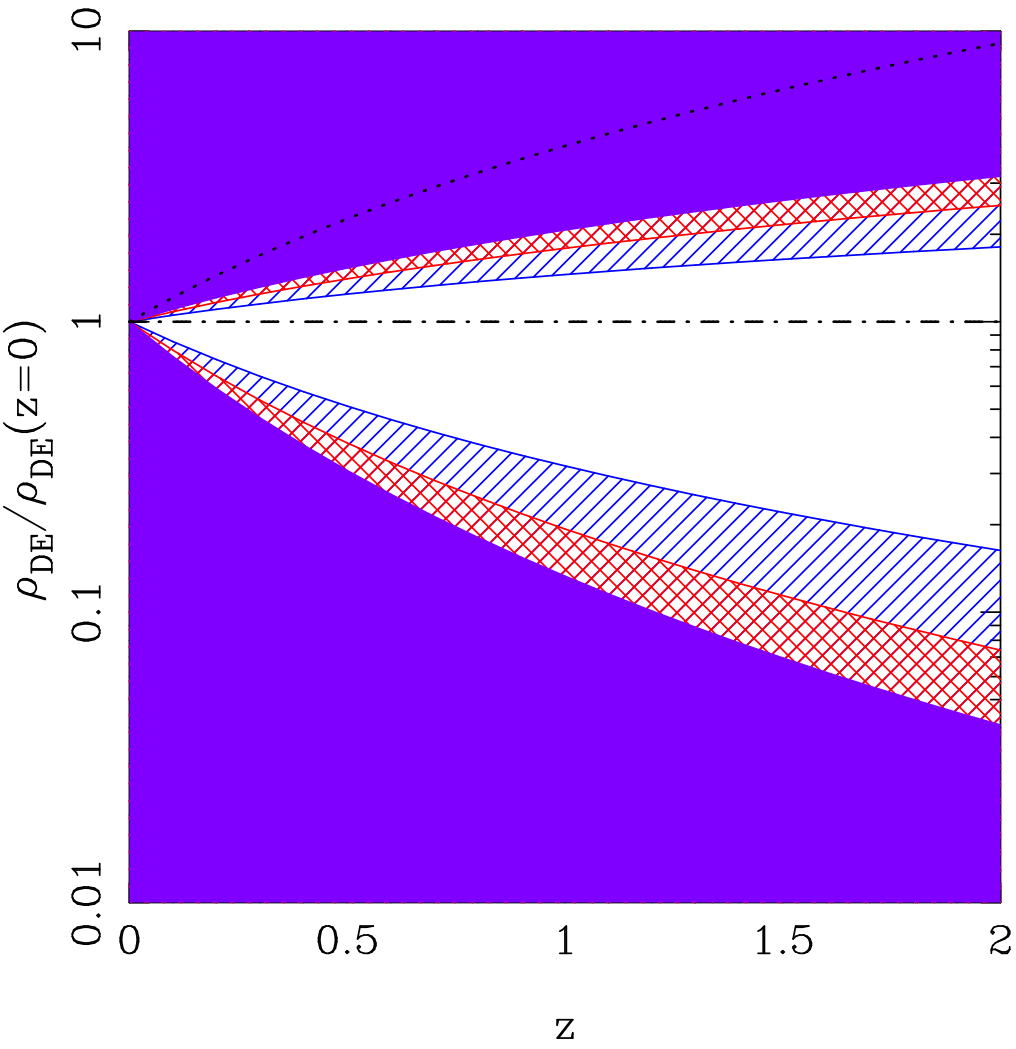

Figure 2.6: The figure represents dark energy density versus redshift for Hubble parameter measurements. The figure is plotted for when we marginalised the present value Hubble parameter. The different region corresponding to white color or blue and red colors with lines show the allowed range of dark energy density at 1σ level, 2σ and 3σ ranges respectively. The solid blue region is ruled out. The dotted line corresponds to $w = -1/3$ and the dotted-dashed line is drawn for $w = -1$, cosmological constant.

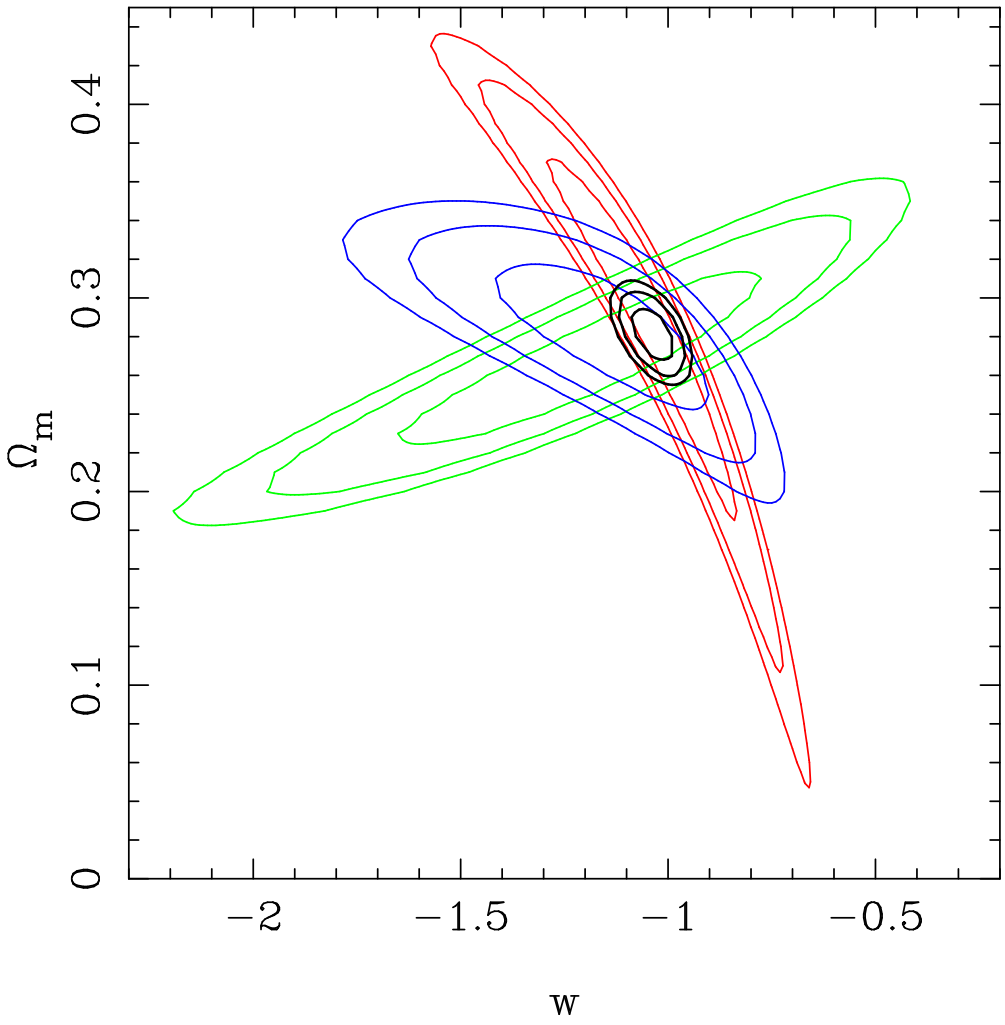

Figure 2.7: The figure represents 1σ, 2σ and 3σ confidence contours obtained from the analysis from the combination of all the three data sets in Ω_m-w plane. The contours in red, green and blue corresponds to constraints from SNIa, BAO and Hz data sets respectively. The black contours are the constraints obtained by combination of the data sets. In the figure, the contours for SNIa and BAO are obtained for H_0=70 $km/s/Mpc$, for Hz data we have marginalised over the value of Hubble constant.

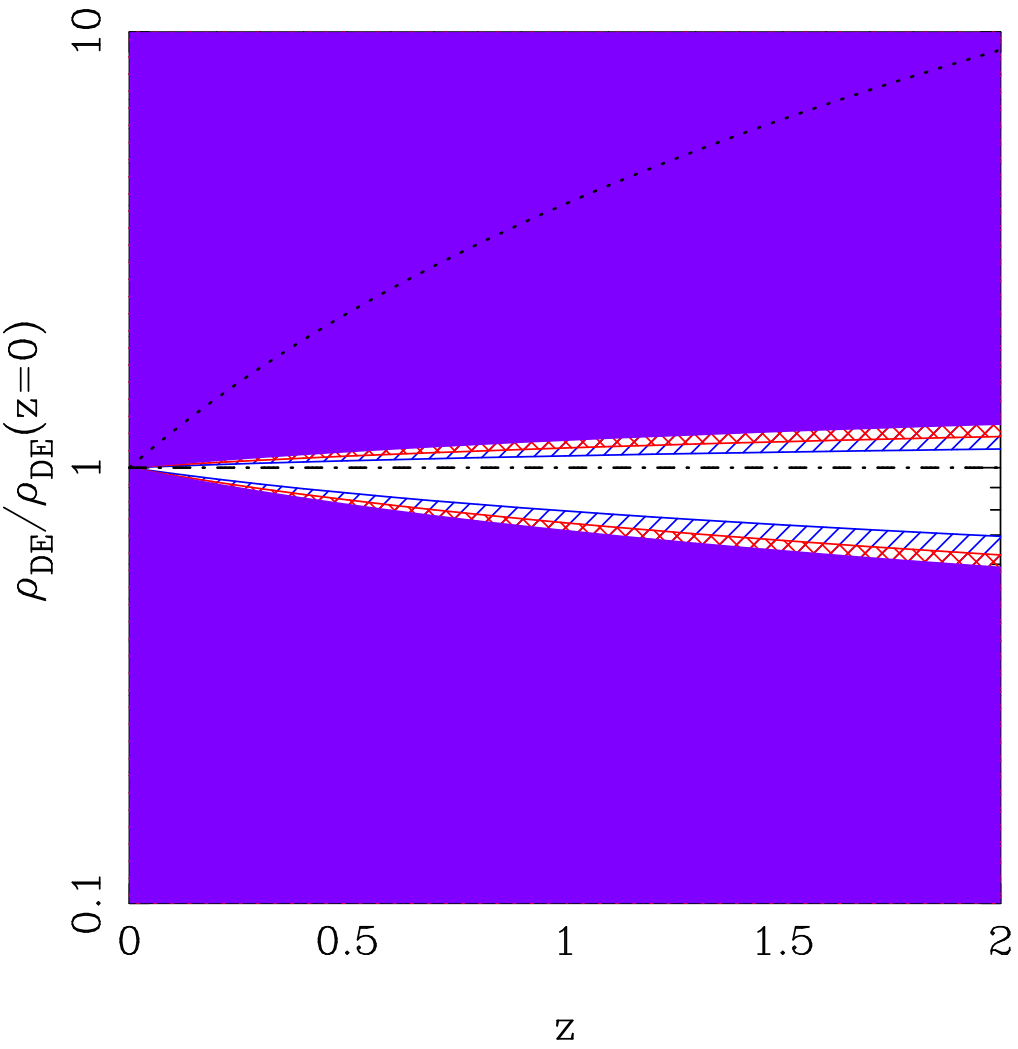

Figure 2.8: The figure represents dark energy density versus redshift for the combined analysis of all the data sets. The figure is plotted for $H_0 = 70\ km/s/Mpc$ for SNIa and BAO data while for Hz data we have marginalised over the range of H_0. The figure shows the allowed range of dark energy density at 1σ level, 2σ and 3σ ranges. The colour scheme in the figure is same as in 2.2 and 2.4. The solid blue region is ruled out. The dotted line corresponds to $w = -1/3$ and the dotted-dashed line is drawn for $w = -1$, cosmological constant.

Parameter	Lower Limit	Upper Limit
Ω_m	0.1	0.6
w_0	-5.0	2.0
$w'(z=0)$	-10.0	10.0
H_0	65.0	75.0

Table 2.2: This table lists the priors used in the parameter fitting, when w is a function of redshift.

the $H(z)$, SNIa, and BAO data we compute:

$$\chi^2(\mathbf{p}) = \chi^2_H(\mathbf{p}) + \chi^2_{SN}(\mathbf{p}) + \chi^2_{BAO}(\mathbf{p}) \tag{2.11}$$

for each of the three cosmological models considered here. We minimize $\chi^2(\mathbf{p})$ with respect to model parameters $\mathbf{p}$ to get best-fit parameter values $\mathbf{p_0}$ and constraint contours.

Figure 2.7 shows constraints on the cosmological parameters for the wCDM, from a joint analysis of the BAO, SNIa and $H(z)$ data. The minimum χ^2 for the case $H_0 = 70$ $km/s/Mpc$ is 580.81 corresponding to $\Omega_m = 0.28$ and $w = -1.03$. The allowed range for matter density is $0.25 < \Omega_m < 0.31$ and for equation of state parameter is $-1.13 < w < -0.95$. The contours (corresponding to $H_0 = 70$ $km/s/Mpc$) is consistent with cosmological model within 3σ confidence level. As the present value of Hubble parameter increases, the models prefers the phantom models and allows larger negative values of equation of state parameters. The figure 2.8 represents the variation in dark energy density as a function of redshift for the combined analysis of all the data sets. The figure is plotted for $H_0 = 70$ $km/s/Mpc$. The different region corresponding to white color or blue and red colors with lines show the allowed range of dark energy density at 1σ level, 2σ and 3σ ranges respectively. The solid blue region is ruled out. The dotted line corresponds to $w = -1/3$ and the dotted-dashed line is drawn for $w = -1$, cosmological constant. Here, we see that for $H_0 = 70$ $km/s/Mpc$ the cosmological model is allowed.

2.2 Chevallier-Polarski-Linder (CPL) model

The evolution of dark energy is determined by its equation of state (EoS), which can be obtained in a particular model or constructed directly from observational data. In the second case, we usually make some assumptions on the form of the equation of state as a parameterization for the dark energy model, then extract the information from observations. A most wildly used parameterization is called the Chevallier-Polarski-

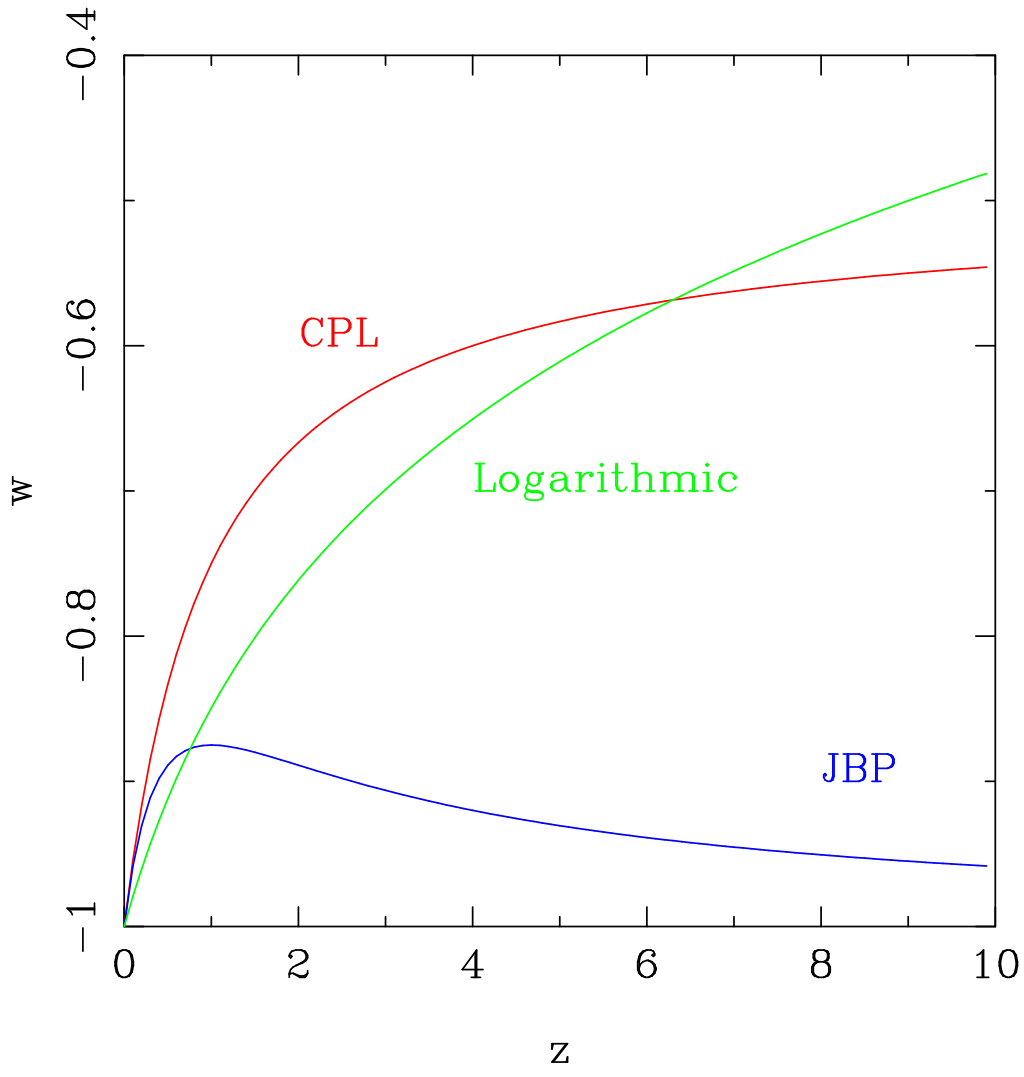

Figure 2.9: The figure represents equation of state of dark energy as a function of redshift for the three types of parameterizations considered. The red line is plotted for $w(z) = w_0 + w'(z = 0)\frac{z}{(1+z)}$ (CPL) parameterization. The blue line is drawn for $w(z) = w_0 + w'(z = 0)\frac{z}{(1+z)}$ parameterization and the green line represents the Logarithmic parameterization.

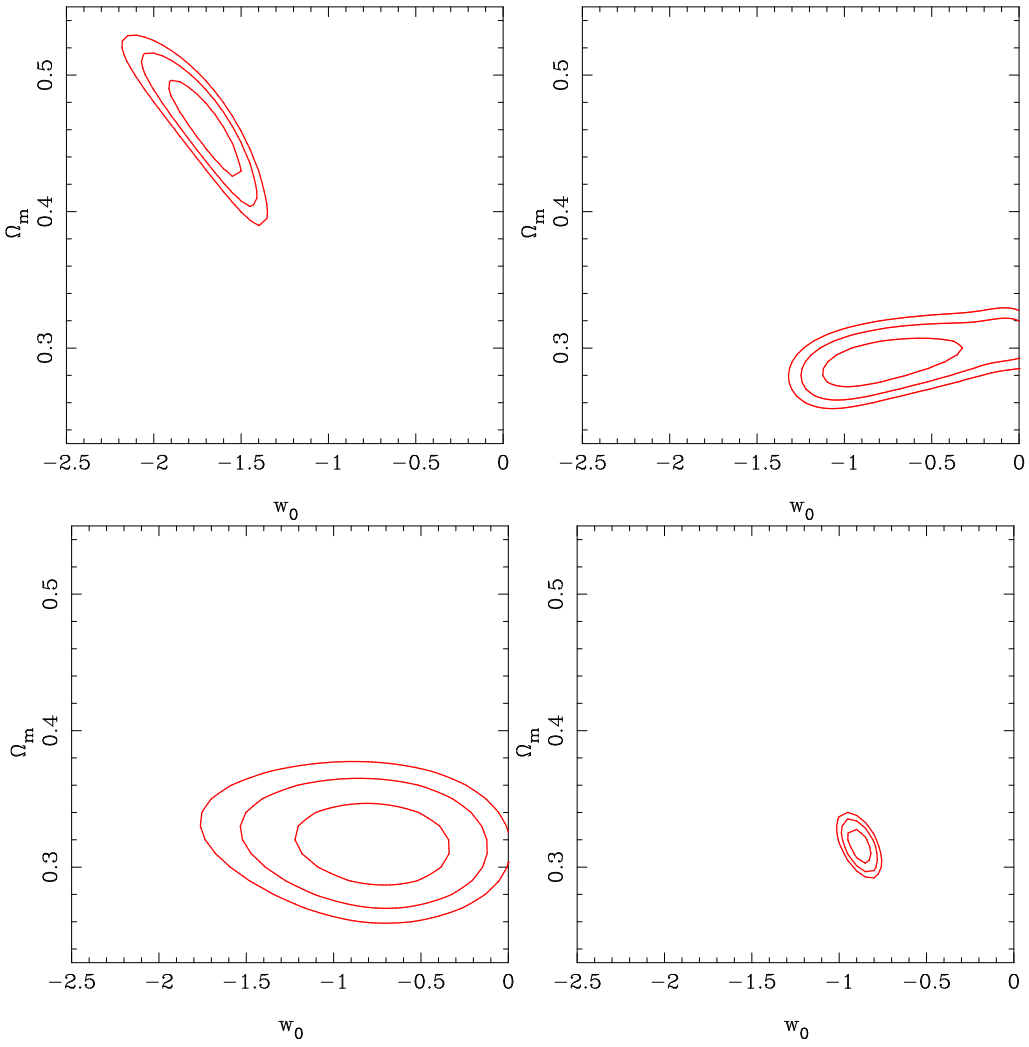

Figure 2.10: The plots represent the confidence contours for SNIa, BAO, H(z) and a combination of the datasets for the CPL parameterization with marginalization over w'. The top left and top right contours are obtained for SNIa and BAO data sets and the bottom left and bottom right contours are obtained for H(z) data and a combination of data sets.

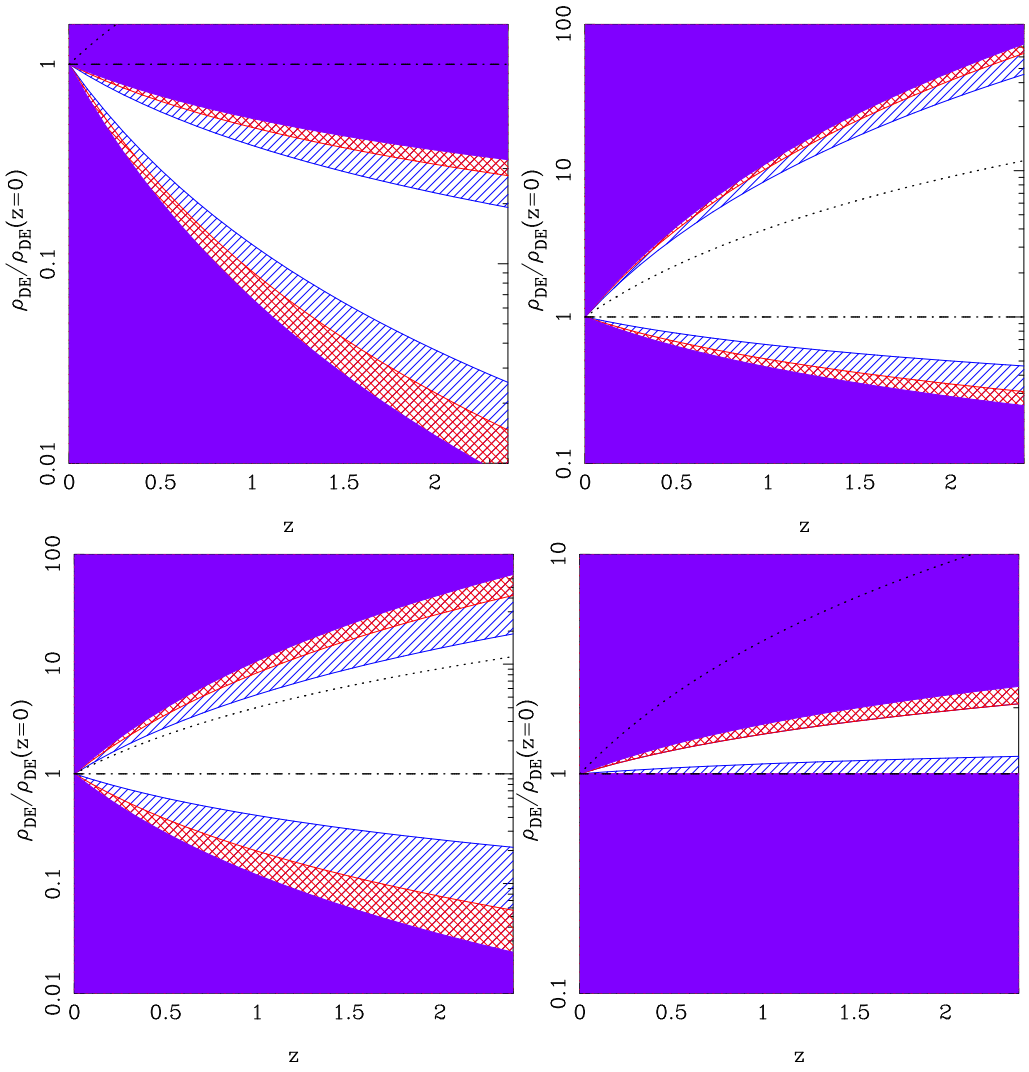

Figure 2.11: The plots represent the variation of dark energy density as a function of redshift allowed at 1, 2 and 3-σ confidence levels for the CPL parameterization with marginalization over w'. The scheme of the plots is same as in Fig. 2.10.

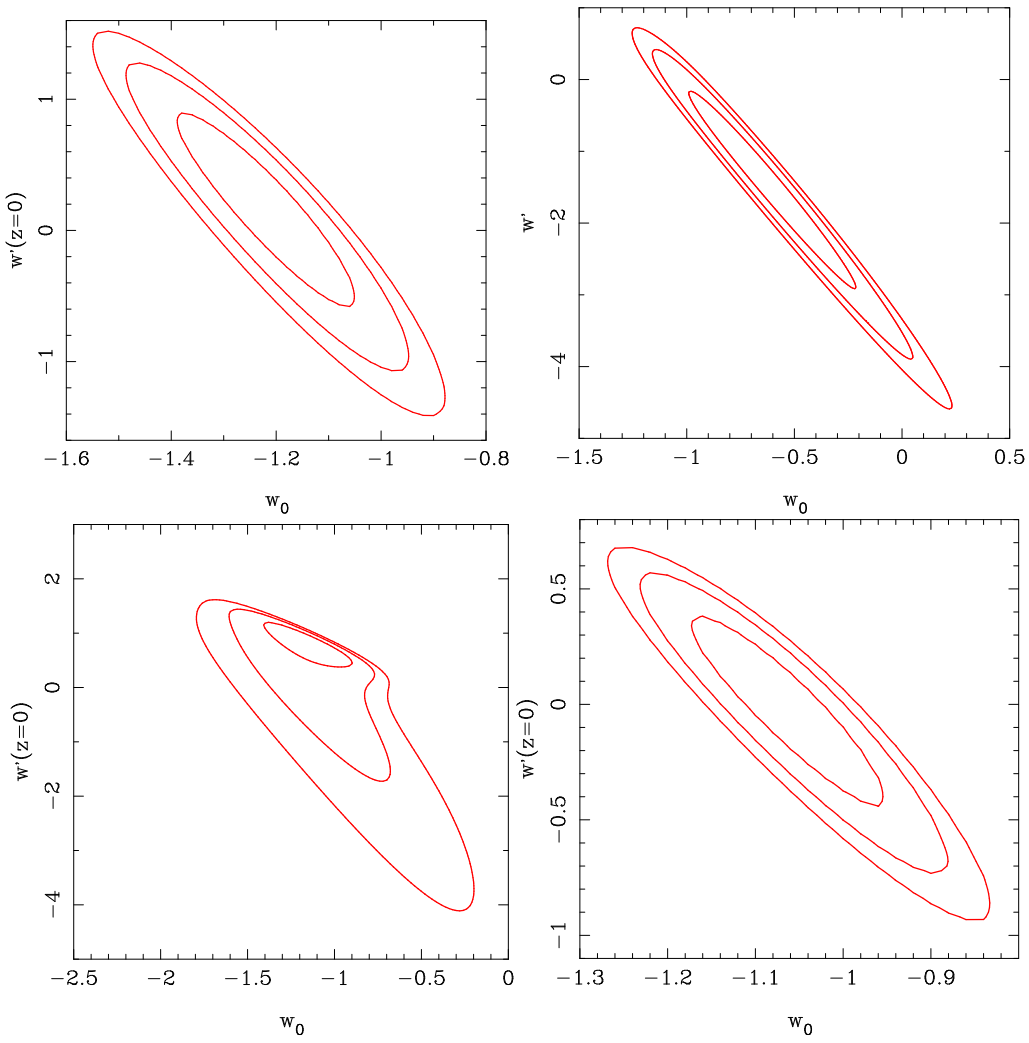

Figure 2.12: The plots represent the confidence contours for SNIa, BAO, H(z) and a combination of the datasets for the $w(z) = w_0 + w'(z=0)\frac{z}{(1+z)}$ parameterization with marginalization over Ω_m. The scheme of the plots is same as in figure 2.10.

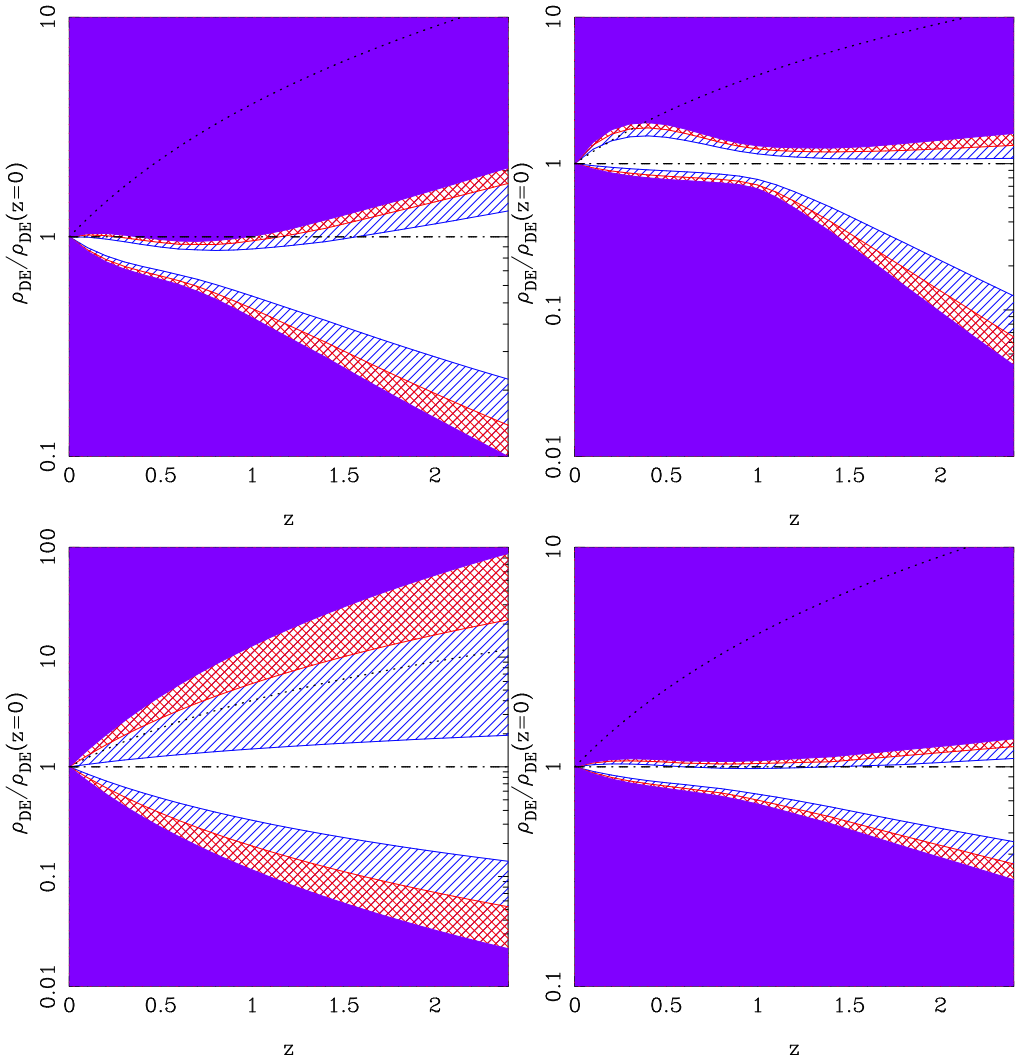

Figure 2.13: The plots show the allowed range of dark energy density by SNIa, BAO, H(z) and a combined datasets for the Chevallier-Polarski-Linder (CPL) parameterization with marginalization over Ω_m.

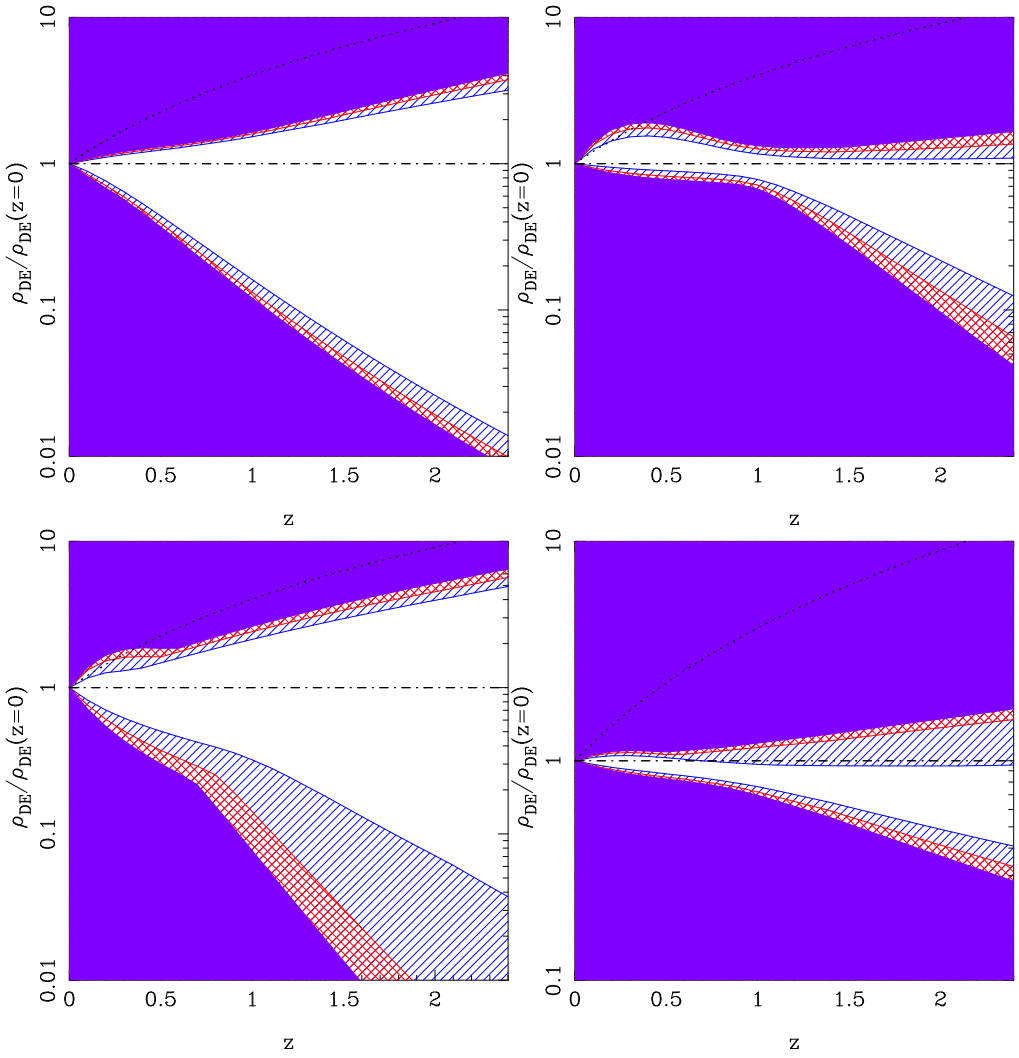

Figure 2.14: The plots show the allowed range of dark energy density by SNIa, BAO, H(z) and a combined datasets for the Chevallier-Polarski-Linder (CPL) parameterization. All the parameters are free parameters. No marginalisation has been done.

Linder (CPL) model [15, 16] with the form of equation of state as

$$w(z) = w_0 + w'(z=0)\frac{z}{(1+z)} \tag{2.12}$$

where w_0 is the value of equation of state parameter at present and $w'(z=0)$ is the first order derivative of $w(z)$ at $z = 0$. The evolution of equation of state parameter as a function of redshift is shown in figure 2.9. The CPL parameterization is well behaved and bounded at high redshifts. The asymptotic value of w(z) at high redshifts is $w(z = \infty) = w_0 + w'$. The present value of the equation of state parameter is $w(0) = w_0$ for this parameterization. This is the direct motivation of proposing such a form. The evolution of dark energy density ($\rho_{_{DE}}$) with the expansion of the universe for this equation of state parameter is then given by

$$\frac{\rho_{_{DE}}}{\rho_{_{DE_0}}} = (1+z)^{3(1+w_0+w')}\ exp\Big[-\frac{3w'z}{1+z}\Big]. \tag{2.13}$$

Here, $\rho_{_{DE_0}} \equiv \rho_{_{DE}}(z=0)$, which is the present value of dark energy density, and $w' \equiv dw/dz$ at the present time. For the analysis, the priors used in this case is listed in table 2.2. For the rest of the chapter, the same priors will be used. In this case, the free parameters are Ω_m, w_0 and $w'(z=0)$ or just w'. To get contours between two parameters, we will make use of the marginalization technique (discussed in previous chapter). By using this technique, we can get a plot between two parameters by performing summation over the third parameter. The figure 2.10 shows the contours in $w_0 - \Omega_m$ planes, which are obtained by marginalization over parameter $w(z = 0)$. The plots represent the confidence contours for SNIa, BAO, H(z) and a combination of the datasets for the CPL parameterization. The top left and top right contours are obtained for SNIa and BAO data sets and the bottom left and bottom right contours are obtained for H(z) data and a combination of data sets. SNIa data favours the phantom model and does not allow ΛCDM model, also it allows higher values of Ω_m than any other data sets. BAO and H(z) data both agrees with cosmological constant model. The allowed range in case of combined constraints are very narrow. The figure 2.11 represents the variation of dark energy density as a function of redshift allowed at 1, 2 and 3 -σ confidence levels for the CPL parameterization with marginalization over w'. The plot scheme is same as in figure 2.10. The top left plot, obtained from analysis of SNIa data does not allow the cosmological constant model. This follows from the contours for SNIa data given in previous figure2.10. Because of this result of SNIa data, the allowed range obtained from combined analysis of all the data sets does not allow cosmological constant within 1σ region.

Now, we marginalise over Ω_m to obtain contours in $w_0 - w'(z=0)$ plane. The plots in figure 2.12 represent the confidence contours for SNIa, BAO, H(z) and a combination of the datasets for the $w(z) = w_0 + w'(z=0)\frac{z}{(1+z)}$ parameterization with marginalization over Ω_m. The scheme of the plots is same as in figure 2.10. The tightest constraints are obtained for SNIa data set. The figure 2.13 shows the allowed range of dark energy density by individual data sets and a combined datasets for the Chevallier-Polarski-Linder (CPL) parameterizations with marginalization over Ω_m. Here, we see that SNIa data does not allow cosmological constant model at lower redshifts while BAO data does not allow it at higher redshifts within 1σ region. Only H(z) data is consistent with ΛCDM model at all the redshift range that is shown in the plot.

In figure 2.14 the plots show the allowed range of dark energy density by the different observations and a combination of observations for the $w(z) = w_0 + w'(z=0)\frac{z}{(1+z)}$ parameterization. All the parameters are free parameters. No marginalisation has been done to obtain these results. The allowed range in unmarginalised case is larger than in case of marginalised ones. BAO data is not consistent with ΛCDM model at higher redshift within 1σ region, which effects the combined constraints also. Supernovae and H(z) data is consistent with cosmological constant model for the entire range of redshift considered.

2.3 Jassal-Bagla-Padmanabhan(JBP) parameterization

The equation of state parameter w(z) is given by Jassal *et al.*[17] as

$$w(z) = w_0 + w'(z=0)\frac{z}{(1+z)^2}. \tag{2.14}$$

The evolution of equation of state parameter as a function of redshift is shown in figure 2.9. The asymptotic value of w(z) at high redshifts is $w(z=\infty) = w_0$ [17], while the present value of the equation of state parameter is $w(0) = w_0$. The evolution of dark energy density ($\rho_{_{DE}}$) with the expansion of the universe for the above equation of state parameter is then given by

$$\frac{\rho_{_{DE}}}{\rho_{_{DE_0}}} = (1+z)^{3(1+w_0)}\ exp\Big[\frac{3w'}{2}\left(\frac{z}{1+z}\right)^2\Big] \tag{2.15}$$

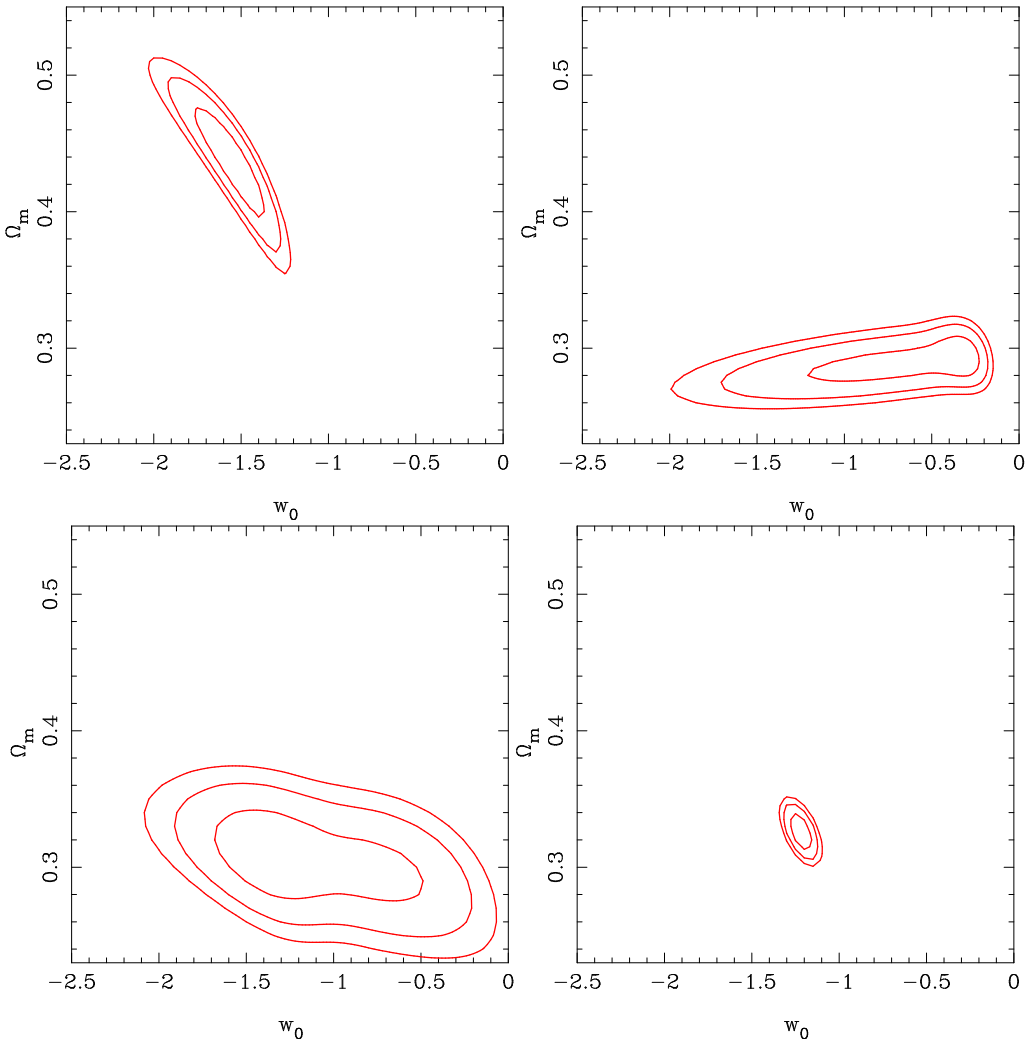

Figure 2.15: The plots represent the confidence contours for SNIa, BAO, H(z) and a combination of the datasets for $w(z) = w_0 + w'(z = 0)\frac{z}{(1+z)^2}$ parameterization with marginalization over w'. The top left and top right contours are obtained for SNIa and BAO data sets and the bottom left and bottom right contours are obtained for H(z) data and a combination of data sets.

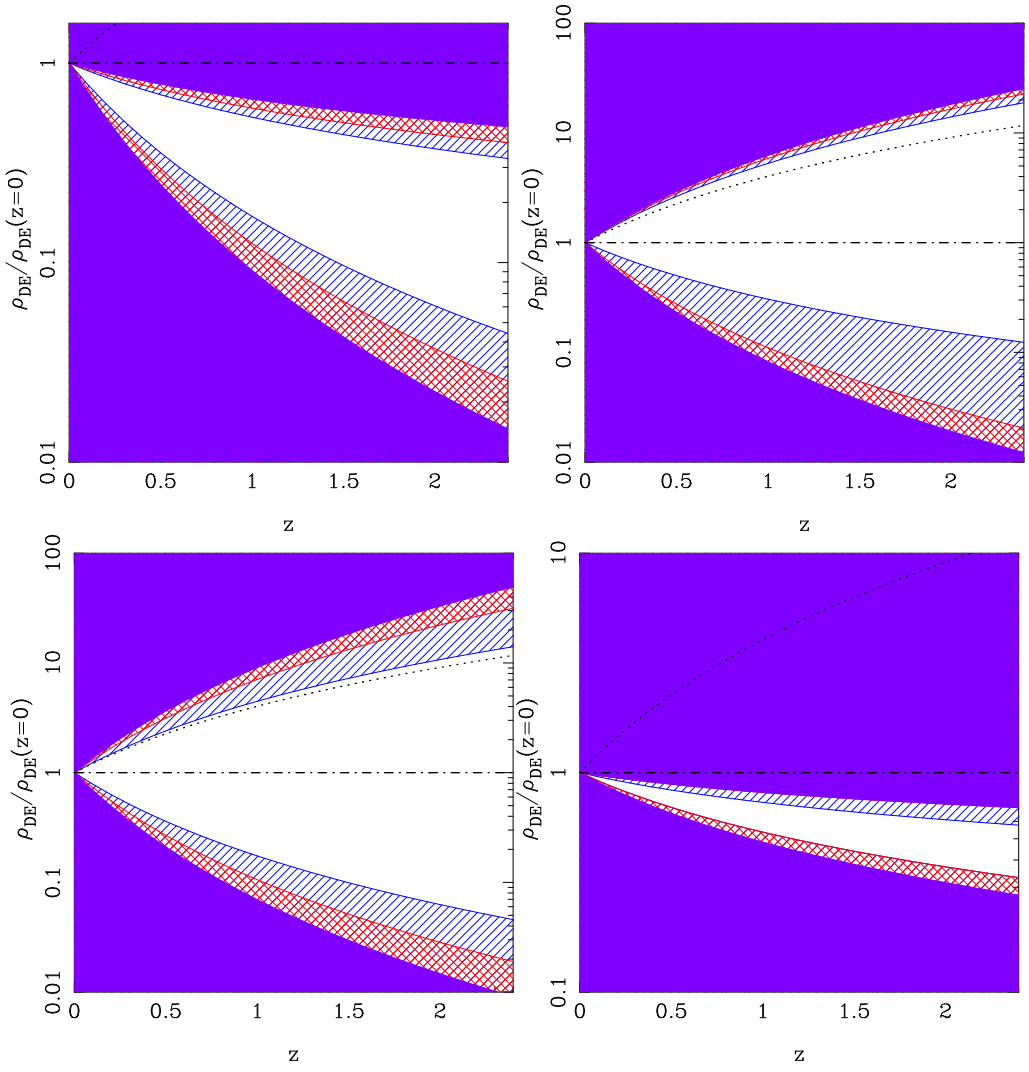

Figure 2.16: The plots represent the variation of dark energy density as a function of redshift allowed at 1, 2 and 3 -σ confidence levels for the $w(z) = w_0 + w'(z=0)\frac{z}{(1+z)^2}$ parameterization with marginalization over w'. The plot scheme is same as in previous figure (Fig. 2.15).

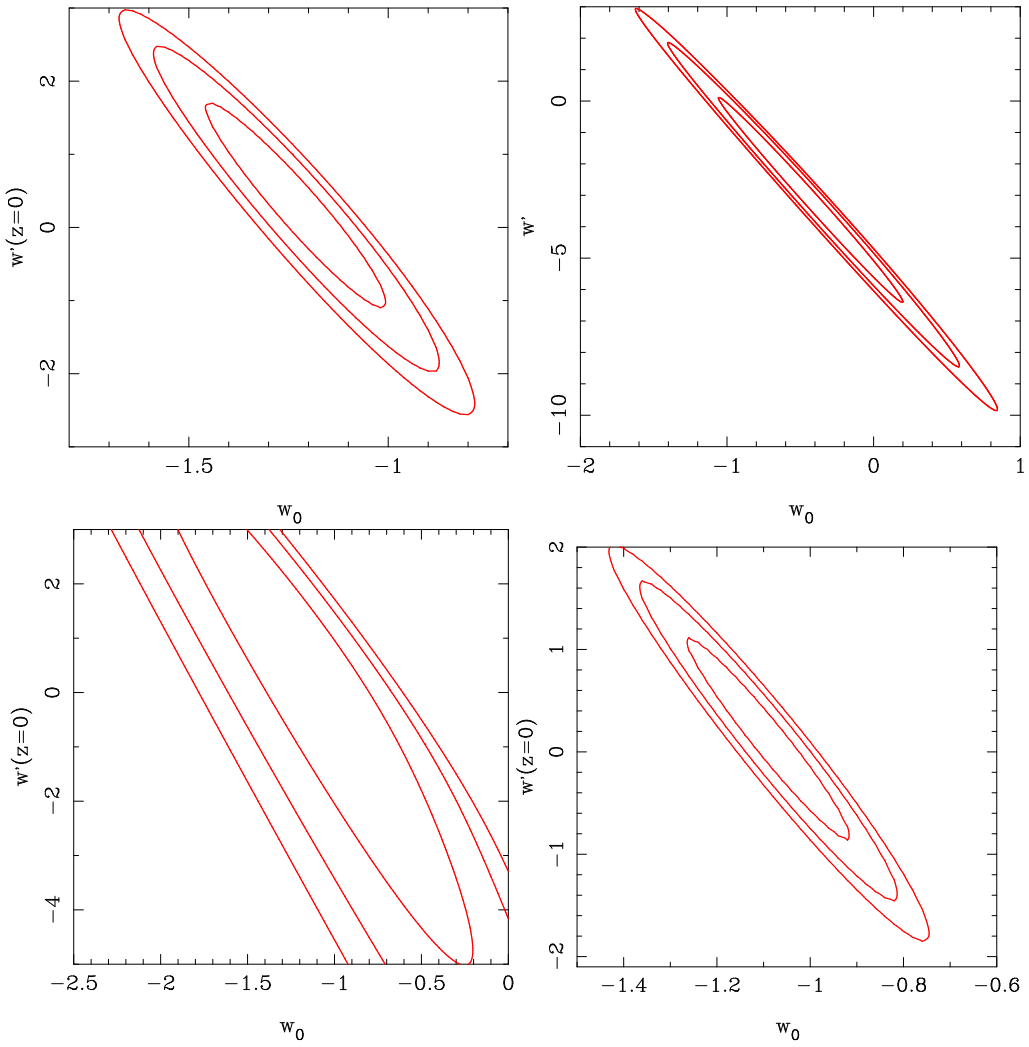

Figure 2.17: The plots represent the confidence contours for SNIa, BAO, H(z) and a combination of the datasets for the JBP parameterization with marginalization over Ω_m. The scheme of the plots is same as in figure 2.15.

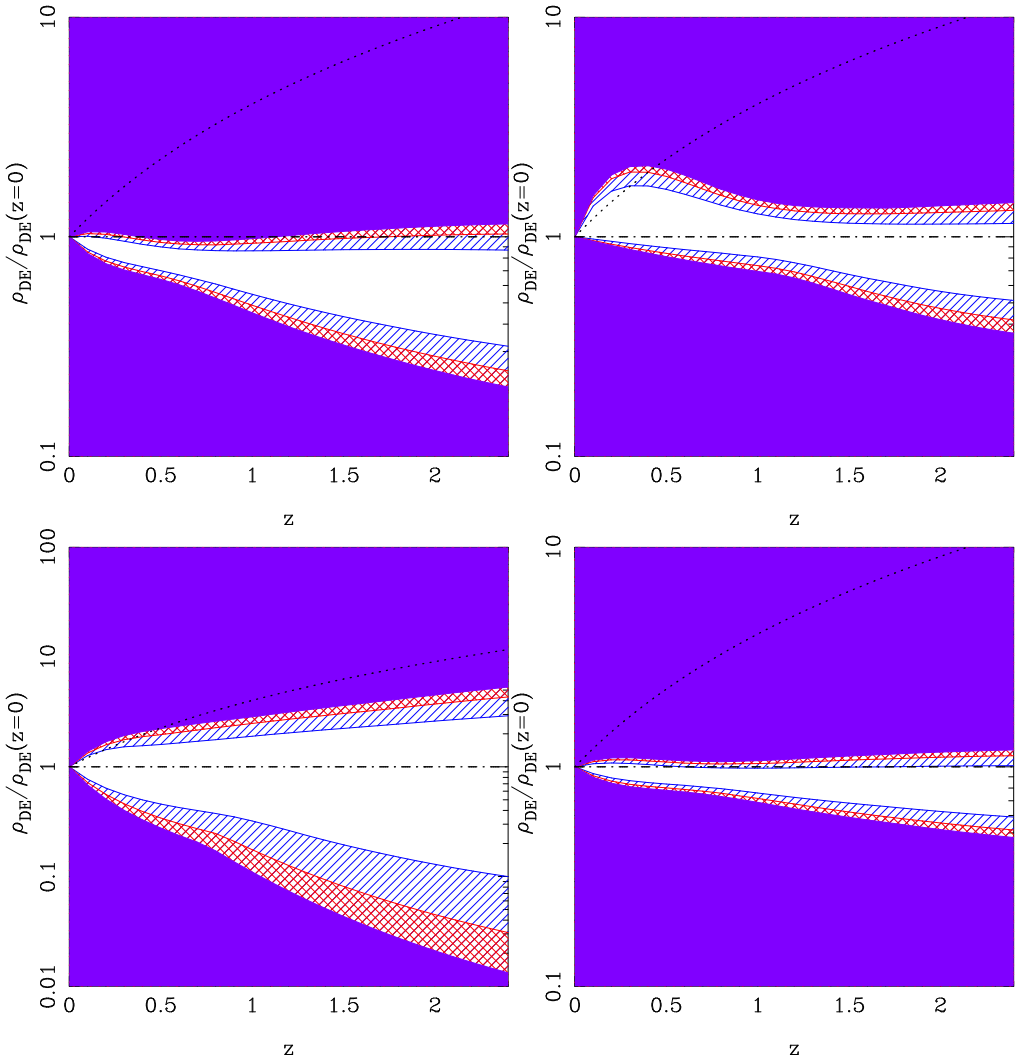

Figure 2.18: The plots show the allowed range of dark energy density by SNIa, BAO, H(z) and a combined datasets for the JBP parameterization with marginalization over Ω_m.

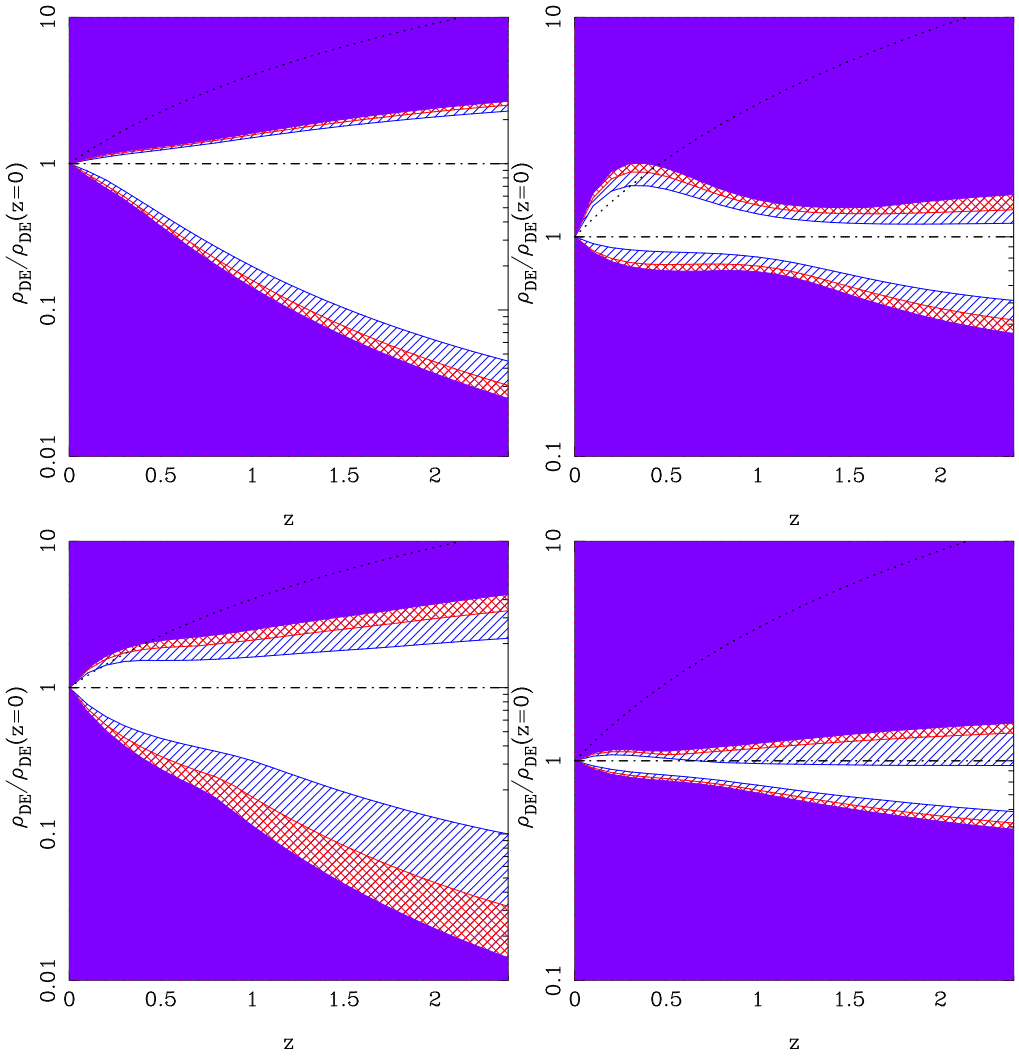

Figure 2.19: The plots show the allowed range of dark energy density by SNIa, BAO, H(z) and a combined datasets for the $w(z) = w_0 + w'(z=0)\frac{z}{(1+z)^2}$. parameterization. All the parameters are free parameters. No marginalisation has been done.

Here, $\rho_{DE_0} \equiv \rho_{DE}(z=0)$, which is the present value of dark energy density, and $w' \equiv dw/dz$ at the present time. The figure 2.15 shows the contours in $w_0 - \Omega_m$ planes, which are obtained by marginalization over parameter $w(z=0)$. The plots represent the confidence contours for SNIa, BAO, H(z) and a combination of the datasets for the JBP parameterization. The top left and top right contours are obtained for SNIa and BAO data sets and the bottom left and bottom right contours are obtained for H(z) data and a combination of data sets. SNIa data favours the phantom model and does not allow ΛCDM model, also it allows higher values of Ω_m than any other data sets. BAO and H(z) data both agrees with cosmological constant model. The allowed range in case of combined constraints are very narrow. The figure 2.16 represents the variation of dark energy density as a function of redshift allowed at 1, 2 and 3 -σ confidence levels for the JBP parameterization with marginalization over w'. The plot scheme is same as in figure 2.10. The top left plot, obtained from analysis of SNIa data does not allow the cosmological constant model and prefers phantom model. This follows from the contours for SNIa data shown in figure2.15. All other data sets are consistent with the ΛCDM model. Because of this result of SNIa data, the allowed range obtained from combined analysis of all the data sets doesnot allow cosmological constant within 3σ region.

So far we have shown the results obtained by performing marginalisation over w', now, we marginalise over Ω_m to obtain contours in $w_0 - w'(z=0)$ plane. The plots in figure 2.17 represent the confidence contours for SNIa, BAO, H(z) and a combination of the datasets for the $w(z) = w_0 + w'(z=0)\frac{z}{(1+z)^2}$ parameterization with marginalization over Ω_m. The scheme of the plots is same as in figure 2.15. The tightest constraints are obtained for SNIa data set.

The figure 2.18 shows the allowed range of dark energy density by SNIa, BAO, H(z) and a combined datasets for the JBP parameterizations with marginalization over Ω_m. SNIa data does not allow cosmological constant model at higher redshifts within 1σ region. This effect can also be seen in combined constraints where, within 1σ region, ΛCDM model is not consistent with observations at higher redshifts.

In figure 2.19 the plots show the allowed range of dark energy density by the different observations and a combination of observations for the $w(z) = w_0 + w'(z=0)\frac{z}{(1+z)^2}$ parameterization. All the parameters are kept free parameters. The allowed range in unmarginalised case is larger than in case of marginalised ones. All three data is are consistent with ΛCDM model at all redshifts within 1σ region. However, the combined constraints are not consistent with the cosmological constant model at higher redshifts.

Data set	3σ confidence	χ^2_m	Best Fit Model
$w(z) = w_0 + w'(z=0)\frac{z}{(1+z)}$ Parameterization			
SNIa	-1.64 $\leq w_0 \leq$ -0.72 -2.0 $\leq w'(z=0) \leq$ 1.26 0.2 $\leq \Omega_m \leq$ 0.45	562.25	w_0=-1.0 $w'(z=0)$=0.2 Ω_m=0.25
BAO	-1.3 $\leq w_0 \leq$ 0.33 -4.97 $\leq w'(z=0) \leq$ 0.77 0.3 $\leq \Omega_m \leq$ 0.31	2.13	w_0=-0.67 $w'(z=0)$=-1.26 Ω_m=0.3
H(z)	-2.14 $\leq w_0 \leq$ 0.28 -5.0 $\leq w'(z=0) \leq$ 1.8 0.1 $\leq \Omega_m \leq$ 0.37	20.77	w_0=-1.16 $w'(z=0)$=0.8 Ω_m=0.2
SNIa+BAO+H(z)	-1.2 $\leq w_0 \leq$ -0.74 -1.32 $\leq w'(z=0) \leq$ 0.56 0.25 $\leq \Omega_m \leq$ 0.3	585.67	w_0=-1.0 $w'(z=0)$=-0.26 Ω_m=0.3
$w(z) = w_0 + w'(z=0)\frac{z}{(1+z)^2}$ Parameterization			
SNIa	-1.62 $\leq w_0 \leq$ -0.62 -3.0 $\leq w'(z=0) \leq$ 2.56 0.2 $\leq \Omega_m \leq$ 0.45	562.28	w_0=-1.06 $w'(z=0)$=-0.06 Ω_m=0.3
BAO	-1.68 $\leq w_0 \leq$ 0.99 -10.0 $\leq w'(z=0) \leq$ 2.99 0.25 $\leq \Omega_m \leq$ 0.3	2.79	w_0=-0.44 $w'(z=0)$=-3.06 Ω_m=0.3
H(z)	-2.36 $\leq w_0 \leq$ 0.24 -5.8 $\leq w'(z=0) \leq$ 3.4 0.18 $\leq \Omega_m \leq$ 0.37	21.11	w_0=-1.16 $w'(z=0)$=0.3 Ω_m=0.28
SNIa+BAO+H(z)	-1.36 $\leq w_0 \leq$ -0.64 -2.52 $\leq w'(z=0) \leq$ 1.62 0.25 $\leq \Omega_m \leq$ 0.3	586.46	w_0=-1.0 $w'(z=0)$=-0.38 Ω_m=0.3

Table 2.3: This table shows the 3σ confidence limit for various data sets for the two parameterization models for $H_0 = 70\ km/s/Mpc$ for BAO and SNIa and for H(z) data, marginalized over H_0. For these results, we have kept Ω_m a free parameter.

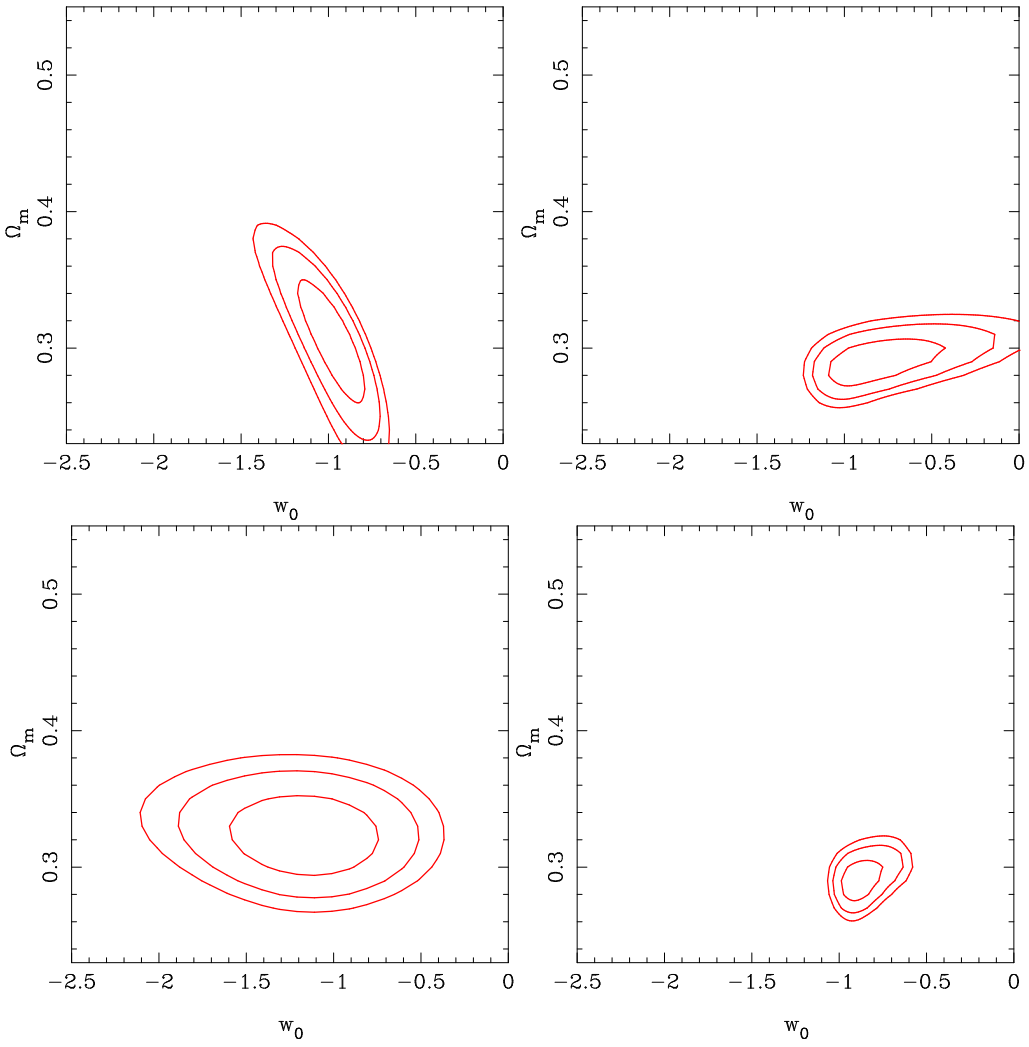

Figure 2.20: The plots represent the confidence contours for SNIa, BAO, H(z) and a combination of the datasets for $w(z) = w_0 + w'(z = 0)log(1 + z)$ parameterization with marginalization over w'. The top left and top right contours are obtained for SNIa and BAO data sets and the bottom left and bottom right contours are obtained for H(z) data and a combination of data sets.

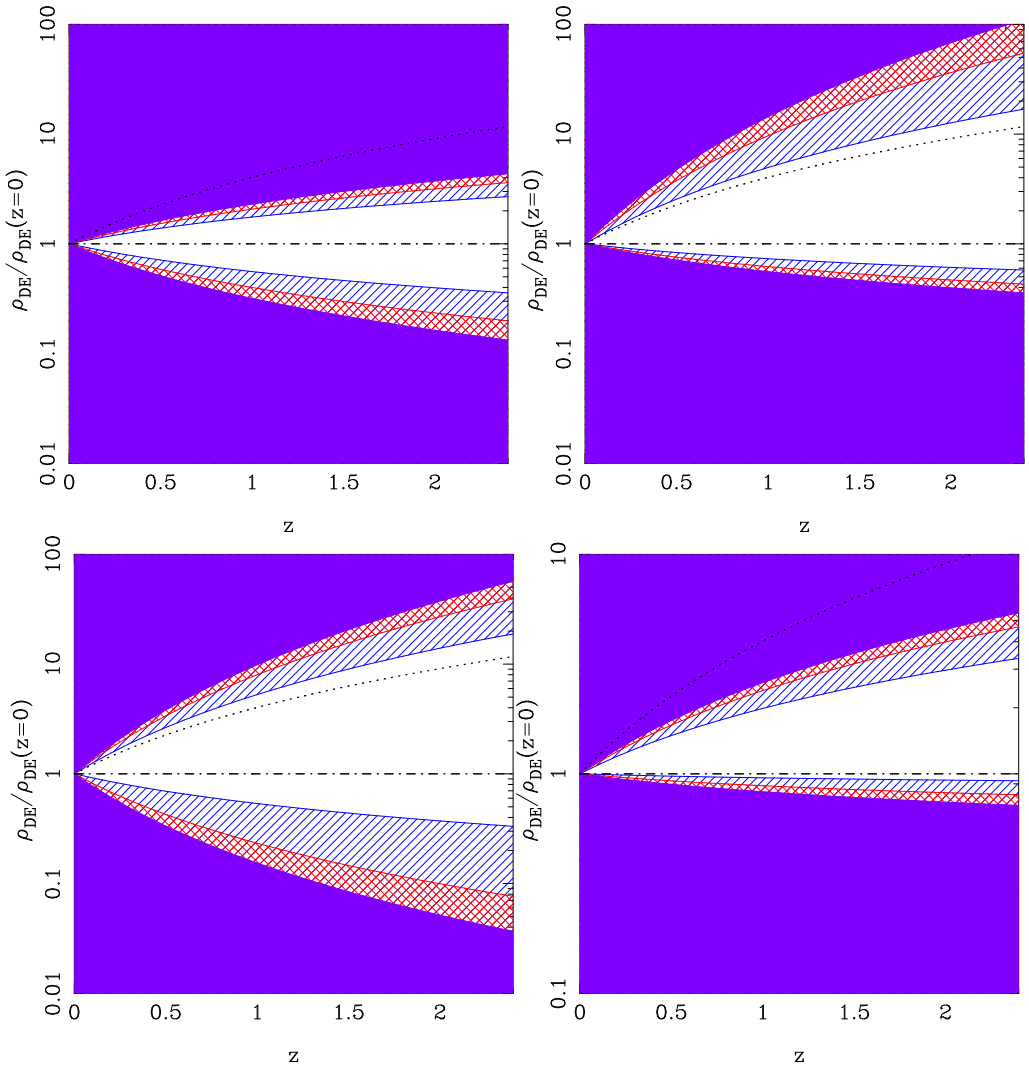

Figure 2.21: The plots represent the variation of dark energy density as a function of redshift allowed at 1, 2 and 3 -σ confidence levels for the Logarithmic parameterization with marginalization over w'. The scheme for the plots is same as in figure 2.20

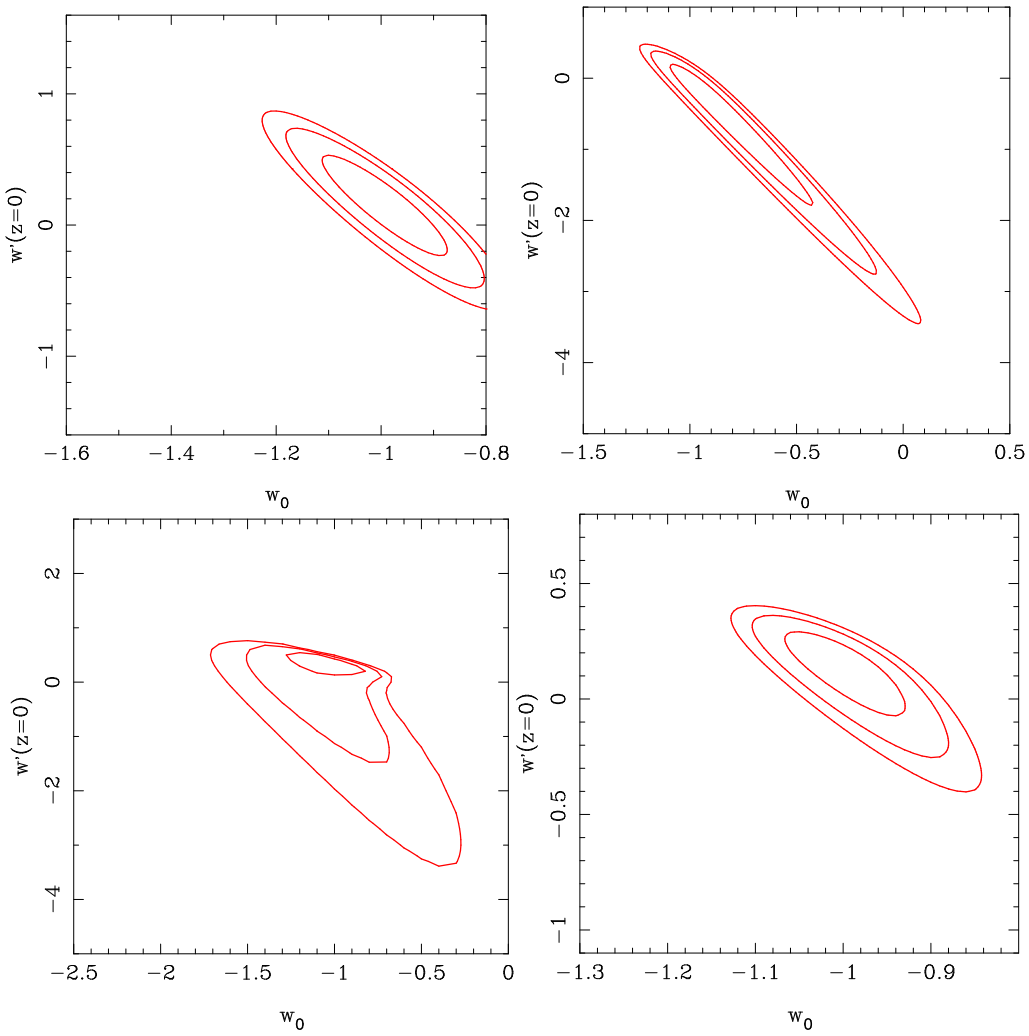

Figure 2.22: The plots represent the confidence contours for SNIa, BAO, H(z) and a combination of the datasets for the Logarithmic parameterization with marginalization over Ω_m. The scheme of the plots is same as in figure 2.20.

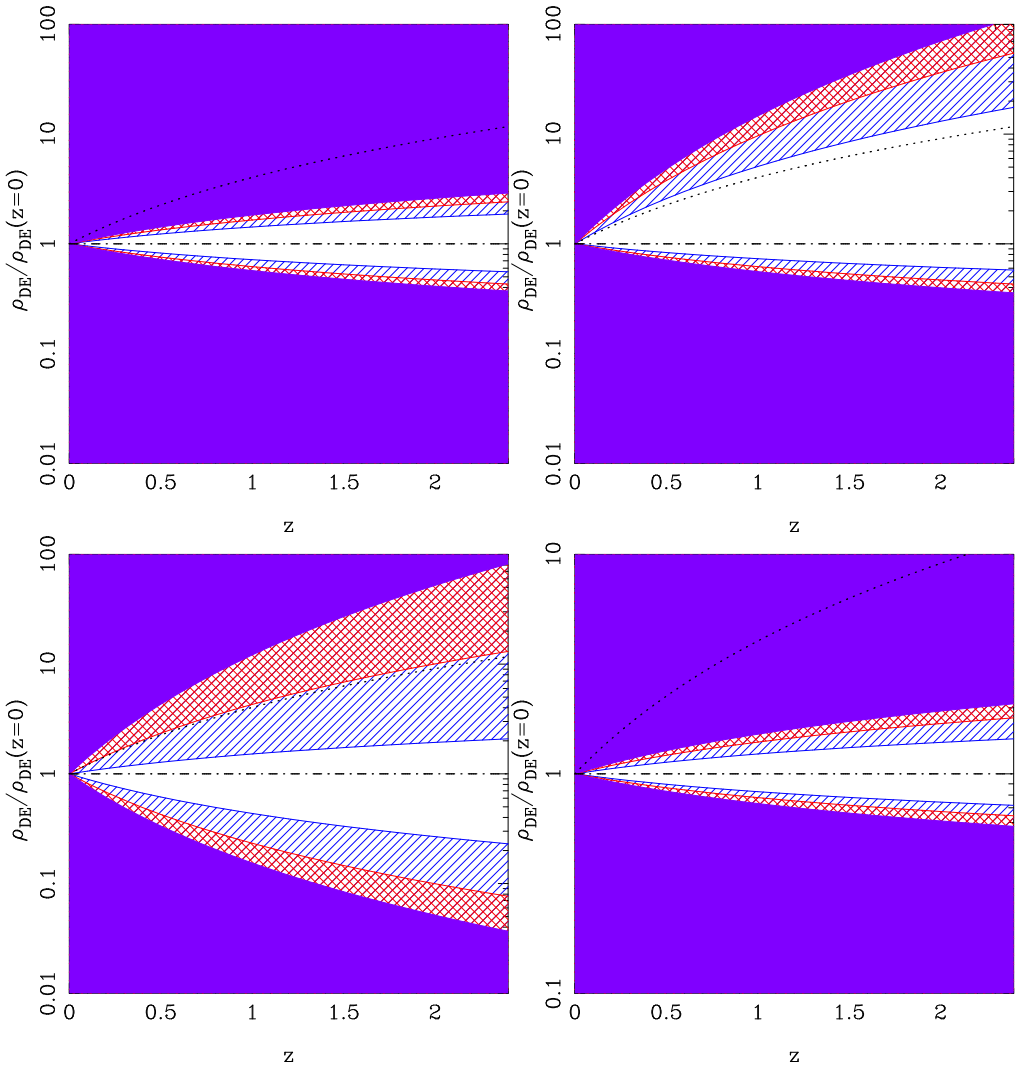

Figure 2.23: The plots show the allowed range of dark energy density by SNIa, BAO, H(z) and a combined datasets for the logarithmic parameterization with marginalization over Ω_m.

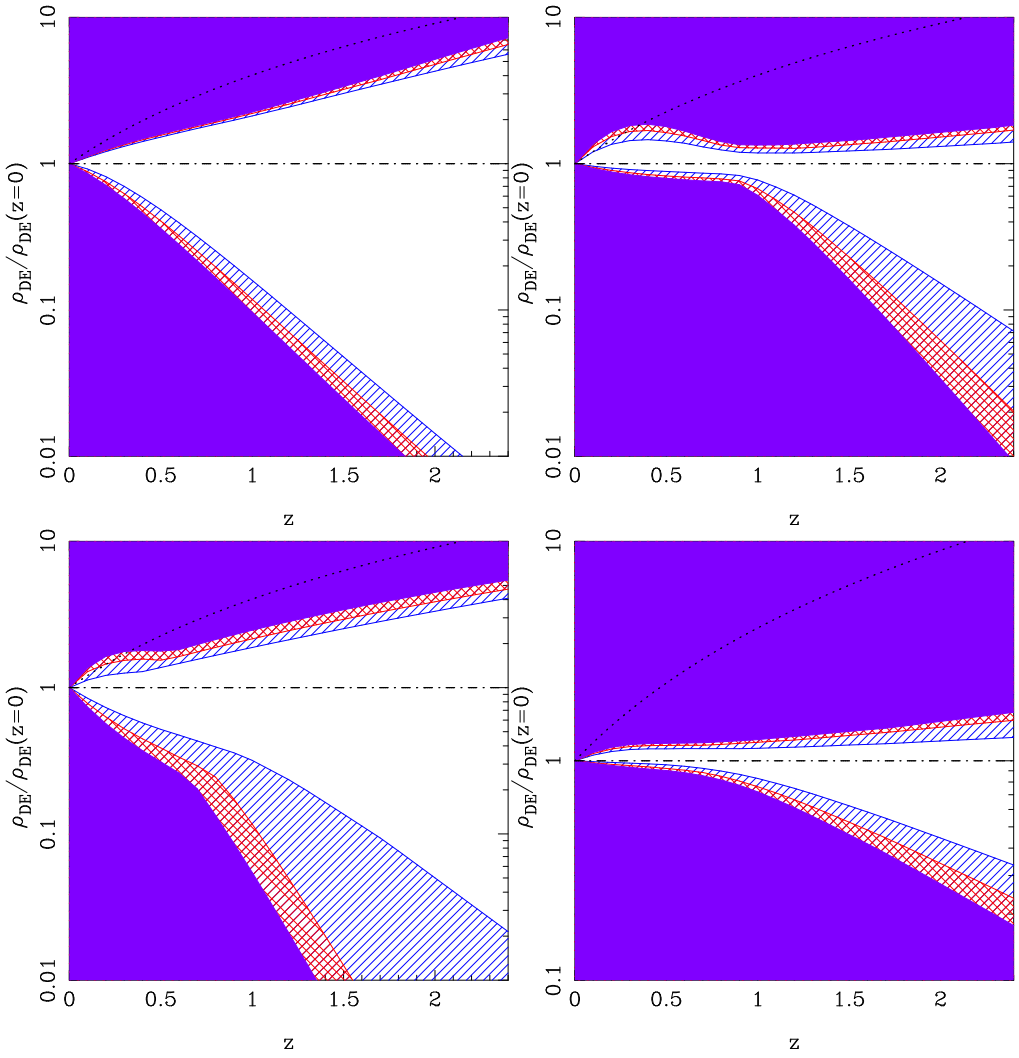

Figure 2.24: The plots show the allowed range of dark energy density by SNIa, BAO, H(z) and a combined datasets for the $w(z) = w_0 + w'(z = 0)log(1 + z)$ parameterization. All the parameters are free parameters. Here, we have not marginalised over any parameter.

Data set	3σ confidence	χ^2_m	Best Fit Model
Logarithmic parameterization			
SNIa	-1.44 $\leq w_0 \leq$ -0.58 -2.0 $\leq w'(z=0) \leq 0.68$ $0.1 \leq \Omega_m \leq 0.49$	563.02	w_0=-0.94 $w'(z=0)$=-1.04 Ω_m=0.37
BAO	-1.26 $\leq w_0 \leq 0.2$ -3.8 $\leq w'(z=0) \leq 0.5$ $0.26 \leq \Omega_m \leq 0.32$	1.29	w_0=-0.84 $w'(z=0)$=-0.5 Ω_m=0.29
H(z)	-2.0 $\leq w_0 \leq 0.2$ -5.0 $\leq w'(z=0) \leq 0.9$ $0.1 \leq \Omega_m \leq 0.37$	20.91	w_0=-1.1 $w'(z=0)$=0.3 Ω_m=0.24
SNIa+BAO+H(z)	-1.09 $\leq w_0 \leq$ -0.66 -1.21 $\leq w'(z=0) \leq 0.25$ $0.26 \leq \Omega_m \leq 0.32$	587.18	w_0=-0.91 $w'(z=0)$=-0.29 Ω_m=0.29

Table 2.4: This table shows the 3σ confidence limit for various data sets for the Logarithmic parameterization model. We consider the present value of Hubble constant to be $H_0 = 70\ km/s/Mpc$ for BAO and SNIa and for H(z) data, marginalized over H_0. For these results, Ω_m a free parameter.

2.4 Logarithmic parameterization

The equation of state parameter in this case is given by

$$w(z) = w_0 + w'(z=0)log(1+z) \tag{2.16}$$

The equation of state parameter increases monotonically for the logarithmic parameterization [18]. The present value of the equation of state parameter is $w(z=0) = w_0$. The evolution of equation of state parameter versus redshift is shown in figure 2.9. The evolution of dark energy density ($\rho_{_{DE}}$) with redshift for the logarithmic equation of state parameters is given by

$$\frac{\rho_{_{DE}}}{\rho_{_{DE_0}}} = (1+z)^{3(1+w_0)}\ exp\Big[\frac{3w'(z=0)}{2}log^2(1+z)\Big]. \tag{2.17}$$

The figure 2.15 shows the contours in $w_0 - \Omega_m$ planes, which are obtained by marginalization over parameter $w(z=0)$. The plots represent the confidence contours for SNIa, BAO, H(z) and a combination of the datasets for the logarithmic parameterization. The top left and top right contours are obtained for SNIa and BAO data sets and the bottom

left and bottom right contours are obtained for H(z) data and a combination of data sets. All the data sets (SNIa, BAO and H(z) data sets) agrees with cosmological constant model. The allowed range in case of combined constraints are very narrower than any of the individual data sets. The figure 2.21 represents the variation of dark energy density as a function of redshift allowed at 1, 2 and 3 -σ confidence levels for the logarithmic parameterization with marginalization over w'. The plot scheme is same as in figure 2.20. Unlike previous cases in 2.11 and 2.16 SNIa data does allow the cosmological constant model, also, it provides the tightest constraints out of all the other individual data sets. This follows from the contours for SNIa data shown in figure2.15. All other data sets are consistent with the ΛCDM model. Hence, it is SNIa data that tightens the range in combined constraints.

We now present results obtained by marginalising over Ω_m to obtain contours in $w_0 - w'(z = 0)$ plane. The plots in figure 2.22 represent the confidence contours for SNIa, BAO, H(z) and a combination of the datasets for the Logarithmic parameterization with marginalization over Ω_m. The scheme of the plots is same as in figure 2.15. The tightest constraints are obtained for SNIa data set. The figure 2.23 shows the allowed range of dark energy density by SNIa, BAO, H(z) and a combined datasets for the Logarithmic parameterizations with marginalization over Ω_m. In this case all the observations allow cosmological constant model at all redshifts within 1σ region. And hence in the combined analysis cosmological constant model is completely consistent with the observations.

In figures 2.24 the plots show the allowed range of dark energy density by the different observations and a combination of observations for the logarithmic parameterization. All the parameters are kept free parameters. The allowed range in this case is larger than in case of marginalised ones. All three data is are consistent with ΛCDM model at all redshifts within 1σ region. The combined constraints are also consistent with the cosmological constant model at higher redshifts.

Chapter 3

Scalar field models of dark energy

To study dynamics due to a varying equation of state parameters, various scalar field models have been proposed. These were originally postulated to circumvent the fine tuning problem of the cosmological constant model. These include scalar field models such as quintessence [22, 23, 27, 59, 60, 61, 62], k-essence [63, 64] and others include fluid models, barotropic [58, 65] as well as the Chaplygin gas [66]. Any scalar field model can be rewritten as fluid dark energy model or vice-verse [67]. In this chapter, we consider models described by a slowly varying canonical scalar field, i.e., quintessence model. For a slowly varying field, where the field potential dominates, the universe experiences a positive acceleration to the expansion.

In this chapter, we discuss the quintessence dynamics in the light of recent cosmological observations. We consider different quintessence scenarios and we determine constraints on the cosmological parameters such as the equation of state parameter, non-relativistic matter density parameter etc., employing different cosmological observational datasets mentioned in chapter 1.6.3. This chapter is based on "**Observational constraints on quintessence models of dark energy [arXiv:1804.09350]**" [68].

Parameter	Lower Limit	Upper Limit
Ω_m	0.01	0.6
w_0	-1.0	1.0
α	0.01	1.0
ϕ	0.1	10.0

Table 3.1: This table lists the priors used for parameter fitting in case of $V(\psi) = M^4 e^{-\alpha^{1/2}\psi/M_p}$ and $V(\psi) = M^{4-n}\psi^n$ potential. Here, the parameters Ω_m, w_0 and ϕ represent the present value of non-relativistic energy density parameter, equation of state parameter of dark energy and present value of field ψ.

3.1 Quintessence Dynamics

We consider a scalar field ψ minimally coupled, i.e. experiencing only gravity, passively through the space-time curvature and a self-interaction described by the scalar field potential V(ψ) and with a canonical kinetic energy contribution. The action for a quintessence field is therefore given by

$$S = \int d^4x\sqrt{-g}\left(-\tfrac{1}{2}g^{\nu\mu}\partial_\nu\psi\partial_\mu\psi - V(\psi)\right) \tag{3.1}$$

In a flat Friedmann background, the pressure and energy density of a homogeneous scalar field are given by

$$\begin{aligned} P &= \frac{\dot{\psi}^2}{2} - V(\psi) \\ \rho &= \frac{\dot{\psi}^2}{2} + V(\psi). \end{aligned} \tag{3.2}$$

The equation of state, which is in general is time varying, is defined as

$$w = \frac{P}{\rho}. \tag{3.3}$$

The equation of motion for the scalar field, the Klein-Gordon equation

$$\ddot{\psi} + 3H\dot{\psi} = -\frac{dV}{d\psi}, \tag{3.4}$$

follows from functional variation of the lagrangian and is interchangeable with the continuity equation.

For a universe which is spatially flat the friedmann equations for a canonical scalar

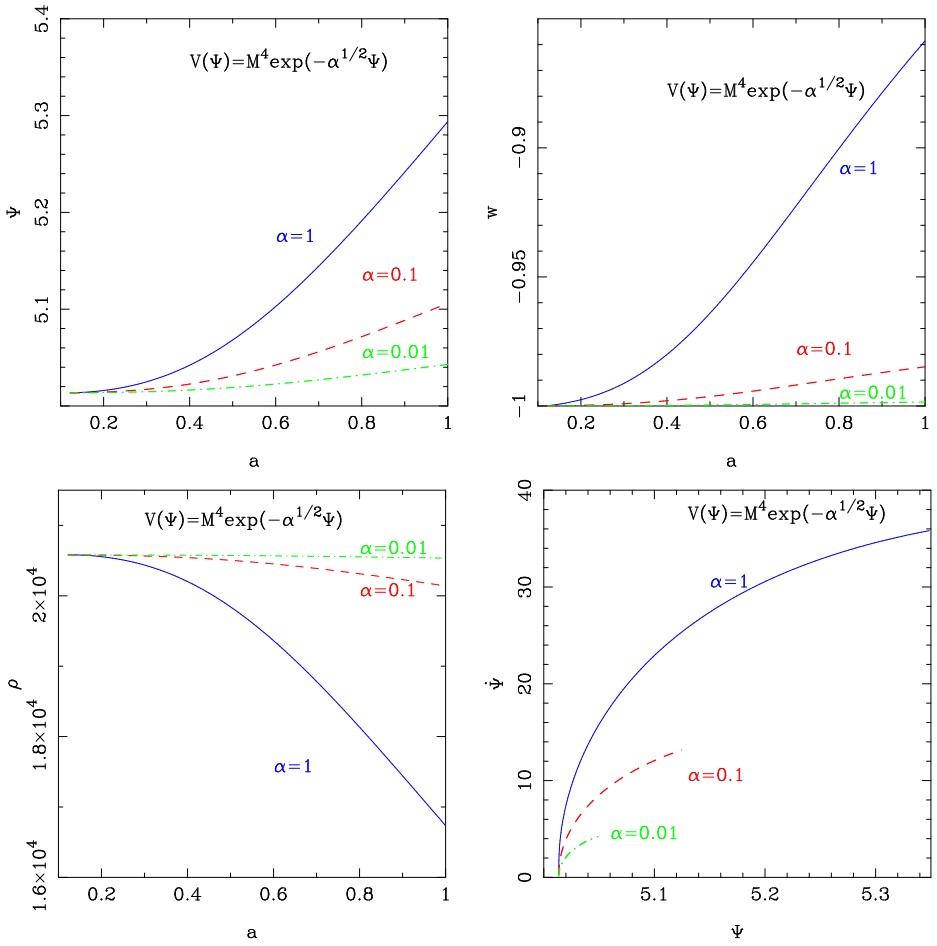

Figure 3.1: The plots in the figure represent evolution of different quantities for the potential $V(\psi) = M^4 e^{-\alpha^{1/2}\psi/M_p}$. Three different values of α considered are 0.01, 0.1 and 1. Here we have plotted $\Psi = \psi/M_p$. The left plot in the first row shows the variation of ψ as a function of scale factor for different values of α. The plot on the shows the behavior of equation of state parameter w for the field potential as the scale factor varies. In the second row, the plot on the left is for energy density of the field as a function of scale factor and the figure on the right is the phase plot for the exponential potential.

field can be written as

$$H^2 = \frac{8\pi G}{3}\left[\frac{1}{2}\dot{\psi}^2 + V(\psi)\right], \tag{3.5}$$

$$\frac{\ddot{a}}{a} = -\frac{8\pi G}{3}\left[\dot{\psi}^2 - V(\psi)\right]. \tag{3.6}$$

For an accelerating universe $\dot{\psi}^2 < V(\psi)$. This means that one requires an almost flat potential to give rise to an accelerated expansion. The equation of state for the field ψ is given by

$$w = \frac{\dot{\psi}^2 - 2V(\psi)}{\dot{\psi}^2 + 2V(\psi)}. \tag{3.7}$$

Data set	3σ confidence	χ^2_m	Best Fit Model
$V = M^4 e^{-\sqrt{\alpha}\Psi}$			
SNIa	-1.0 $\leq w_0 \leq$ -0.63 0.01 $\leq \Omega_m \leq$ 0.31 0.01 $\leq \alpha \leq$ 1.0	563.42	w_0=-0.97 Ω_m=0.24 α=0.03
BAO	-1.0 $\leq w_0 \leq$ -0.85 0.26 $\leq \Omega_m \leq$ 0.31 0.01 $\leq \Omega_m \leq$ 1.0	2.35	w_0=-0.99 Ω_m=0.28 α=0.07
H(z)	-1.0 $\leq w_0 \leq$ 0.14 0.19 $\leq \Omega_m \leq$ 0.32 0.01 $\leq \alpha \leq$ 1.0	17.04	w_0=-1.0 Ω_m=0.26 α=1.0

Table 3.2: The above table shows the 3σ confidence limit for all the three data sets and the value of parameters corresponding to the minimum value of χ^2 for the potential $V(\Psi) = M^4 e^{-\sqrt{\alpha}\Psi}$, where $\Psi = \psi/M_p$. For H(z) data, marginalized over H_0.

Using Eq. 3.7, we can calculate the equation of state for a given potential and then we study the effects on cosmological expansion.

Depending on the evolution of w, quintessence models are classified into two broad categories [69, 70, 71, 72, 73, 74, 75, 76, 77]. The first corresponds to thawing models, in which the field is nearly frozen by a Hubble damping during the early cosmological epoch and it starts to evolve once the field mass m_ψ drops below the Hubble rate $H(a)$. Here the field is displaced from its frozen value recently, when it starts to roll down to the minimum. In this case, the evolution of w is characterized by the growth from -1, at early times the equation of state is $w \approx$ -1, but grows less negative with time. We analyze the following concave potentials for thawing behavior [59, 78, 79, 80, 81].

- Exponential potential :

$$V = M^4 e^{-\sqrt{\alpha}\psi/M_p} \tag{3.8}$$

- Polynomial (concave) potential :

$$V = M^{4-n}\psi^n \tag{3.9}$$

for $0 < n < 3$. The different values of n correspond to potentials with different shapes.

The second class of potentials consists of a field which was already rolling towards minimum of its potential, prior to the onset of acceleration, but slows down because of the

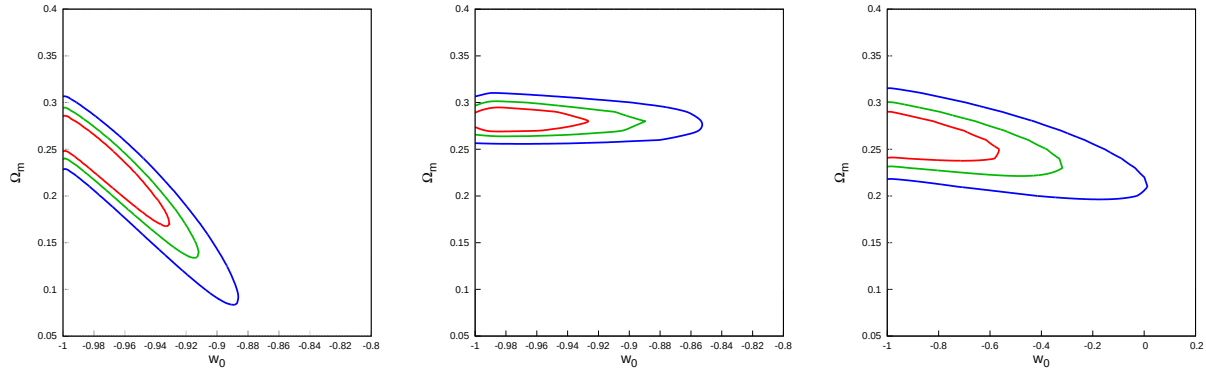

Figure 3.2: The figure represent 1σ, 2σ and 3σ confidence contours in $w_0 - \Omega_m$ plane for thawing potential $V = M^4 e^{-\sqrt{\alpha}\Psi}$. Going from left to right, the first, second and third plot is obtained for SNIa , BAO and H(z) data respectively. To obtain the contours we have marginalized over α.

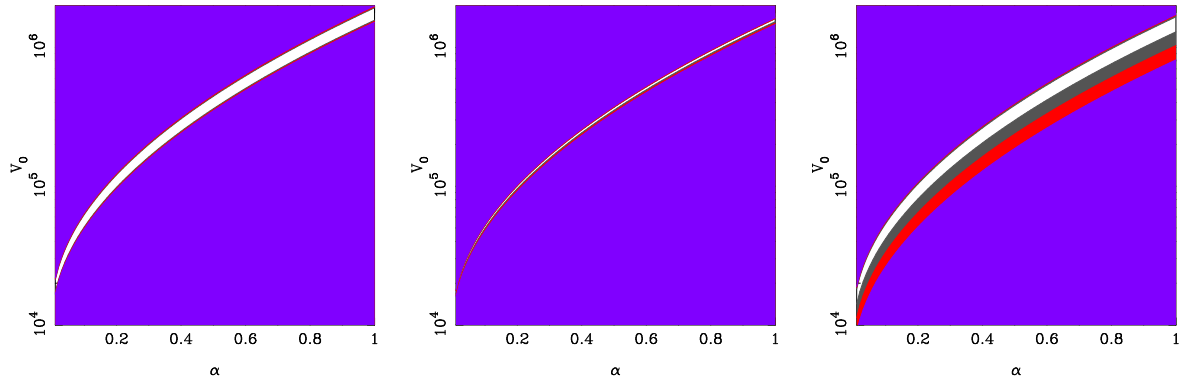

Figure 3.3: The figure represents allowed region for $V_0 = M^4/M_p^2$ corresponding to 1σ, 2σ and 3σ confidence region as a function of α for thawing potential $V = V_0 e^{-\sqrt{\alpha}\Psi}$. The left plot is obtained for SNIa , middle plot is obtained for BAO and right plot is the result from H(z) data respectively.

shallowness of the potential at late times and comes to a halt as it begins to dominate the universe. For freezing models, at late times, the equation of state parameter w approaches -1. For this work we focus on homogeneous scalar field scenarios belonging to thawing class.

3.2 Solutions to cosmological equation of motion

In this section, we discuss the background cosmology and numerical solutions for the different types of potentials that we have discussed in the previous section.

value of n	SNIa data	BAO data	H(z) data
$V(\phi) = M^{4-n}\psi^n$			
n=1	$\chi^2_{min} = 608.61$ $w_0 = -0.98$ $\Omega_m = 0.21$ $\phi = 1.7$	$\chi^2_{min} = 2.29$ $w_0 = -1.0$ $\Omega_m = 0.28$ $\phi = 10.0$	$\chi^2_{min} = 17.06$ $w_0 = -1.0$ $\Omega_m = 0.27$ $\phi = 3.1$
n=2	$\chi^2_{min} = 608.59$ $w_0 = -0.98$ $\Omega_m = 0.22$ $\phi = 6.2$	$\chi^2_{min} = 2.41$ $w_0 = -1.0$ $\Omega_m = 0.28$ $\phi = 10.0$	$\chi^2_{min} = 17.06$ $w_0 = -1.0$ $\Omega_m = 0.27$ $\phi = 5.8$
n=3	$\chi^2_{min} = 608.54$ $w_0 = -0.98$ $\Omega_m = 0.21$ $\phi = 5.5$	$\chi^2_{min} = 2.65$ $w_0 = -1.0$ $\Omega_m = 0.28$ $\phi = 10.0$	$\chi^2_{min} = 140.85$ $w_0 = -1.0$ $\Omega_m = 0.27$ $\phi = 8.4$

Table 3.3: The above table shows the value of the parameters corresponding to minimum value of χ^2 for the potential $V = M^{4-n}\psi^n$. Here, w_0, Ω_m and ϕ represent the presenet value of dark energy equation of state parameter, non-relativistic energy density parameter and the field ψ respectively.

Value of n	SNIa data	BAO data	H(z) data
1	-1.0$\leq w_0 \leq$-0.92 0.1$\leq \Omega_m \leq$0.29 1.0$\leq \phi \leq$10.0	-1.0$\leq w_0 \leq$-0.995 0.26$\leq \Omega_m \leq$0.31 1.0$\leq \phi \leq$ 10.0	-1.0$\leq w_0 \leq$0.1 0.19$\leq \Omega_m \leq$0.32 1.0$\leq \phi \leq$ 10.0
2	-1.0$\leq w_0 \leq$-0.91 0.1$\leq \Omega_m \leq$0.29 1.0$\leq \phi \leq$10.0	-1.0$\leq w_0 \leq$-0.996 0.26$\leq \Omega_m \leq$0.31 1.9$\leq \phi \leq$ 10.0	-1.0$\leq w_0 \leq$0.1 0.18$\leq \Omega_m \leq$0.32 1.0$\leq \phi \leq$ 10.0
3	-1.0$\leq w_0 \leq$-0.91 0.1$\leq \Omega_m \leq$0.29 1.0$\leq \phi \leq$10.0	-1.0$\leq w_0 \leq$-0.997 0.26$\leq \Omega_m \leq$0.31 2.8$\leq \phi \leq$ 10.0	-1.0$\leq w_0 \leq$0.08 0.18$\leq \Omega_m \leq$0.32 1.0$\leq \phi \leq$ 10.0

Table 3.4: The above table shows the 3σ confidence limit for all the three data for the potential $V = V_0\psi^n$ for n=1,2,3.

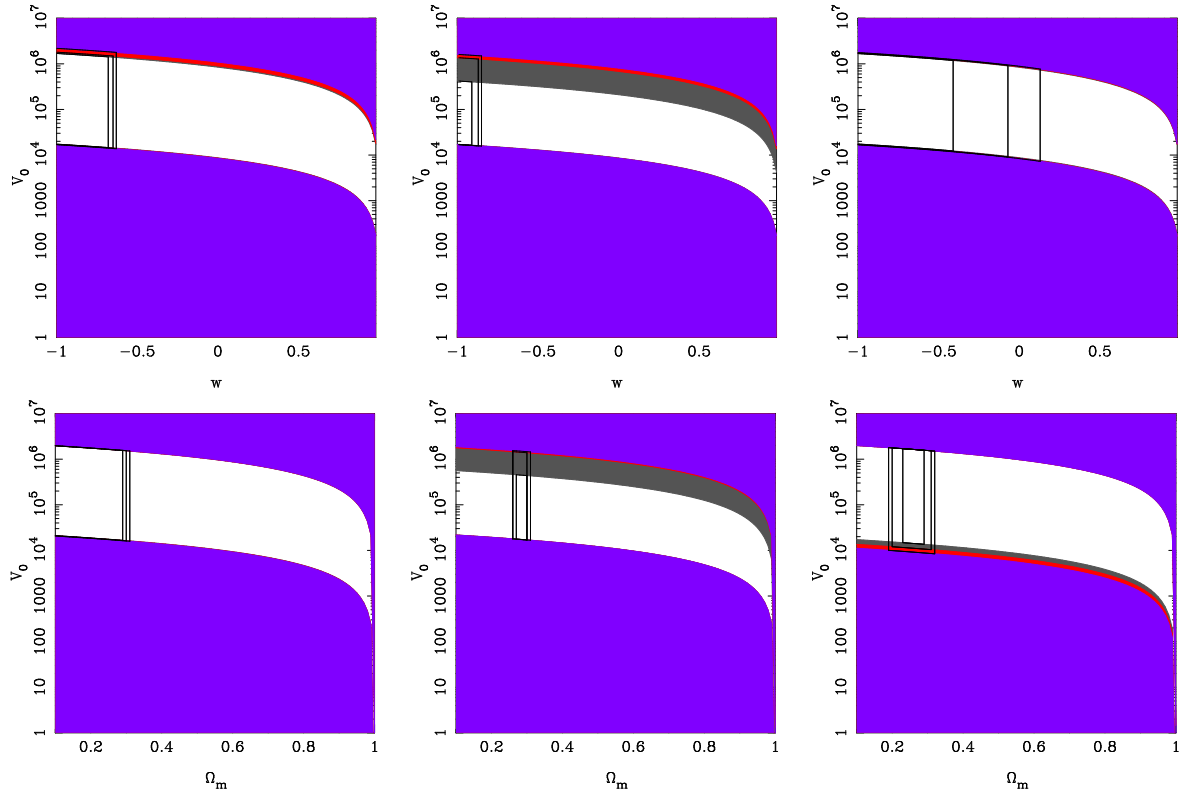

Figure 3.4: The figure represents allowed region for $V_0 = M^4/M_p^2$ corresponding to 1σ, 2σ and 3σ confidence region as a function of EoS w and Ω_m for potential $V = V_0 e^{-\sqrt{\alpha}\Psi}$ in first and second rows respectively. Going from left to right, the first, second and third plots are obtained for SNIa , BAO and H(z) datasets respectively. Numerically, V_0 is given by the formula in Eq.(3.13).

3.2.1 The exponential potential

To study how the universe evolves in the presence of this potential, we solve the Klein-Gordon equation, Eq. 3.4, and Friedmann equations for the scalar field, Eq. 3.5. In order to solve the equations, we define the following dimensionless parameter:

$$\Psi = \frac{\psi}{M_p}. \tag{3.10}$$

The potential, then, takes the form

$$V(\Psi) = M^4 e^{-\sqrt{\alpha}\Psi}. \tag{3.11}$$

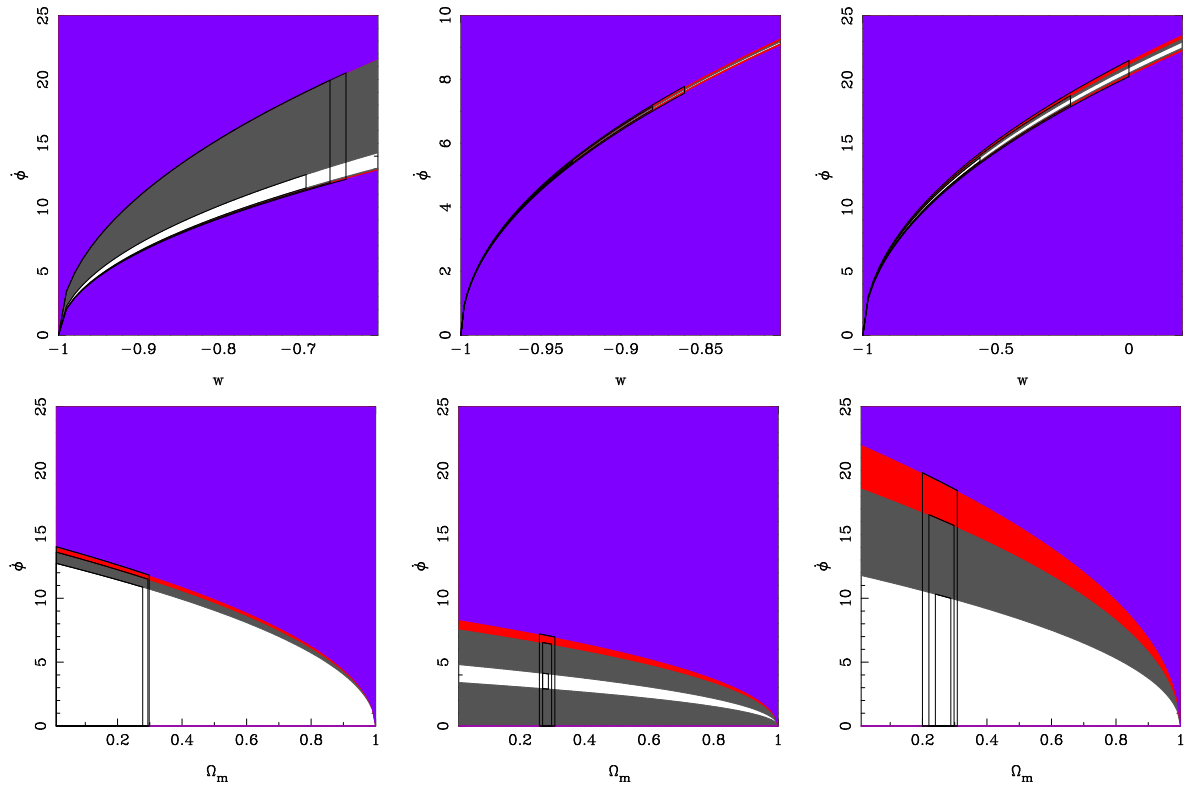

Figure 3.5: The figure represents allowed region for $\dot{\phi}$ corresponding to 1σ, 2σ and 3σ confidence region as a function of EoS w for potential $V = V_0 e^{-\sqrt{\alpha}\Psi}$ in first row and $\dot{\phi}$ as a function of Ω_m in second row. Here, $\dot{\phi}$ is the present value of $\dot{\psi}$. The scheme if plots is same as in Fig.(3.3). The field velocity, $\dot{\phi}$ is calculated using formula given in Eq.(3.14). The plots are for positive branch of field velocity.

In terms of the new variables, the cosmological equations can be written as

$$\ddot{\Psi} + 3\frac{\dot{a}}{a}\dot{\Psi} - \sqrt{\alpha}V_0 e^{-\sqrt{\alpha}\Psi} = 0, \tag{3.12}$$
$$\left(\frac{\dot{a}}{a}\right)^2 = H_0^2\frac{\Omega_m}{a^3} + \frac{\dot{\Psi}^2}{6} + \frac{V_0}{3}e^{-\sqrt{\alpha}\Psi}$$

where $V_0 = \frac{M^4}{M_p^2}$ and H_0 is the present value of Hubble parameter. For $\Omega_{total} = \Omega_m + \Omega_\phi = 1$, the initial conditions are given by

$$V_0 = \frac{3H_0^2}{2}(1-\Omega_{m_i})(1-w_{in})e^{\sqrt{\alpha}\Psi_i} \tag{3.13}$$

$$\dot{\Psi_i}^2 = 3H_0^2(1-\Omega_{m_i})(1+w_{in}); \qquad \Psi_i = 1. \tag{3.14}$$

The variables Ω_{m_i}, Ψ_i and w_{in} are values of non-relativistic matter density parameter,

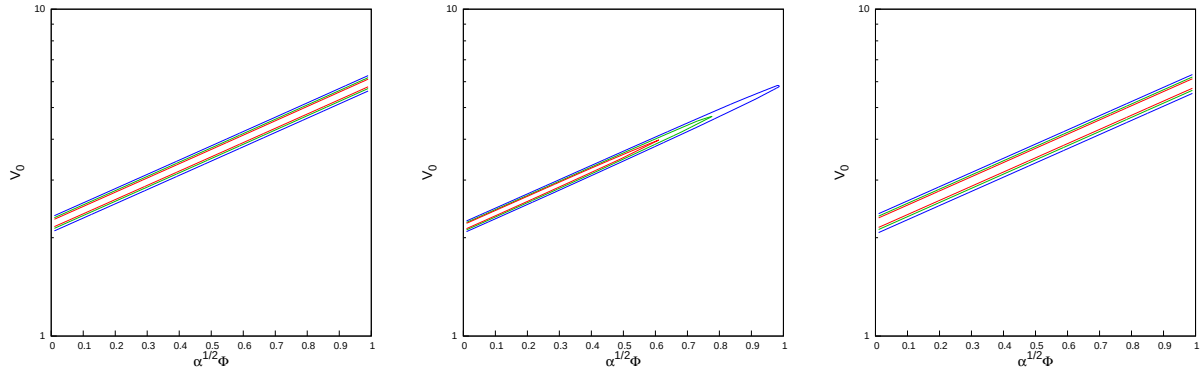

Figure 3.6: The figure represent 1σ, 2σ and 3σ confidence contours in $\sqrt{\alpha}\Phi - V_0$ plane for thawing potential $V = M^4 e^{-\sqrt{\alpha}\Psi}$. Going from left to right, the first, second and third plot is obtained for SNIa , BAO and H(z) data respectively. Here, V_0 is scaled by the square of the present value of Hubble parameter (H_0^2).

field and equation of state parameter at some initial time $t = t_i$. From here onwards, ϕ and Φ represents the present value of ψ and Ψ respectively.

By solving these coupled equations analytically, we get a solution for Ψ and $\dot{\Psi}$. These values are, then, used to determine the value of equation of state parameter w, which in terms of the dimensionless parameters is given by

$$w = \frac{\dot{\Psi}^2 - 2V_0 e^{-\sqrt{\alpha}\Psi}}{\dot{\Psi}^2 + 2V_0 e^{-\sqrt{\alpha}\Psi}}. \tag{3.15}$$

The above equation infers that, depending upon the form of potential $V(\Psi)$, w lies between -1 and $+1$.

To study the evolution of the model, we evolve the system from early time to late time. We plot the results obtained for this potential in Fig. 3.1. The plot on the left in the first row shows the variation of Ψ as a function of scale factor. The plot on the right shows the behavior of equation of state parameter w as scale factor changes. The larger value of parameter α corresponds to a steeper potential and the scalar field evolves faster. In the second row, the plot on the left is for energy density of the field as a function of scale factor and the figure at right is the phase plot obtained for the potential. Using different observations in the analysis, we constrain the cosmological parameters.

The priors used for the analysis are listed in Table 3.1. The results obtained are shown in figure Fig. 3.2. The plots in the figure represent 1σ, 2σ and 3σ confidence contours in $\Omega_m - w$ plane. The first, second and third plot is obtained for SNIa , BAO and H(z) data respectively. To obtain the contours we have marginalized over the entire range of

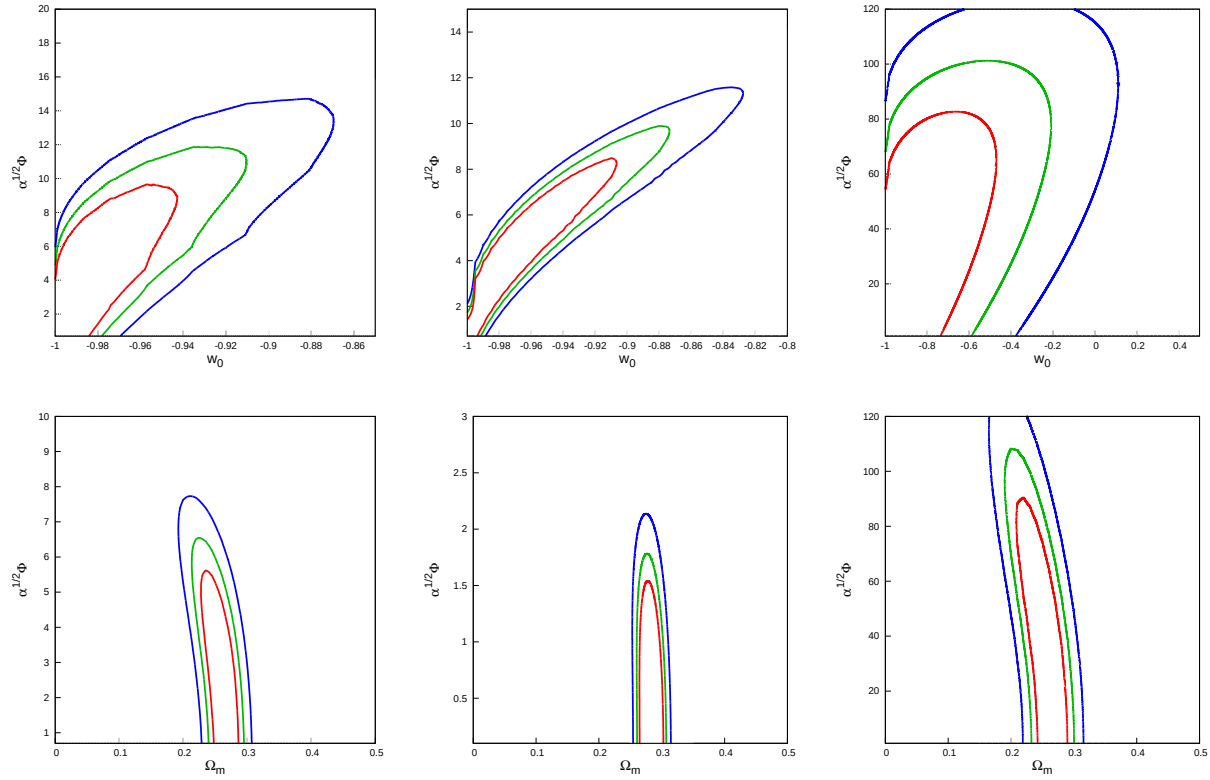

Figure 3.7: The figure represent 1σ, 2σ and 3σ confidence contours in $w - \sqrt{\alpha}\Phi$ plane for thawing potential $V = M^4 e^{-\sqrt{\alpha}\Psi}$ in first row and contours in plane $\Omega_m - \sqrt{\alpha}\Phi$ are given in second row.The scheme of the plots is same as in Fig. 3.2.

α. The minimum value of χ^2 (χ^2_{min}) is listed in Table 3.2 and the constraints obtained for the parameters are listed in Table 3.2.

3.2.2 The Polynomial (concave) potential

The second potential of thawing class that we analyzed is a power potential given by

$$V(\psi) = M^{4-n}\psi^n. \tag{3.16}$$

The background equations then take the following form:

$$\ddot{\psi} + 3\frac{\dot{a}}{a}\dot{\psi} + nV_0\psi^{n-1} = 0, \tag{3.17}$$
$$\left(\frac{\dot{a}}{a}\right)^2 = \frac{\Omega_m}{a^3} + \frac{\dot{\psi}^2}{6} + \frac{V_0\psi^n}{3}.$$

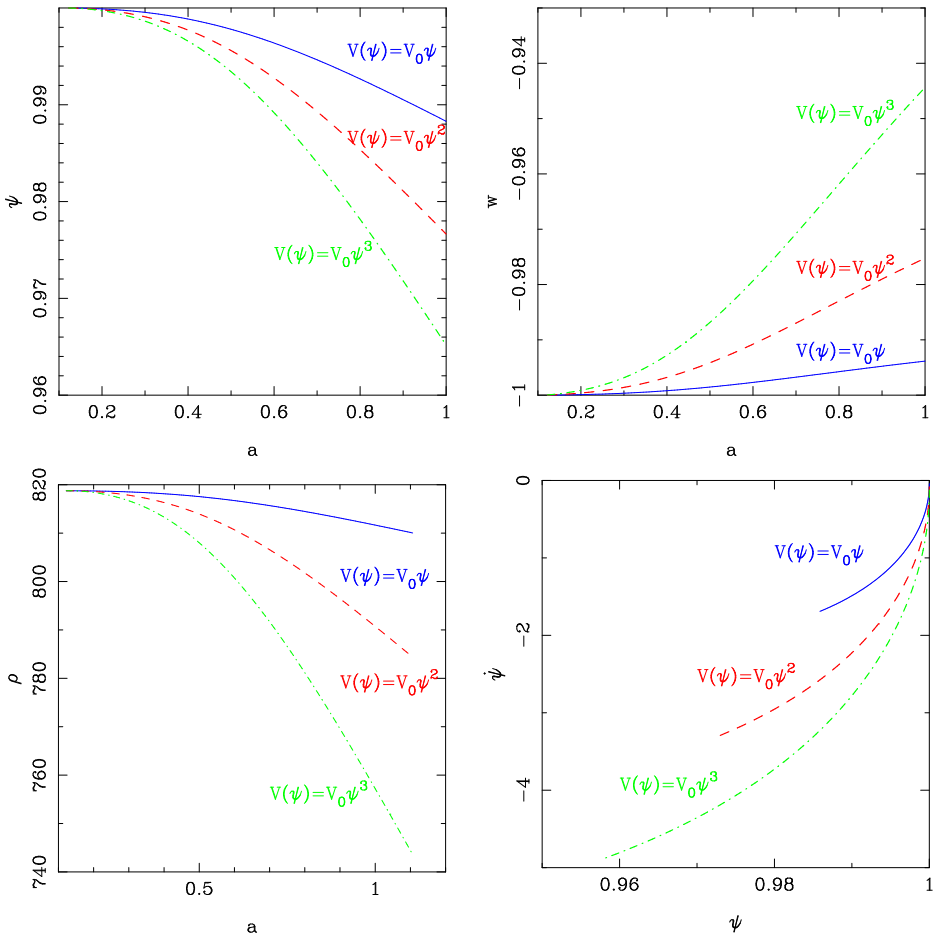

Figure 3.8: The plots in this figure represent the theoretical results obtained for potential $V(\psi) = M^{4-n}\psi^n$, for n =1, 2 and 3. In the first row of the left plot shows the variation of ψ as a function of scale factor. The right plot shows the evolution of equation of state parameter w for the potential as scale factor changes. In the second row, the plot on the left is for energy density of the field as a function of scale factor and the figure on the right is the phase plot for the power potential.

And equation of state becomes

$$w = \frac{\dot{\psi}^2 - 2V_0\psi^n}{\dot{\psi}^2 + 2V_0\psi^n}. \tag{3.18}$$

The value of V_0 for this potential is found to be

$$V_0 = \frac{3H_0^2}{16\pi G}(1 - \Omega_{m_i})(1 - w_{in})\psi_i^{-n} \tag{3.19}$$

and the initial value of field velocity, $\dot{\psi_i}$=$\dot{\phi}$ is given by

$$\dot{\phi} = \dot{\psi_i} = \pm\sqrt{\frac{3H_0^2}{8\pi G}(1-\Omega_{m_i})(1+w_{in})} \tag{3.20}$$

and the initial value of the field ψ_i is denoted by ϕ.

We plot the results obtained by evolving the system from past to present for this potential in Fig. 3.8. In the first row, the plot on the left shows the variation of ψ as a function of scale factor. The plot on the right shows the behavior of equation of state parameter w for the potential w.r.t. scale factor. At earlier times, w is almost -1 and behaves like a cosmological constant but at later times, w evolves away from -1. For a larger value of n, the field evolves faster. In the second row, the plot on the left is for energy density of the scalar field as a function of a and the figure on the right is the phase plot obtained for the polynomial potential.

3.3 Results

In this section, we discuss the results obtained by using the three different cosmological observations in the analysis.

First we will discuss the results obtained for the exponential potential, $V(\Psi) = M^4 e^{-\sqrt{\alpha}\psi/M_p}$. The priors used for the analysis are listed in Table 3.1. The free parameters used in the analysis are dark energy EoS parameter w, matter density parameter Ω_m and α. We have fixed the value of field $\phi = 1$.In Figure 3.2, we show the 1σ, 2σ and 3σ confidence contours in $\Omega_m - w_0$ plane. Here, Ω_m and w_0 denotes the present values of matter density parameter and equation of state parameter. The plot on the left is from the SNIa data, the plot in middle is for BAO data and the plot on right shows the results from H(z) data. To obtain the contours we have marginalized over the entire range of parameter α. The minimum value of χ^2 (χ^2_{min}) is listed in Table 3.2 and the constraints obtained for the parameters are listed in Table 3.2. BAO data provides the narrowest constraints on Ω_m and provides an upper limit on w_0; none of the data sets provide a lower limit on w_0. The Hubble data constrains Ω_m nicely, but it allows the regions of w_0 within 3σ limits, which gives decelerated expansion. Supernova data, too, does not provide a lower limit on parameter w_0; it allows entire range of w_0 below $w_0 \leq -0.88$.

We show the allowed range of $V_0 = M^4/M_p^2$ corresponding to 1σ, 2σ and 3σ confidence regions as a function of α in figure 3.3. The left plot is obtained for SNIa , middle plot is

obtained for BAO and right plot is the result from H(z) data respectively. The maximum range is allowed by H(z) data and the narrowest range is provided by BAO data. The results are consistent with the confidence contours of figure 3.2, this is because the value of V_0 depends upon both Ω_m and w. The parameter α alone is not constrained. In figure 3.4, we shows allowed range of V_0 as a function of dark energy equation of state parameter w (in first row) and V_0 as a function of Ω_m in second row. The allowed range in both the cases are large and comparable, but BAO allows smallest range as compared to others.

The allowed range of field velocity $\dot{\phi}$ as a function of w and Ω_m is shown in figure 3.5. The scheme of the plots is same as before. The variation of field velocity is calculated using the form of equation (3.14). From this equation, we get two branches for $\dot{\phi}$; first is $\dot{\phi} = \sqrt{3H_0^2(1+w_{in})}$, which we will refer to as the positive branch and another one is the negative branch which is given by $\dot{\phi} = -\sqrt{3H_0^2(1+w_{in})(1-\Omega_{m_i})}$. Here we have plotted for the positive branch, the results of negative branch are just opposite to the positive one. The allowed range for the positive branch lies above zero, in case of the negative it lies below zero. In this case too, the BAO provides the tightest allowed range as compared to the other two datasets.

Fig. 3.6 shows the confidence contours corresponding to 1σ, 2σ and 3σ levels in V_0 and $\sqrt{\alpha}\Phi$ plane. Here, we show the results for the range $0-1$ of $\sqrt{\alpha}\Phi$. We find that the most stringent constraints are provided for BAO data set, and the widest range is allowed for H(z) data and for SNIa data set the range lies between the range provided by other two datasets. In Fig. 3.7, we show the allowed range of $\sqrt{\alpha}\Phi$ and w for different datasets in first row and in second row we show the constraints on $\sqrt{\alpha}\Phi$ versus Ω_m. The first plot is obtained for SNIa, second plot is obtained for BAO and third plot is the result from H(z) data respectively. The results are consistent with the confidence contours of Fig. 3.2. This is because the value of V_0 depends upon both Ω_m and w.

We will now discuss the results obtained for the concave potential, $V = M^{4-n}\psi^n$. This potential gives us three potentials, as n takes three values; n=1,2 and 3. The free parameters in the analysis are w, non-relativistic matter density parameter Ω_m and field ϕ. The priors used for this analysis are listed in Table 3.1. The figure 3.9 shows the 1σ, 2σ and 3σ confidence contours in $\Omega_m - w$ plane. The contours in the first rows are obtained from analysis of SNIa data, second row represents plots from BAO data and the third row shows results for H(z) dataset. The contours in first, second and third columns are for $n = 1$, 2 and 3 respectively. The two dimensional contours in $w - \Omega_m$ plane are shown by marginalizing over the third parameter ϕ. The value of minimum χ^2

is listed in Table 3.3 and the constraints on the parameters are listed in Table 3.4. The tightest constraints are from the BAO data, followed by SNIa and H(z) data respectively. The H(z) data also allows models with a decelerated expansion for all three values of n, within the 3σ confidence limit. We find that for a dataset, the tightest range is given by the potential corresponding to $n = 3$; as the value of n decreases, the allowed range for w increases for all three datasets. As the value of n increases, the contours move towards $w = -1$, the cosmological constant model. All the three datasets provide strong constraints on Ω_m, with SNIa giving maximum allowed range for this parameter.

In figure 3.10, we show the allowed range of $V_0 = M^{4-n}$ corresponding to 1σ, 2σ and 3σ confidence regions as a function of field ϕ. The scheme of plots is same as in figure 3.9. As the value of ϕ increases, the allowed range of values of V_0 decreases. This trend is same for the three datasets for all values of n. The maximum value V_0 is required for a smaller value of ϕ. The maximum range is allowed by H(z) data and the narrowest range is provided by BAO data for all values of n. The results are consistent with the confidence contours in plane $w - \Omega_m$ of figure 3.9 as the value of V_0 depends upon those parameters (see Eq. (3.19)). Here, the entire range of ϕ considered in the analysis is allowed by the observations; there are no constraints on ϕ.

In figure 3.11, we show allowed range of V_0 as a function of dark energy equation of state parameter w corresponding to 1σ, 2σ and 3σ confidence contours. The allowed range for the three datasets are large, but BAO allows smallest range as compared to others, for all three values of n. In case of BAO data, as the value of n increases from 1 to 3, the maximum allowed range goes down from 500 to 110 to 11; this is not the case in other two datasets. In case of SNIa and H(z) datasets, the allowed ranges just increases, but the maximum value remains more or less the same, as we n increases. In figure 3.12, we shows allowed range of V_0 as a function of non-relativistic matter density parameter Ω_m corresponding to confidence contours in figure 3.9. Here, we see the similar pattern as in figure 3.11, as the value of Ω_m decreases the allowed range of V_0 increases. The minimum range is provided by BAO data set; as the value of n increases, the maximum of the allowed range decreases. For SNIa and H(z) data, as n increases, the maximum of the allowed range remains the same but the allowed ranges increases.

The allowed range of positive branch of $\dot{\phi}$ as a function of w corresponding to 1σ, 2σ and 3σ confidence level are presented in figure 3.13. The scheme of the plots is same as before. As the value of w increases, there is a monotonic increases in the allowed range of $\dot{\phi}$. For a particular data set, the variation in $\dot{\phi}$ is same for all values of n as the value of $\dot{\phi}$ is independent of n or the form of potential, see equation (3.20). The narrowest range

for $\dot{\phi}$ is given by BAO data followed by SNIa data and then H(z) data. The results of the negative branch is just the mirror image of those of positive branch along the $w = -1$ line.

In figure 3.14, we show the allowed range of positive branch of $\dot{\phi}$ as a function of Ω_m corresponding to 1σ, 2σ and 3σ confidence level. We see that as the value of Ω_m increases, the allowed range of $\dot{\phi}$ decreases. The tightest range is provided by BAO, then SNIa followed by H(z) data set. Also, for a dataset, if n increases, the allowed range of $\dot{\phi}$ increases. The results are similar for negative branch, the only difference being that the range lies below zero line and is a mirror image of the range for the positive branch.

In this chapter, constraints on thawing models of scalar field models of dark energy are presented for exponential potential ans the polynomial potentials. The datasets allow for a small range in variation of scalar field parameters. The models which closely emulate the background evolution of a cosmological constant are preferred by the observations. The constraints on different parameters are stringent since the different observations considered are sensitive to different physical quantities. The stringent constraints are provided by BAO data, which are consistent with fluid models of dark energy.

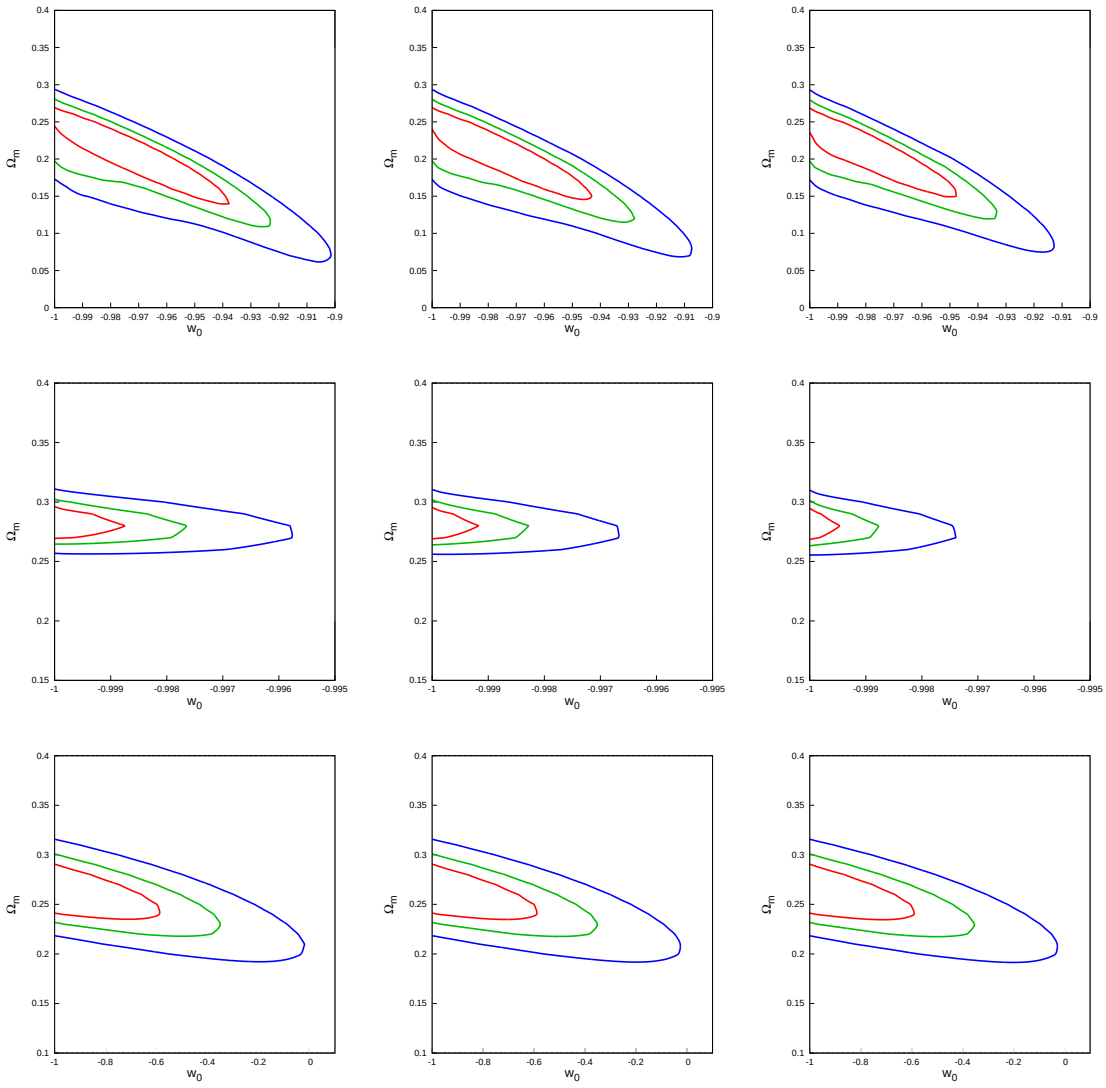

Figure 3.9: The plots in the rows of the figure represent 1σ, 2σ and 3σ confidence contours in $\Omega_m - w$ plane for $V = V_0\psi^n$. In first row, the first, second and third plot is obtained for SNIa for n equal to 1, 2 and 3 respectively. In the second row, the plots are obtained for BAO data for n equal to 1, 2 and 3 in the same order. The second row shows the plots for H(z) data for n equal to 1, 2 and 3 respectively.

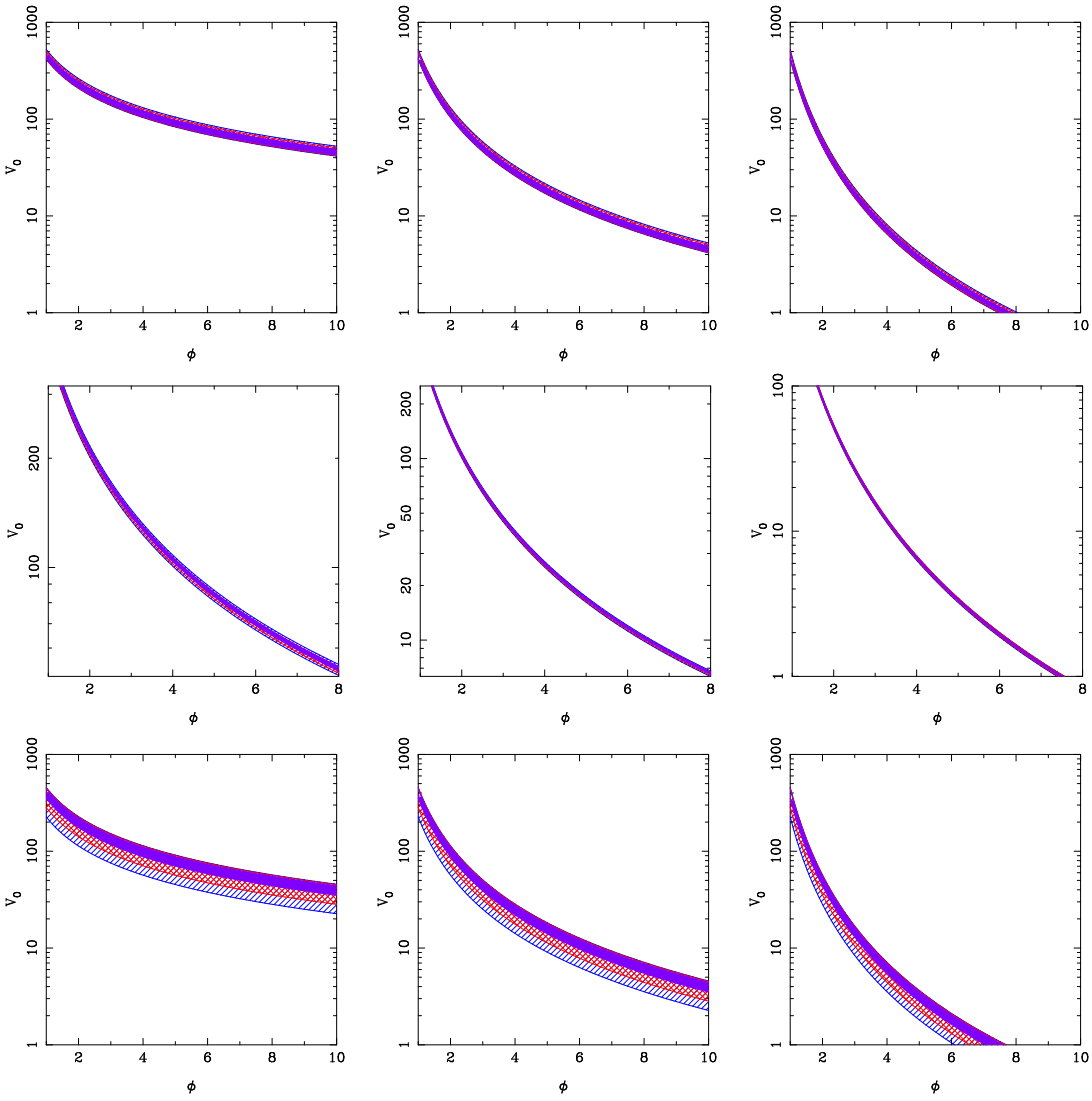

Figure 3.10: The plots in the rows of the figure represent allowed region for $V_0 = M^{4-n}$ corresponding to 1σ, 2σ and 3σ confidence region as a function of field ϕ, for $V = V_0\psi^n$. Going from left to right, the first, second and third plots are obtained for potentials corresponding to n equal to 1, 2 and 3 respectively. In first row, the plots shows results for SNIa, the plots in second row are obtained for BAO data and the third row shows the plots for H(z) dataset.

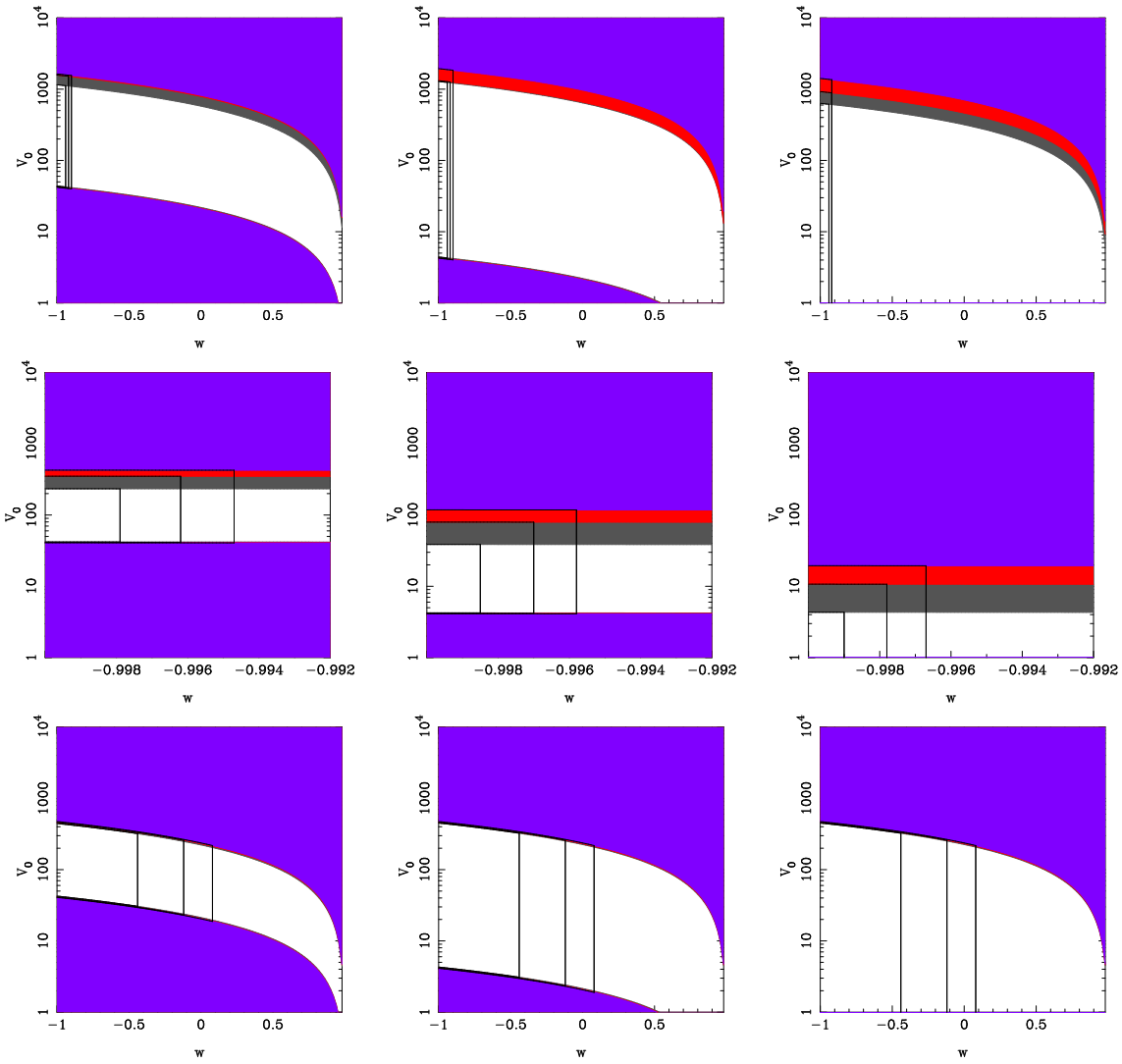

Figure 3.11: The plots in the rows of the figure represent allowed region for $V_0 = M^{4-n}$ corresponding to 1σ, 2σ and 3σ confidence region as a function of w, equation of state for the quintessence field, for $V = V_0\psi^n$. The scheme of the plots is same as before. The value of V_0 is calculated by using the formula given in Eq.(3.19).

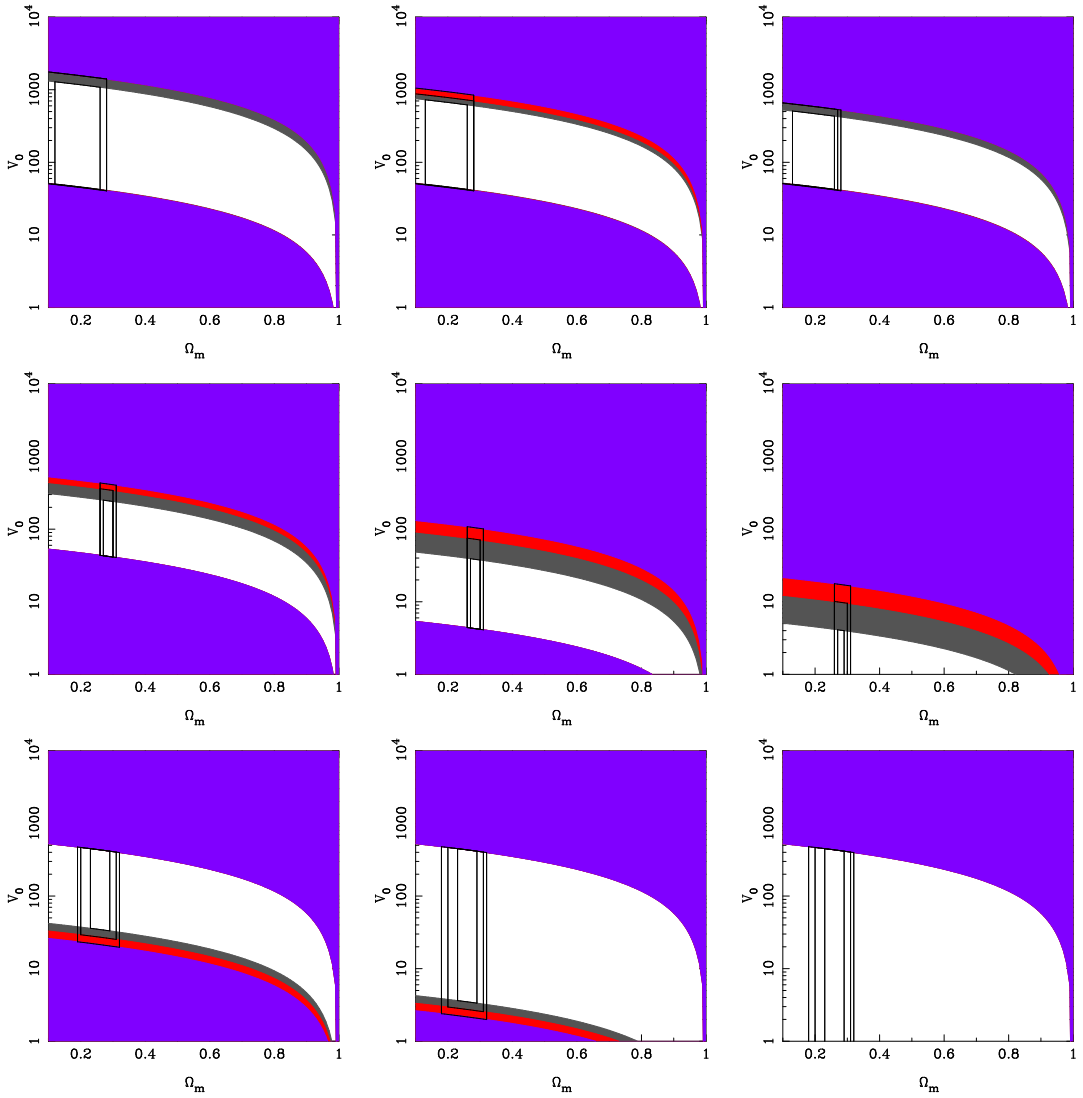

Figure 3.12: The plots in the rows of the figure represent allowed region for V_0 as a function of non-relativistic matter density parameter Ω_m, for thawing power potential $V = V_0\psi^n$. The order in which the plots are presented is same as in Fig.(3.10).

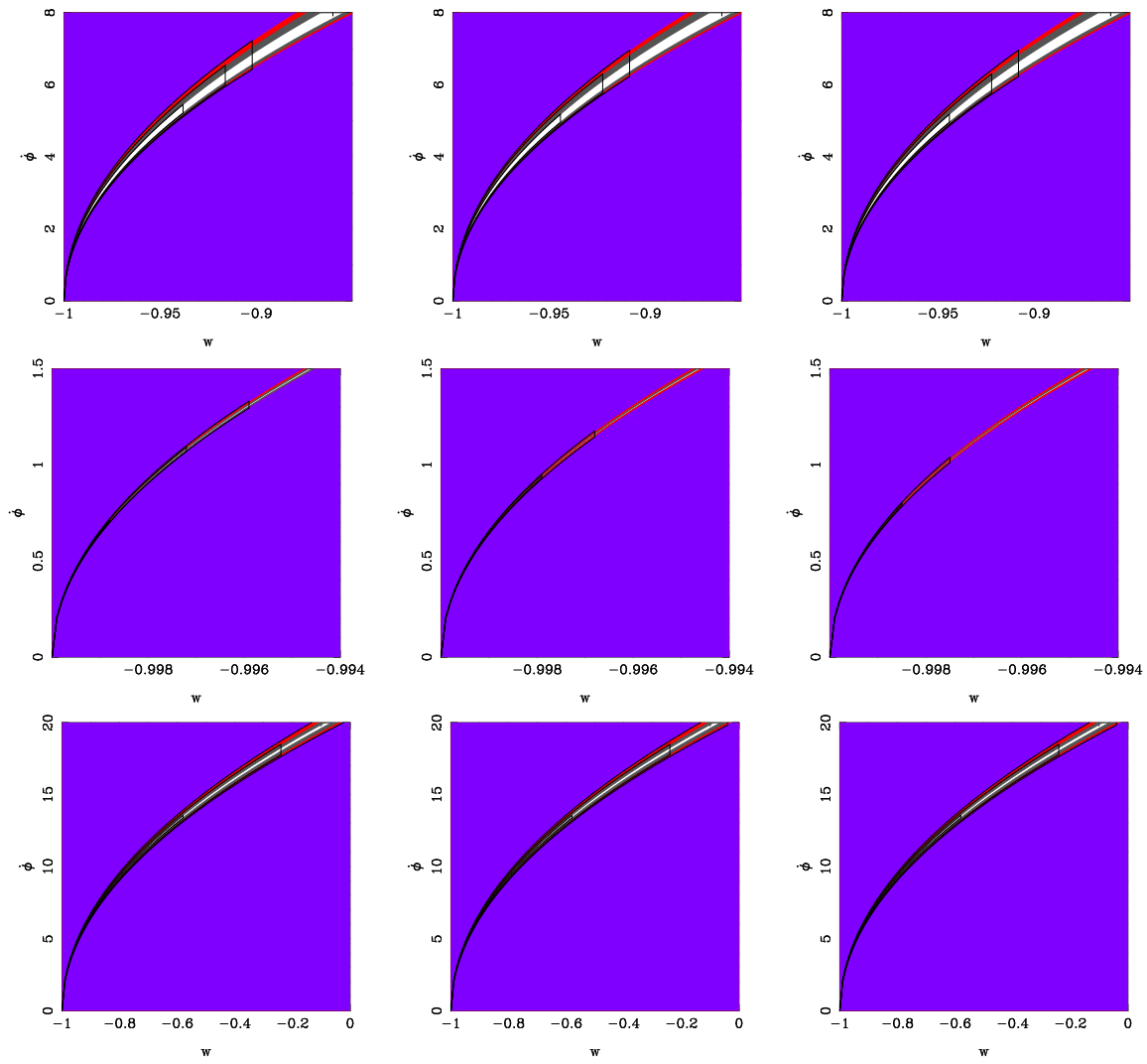

Figure 3.13: The plots in the rows of the figure represent allowed region for $\dot{\phi}$ corresponding to 1σ, 2σ and 3σ confidence region as a function of w, equation of state for the quintessence field, for $V = V_0\psi^n$. The scheme of the plots is same as before. The value of V_0 is calculated by using the formula given in Eq.(3.20).

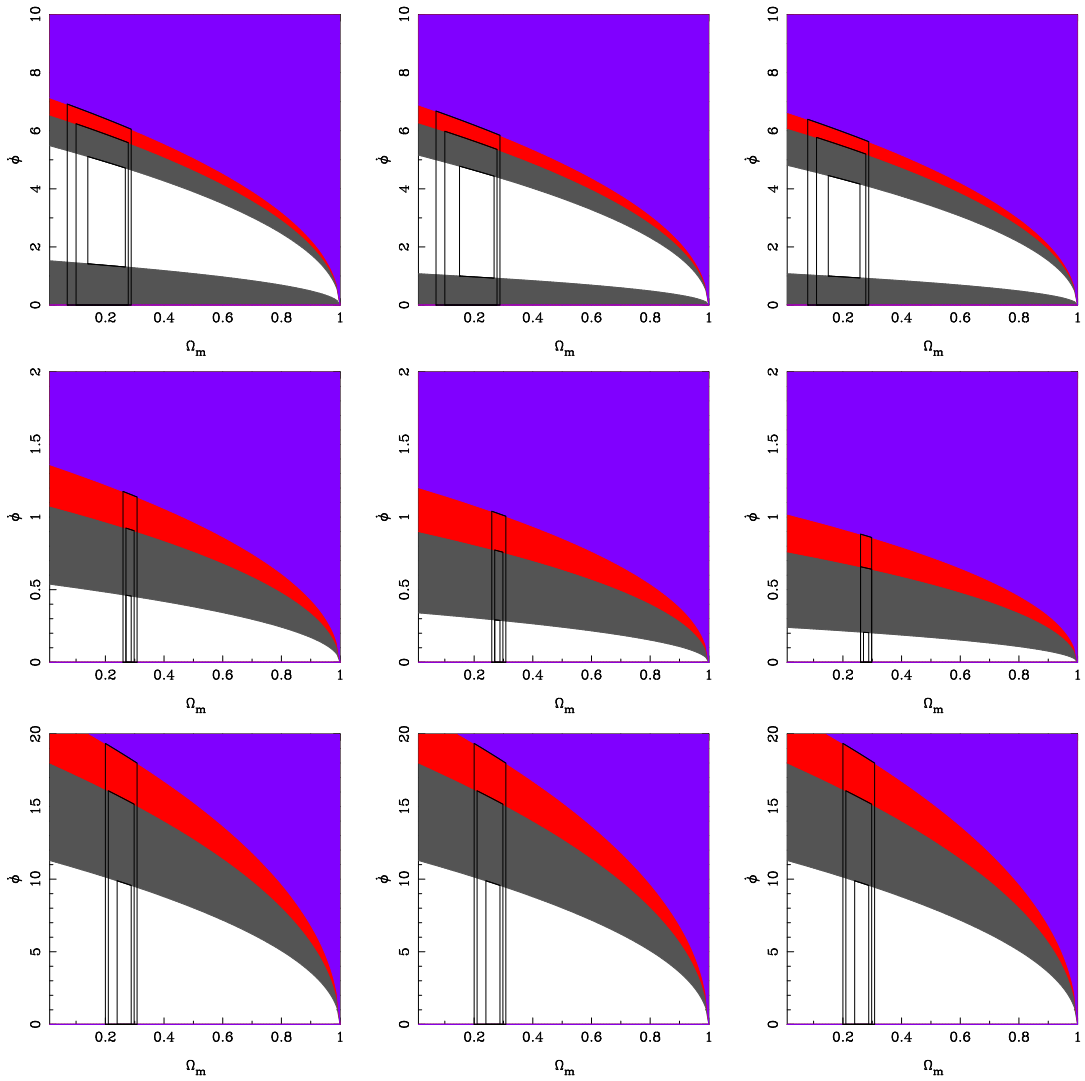

Figure 3.14: The plots in the rows of the figure represent allowed region for $\dot{\phi}$ corresponding to 1σ, 2σ and 3σ confidence region as a function of Ω_m, for the quintessence potential, $V = V_0\psi^n$. The scheme of the plots is same as before.

Chapter 4

Reconstruction of Dark Energy Potential

In this chapter, we reconstruct the quintessence and phantom scalar field potentials and study the evolution of the scalar field as a function of scale factor. We reconstruct the form of potentials that are consistent with the different parameterizations of dark energy equation of state mentioned in chapter 2 and by using cosmological observations, we constrain the reconstructed potential and the field parameters. This chapter is based on **A. Sangwan, A. Mukherjee, and H. K. Jassal *JCAP*, 1801(01):018, 2018**[65].

There are two methods of reconstruction. First is the parametric reconstruction method which we adopted. In this method a form of dark energy equation of state parameter is considered and using the cosmological equations we reconstruct the quantities. In the second method, instead of assuming a function form of dark energy equation of state, we reconstruct it from cosmological observations. For more details see [82]. Now we will discuss how the reconstruction of canonical and non-canonical potential is done.

4.1 Dark energy cosmology

For a spatially flat, homogeneous and isotropic universe, the cosmological evolution is described by the Friedmann equations 2.3. The Friedmann equation in terms of scale factor is given by

$$\frac{\dot{a}^2}{a^2} = \frac{8\pi G}{3}\rho, \tag{4.1}$$

$$2\frac{\ddot{a}}{a} + \frac{\dot{a}^2}{a^2} = -8\pi G p, \tag{4.2}$$

where a is the scale factor, ρ is the total energy density and p is the pressure. The total energy density ρ at a given time is the sum of the energy densities of single components. We neglected the contribution of the relativistic particles at late times because observations suggest that the energy of the present universe is dominated by dark energy with more than two-third, where less than one-third contribution is due to the energy density from non-relativistic matter.

The equation of state for a barotropic fluid is given by $p = w\rho$, where w is the equation of state parameter. The energy density is, in general, a function of the scale factor and is given by equation 2.7. For non-relativistic matter with $w = 0$, energy density is $\rho_m \propto a^{-3}$ and for relativistic particles with $w = 1/3$, energy density scales as $\rho \propto a^{-4}$. For dark energy, with a constant w, the dark energy density evolves as a function of scale factor as $a^{-3(1+w)}$. This is referred to as wCDM model.

In general, w can be a function of time and its behaviour can be approximated by way of assuming a functional form for its evolution. A simple parameterization is an expansion of the energy equation state in a Taylor series suggested by [15, 16]

$$w(a) = w_0 + w'(1 - a). \tag{4.3}$$

In this parameterization, namely the CPL parameterization, w_0 is the present value of equation of state parameter and w' is its first derivative. This is called the CPL parameterization. This functional form is used in most studies of varying dark energy models. This parameterization allows a slow variation of the dark energy density at late times. The asymptotic or early time value of the dark energy equation of state is $w_0 + w'$ and the present day value (i.e. at $a = 1$) is w_0. In this case, the variation of the dark energy density as a function of scale factor is given by

$$\frac{\rho_{DE}}{\rho_{DE_0}} = a^{-3(1+w_0+w')} \exp\left[-3w'(1 - a)\right]. \tag{4.4}$$

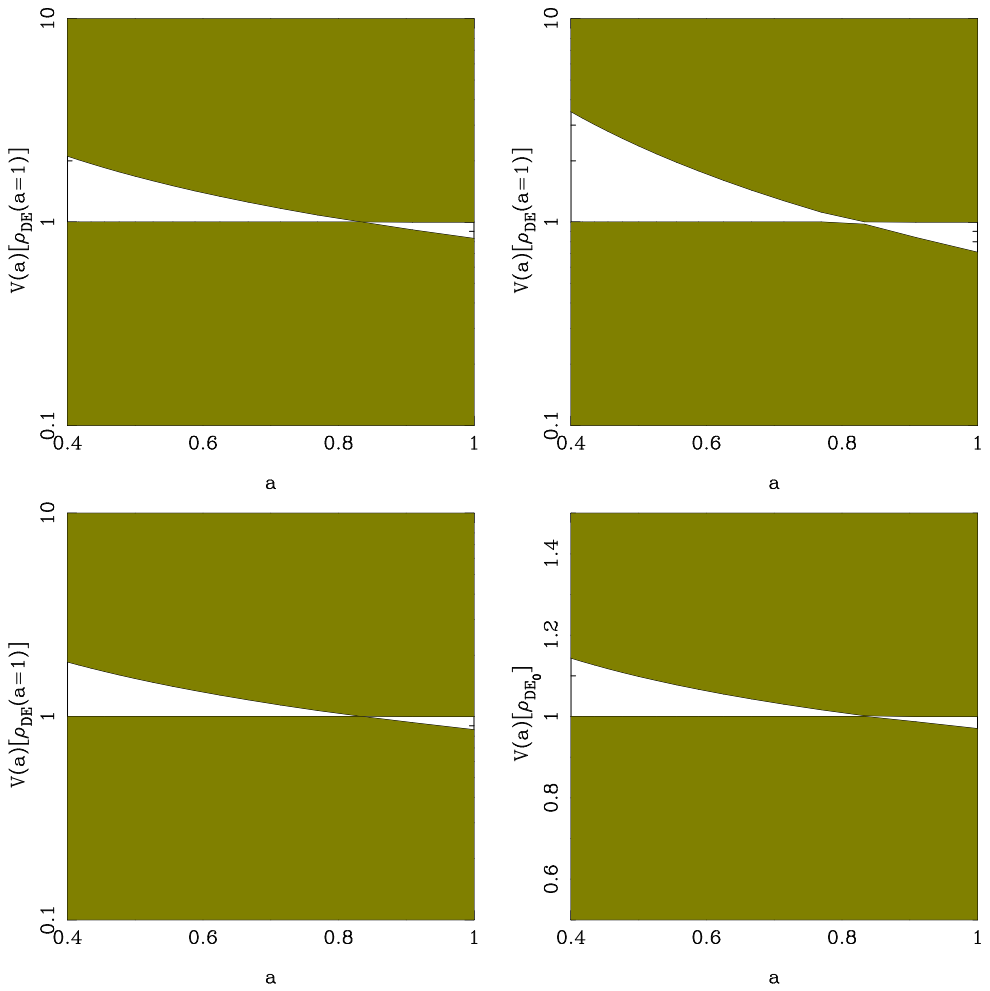

Figure 4.1: The figure represents 3σ allowed regions for the reconstructed potential, scaled by the present day dark energy density $[\rho_{DE}(a=1)]$ as a function of scale factor for the wCDM model. The first and second plots in the first row are the results obtained from the analysis of SNIa, BAO and the plots in second row are results obtained from H(z) and combined datasets respectively. The plots in first row are for a quintessence scalar field potential.

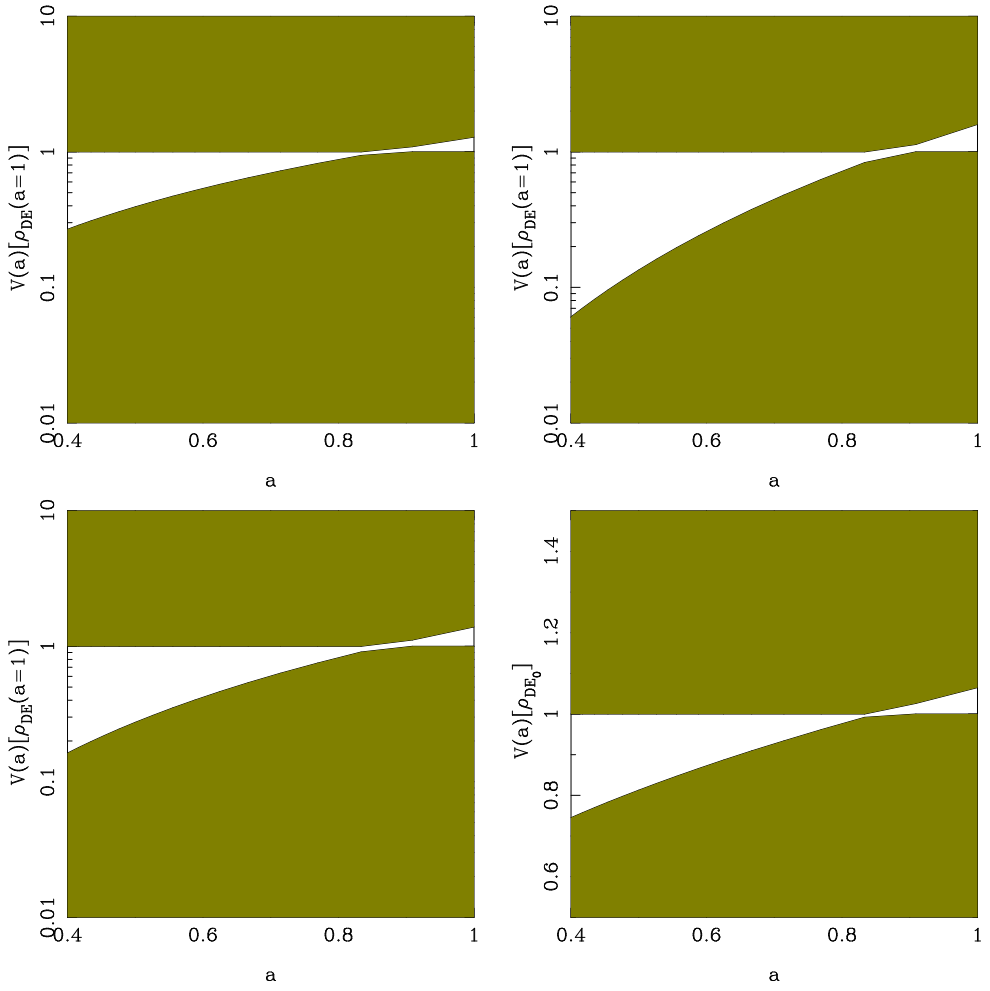

Figure 4.2: The figure represents 3σ allowed regions for the reconstructed phantom potential as a function of scale factor for the wCDM model. The potential is scaled by the present day dark energy density $[\rho_{DE}(a = 1)]$. The order in which the plots are presented is the same as in 4.1. The plots are for a phantom potential.

Another description of a varying equation of state parameter that is used in this work, is the logarithmic parameterization given as,

$$w(a) = w_0 - w' log(a). \tag{4.5}$$

In this case, the equation of state increases monotonically [18] and the variation of energy density with scale factor is given by

$$\frac{\rho_{DE}}{\rho_{DE_0}} = a^{-3(1+w_0-\frac{w'}{2}log(a))}. \tag{4.6}$$

We attempt for find explicit form of the scalar field potential which has the same background evolution as described by these parameterizations. Since all scalar field models of dark energy are largely phenomenological, it is reasonable to fit functional forms of scalar fields with the fluid parameterizations.

In the present work, the nature and evolution of the scalar field dark energy potentials are reconstructed for the evolution history allowed by these three parameterizations.

4.2 Reconstruction of scalar field potential

Dark energy is equivalently described by scalar fields, both canonical and non canonical. In this paper, we consider the canonical, quintessence field and the phantom field. For models which are of 'quintessence' type scalar fields [23, 60, 61, 62, 71, 83, 84, 85, 86, 87, 88, 89], $w > -1$ and on the other hand, $w < -1$ for 'phantom' like models. [83, 29, 90, 91, 92, 93, 94, 95]. The phantom scalar fields have a negative kinetic energy and are the same as the c-fields proposed by Hoyle and Narlikar [96, 97]. These c-fields are massless scalar fields and generate negative gravitational field because of negative energy density.

The pressure and energy density for quintessence and phantom scalar field are given by

$$p = \frac{\pm\dot{\phi}^2}{2} - V(\phi) \qquad \rho_{DE} = \frac{\pm\dot{\phi}^2}{2} + V(\phi), \tag{4.7}$$

where ϕ denotes the scalar field and $V(\phi)$ is the scalar field potential. In the above expressions, the plus sign corresponds to a quintessence field and the negative sign corresponds to a phantom field dark energy i.e., for a negative kinetic energy term. Therefore, the scalar field potential which is emulated by the parameterization given in equation 4.3

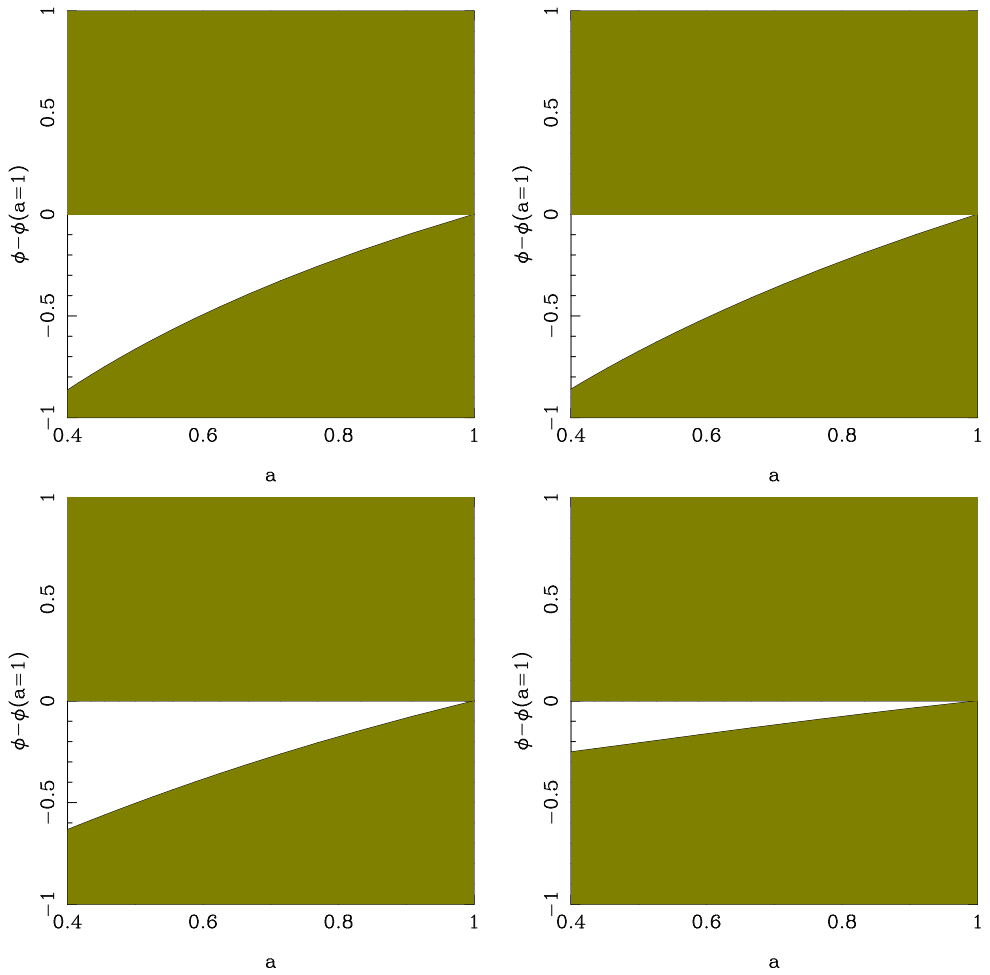

Figure 4.3: The plots show 3σ allowed regions for field ϕ as a function of scale factor reconstructed from the wCDM model. The plots in first row are plotted from the analysis of SNIa and BAO data. And the plots in second row shows the results obtained from H(z) data and combined datasets respectively. The plots are obtained for quintessence potential.

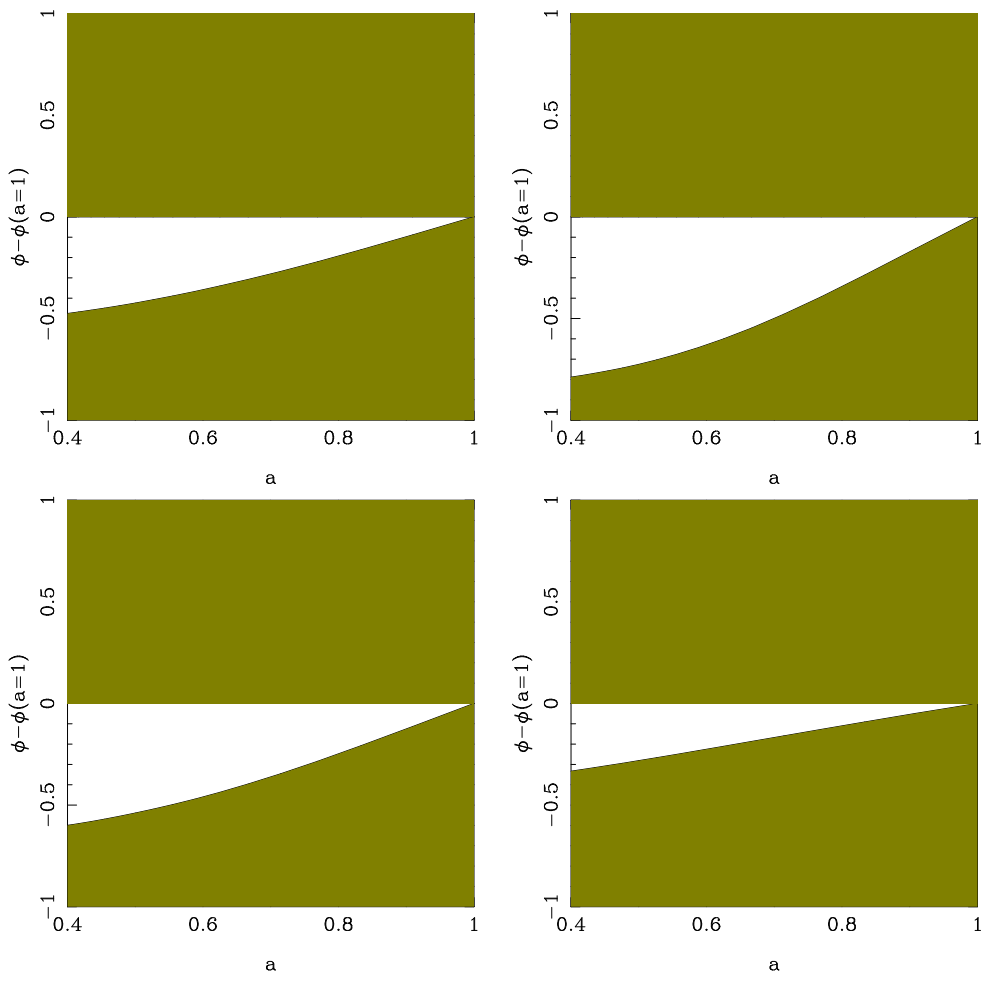

Figure 4.4: The plots show 3σ allowed regions for field ϕ as a function of scale factor reconstructed from the wCDM model for phantom scaler field. The order in which the plots are presented is the same as in 4.3.

can be reconstructed as

$$V(a) = \frac{1}{2}(1-w)\rho_{DE}(a).$$

for the scalar field. Here, w can be a constant or a function of the scale factor. The variation of the scalar field with time for a quintessence field is given as

$$\left[\frac{d\phi}{dt}\right]^2 = (1+w)\,\rho_{DE}$$

which, in turn, can be written as

$$\left[\frac{d\phi}{da}\right] = \frac{\sqrt{(1+w)\rho_{DE}}}{a\ H(a)}. \tag{4.8}$$

We mainly consider the positive sign in the above expression for our discussion. For completeness, we discuss the results for the negative sign branch within the quintessence scenario for the case of a constant equation of state parameter. The effective dynamics are the same for both the negative and positive branch as the energy density depends on $\dot{\phi}^2$.

For a phantom like scalar field, since the kinetic energy is negative, the variation in the field ϕ as a function of time is given as

$$\left[\frac{d\phi}{dt}\right]^2 = -\,(1+w)\,\rho_{DE},$$

which, in terms of the scale factor, is given by,

$$\left[\frac{d\phi}{da}\right] = \frac{\sqrt{-(1+w)\rho_{DE}}}{a\ H(a)}. \tag{4.9}$$

For a universe with dark energy as its sole constituent, the scalar field potential for a constant dark energy equation of state is given by (see also [98])

$$V(\phi) = \frac{1}{2}(1-w)\rho_{DE_0} exp\left[-\sqrt{24\pi G(1+w)}(\phi-\phi_0)\right],$$

which can be rewritten as

$$\tilde{V}(\tilde{\phi}) = \frac{1}{2}(1-w) exp\left[-\sqrt{3(1+w)}(\tilde{\phi}-\tilde{\phi}_0)\right] \tag{4.10}$$

where $\tilde{V} = V/\rho_{DE_0}$, $\tilde{\phi} = \sqrt{8\pi G}\phi$ and ϕ_0 is the value of field at $a = 1$. And for a phantom

dark energy, the potential is of the form

$$V(\phi) = \frac{1}{2}(1-w)\rho_{DE_0} exp\left[\sqrt{-24\pi G(1+w)}(\phi-\phi_0)\right].$$

We scale the potential with the present day value of dark energy density and ϕ by $\sqrt{8\pi G}$ and then the above equation takes the form

$$\tilde{V}(\tilde{\phi}) = \frac{1}{2}(1-w) exp\left[\sqrt{-3(1+w)}(\tilde{\phi}-\tilde{\phi}_0)\right]. \tag{4.11}$$

The slope of the potential and its amplitude are determined by the equation of state parameter of dark energy. The exponential potential belongs to the 'thawing' class of scalar fields, where the early times scalar field equation of state is like that of a cosmological constant with $w = -1$ and at late times begins to deviate from this value. This potential has been employed extensively for dark energy studies and as an inflation potential [99].

If the contribution of matter density is significant, the solutions for the quintessence scalar field for $w = constant$ are given by

$$(\tilde{\phi}-\tilde{\phi}_0) = \frac{\sqrt{3(1+w)}}{3w}\left[\ln\left(\frac{\sqrt{1+r_0a^{3w}}-1}{\sqrt{1+r_0a^{3w}}+1}\right) - \ln\left(\frac{\sqrt{1+r_0}-1}{\sqrt{1+r_0}+1}\right)\right], \tag{4.12}$$

where $r_0 = \rho_{m_0}/\rho_{DE_0}$. If $d\phi/da$ is negative, the expression for field is same as this with an overall negative sign and the expression of the quintessence scalar field potential can be written as,

$$\tilde{V}(\tilde{\phi}) = \frac{(1-w)}{2}\left[r_0 \sinh^2\left(\frac{\sqrt{3}w\tilde{\phi}}{2\sqrt{1+w}}\right)\right]^{\frac{1+w}{w}}. \tag{4.13}$$

Similarly, we obtain an expression for phantom scalar field, which is given by

$$(\tilde{\phi}-\tilde{\phi}_0) = \frac{\sqrt{-3(1+w)}}{3w}\left[\ln\left(\frac{\sqrt{1+r_0a^{3w}}-1}{\sqrt{1+r_0a^{3w}}+1}\right) - \ln\left(\frac{\sqrt{1+r_0}-1}{\sqrt{1+r_0}+1}\right)\right]. \tag{4.14}$$

The functional form of the potential for the phantom field is same as that for a quintessence potential except for a negative sign in the argument $\sqrt{-(1+w)}$, and is given as

$$\tilde{V}(\tilde{\phi}) = \frac{(1-w)}{2}\left[r_0 \sinh^2\left(\frac{\sqrt{3}w\tilde{\phi}}{2\sqrt{-(1+w)}}\right)\right]^{\frac{1+w}{w}}. \tag{4.15}$$

Here, the scalar field ϕ is scaled by $\sqrt{8\pi G} = M_{pl}^{-1}$. For a large value of the scalar

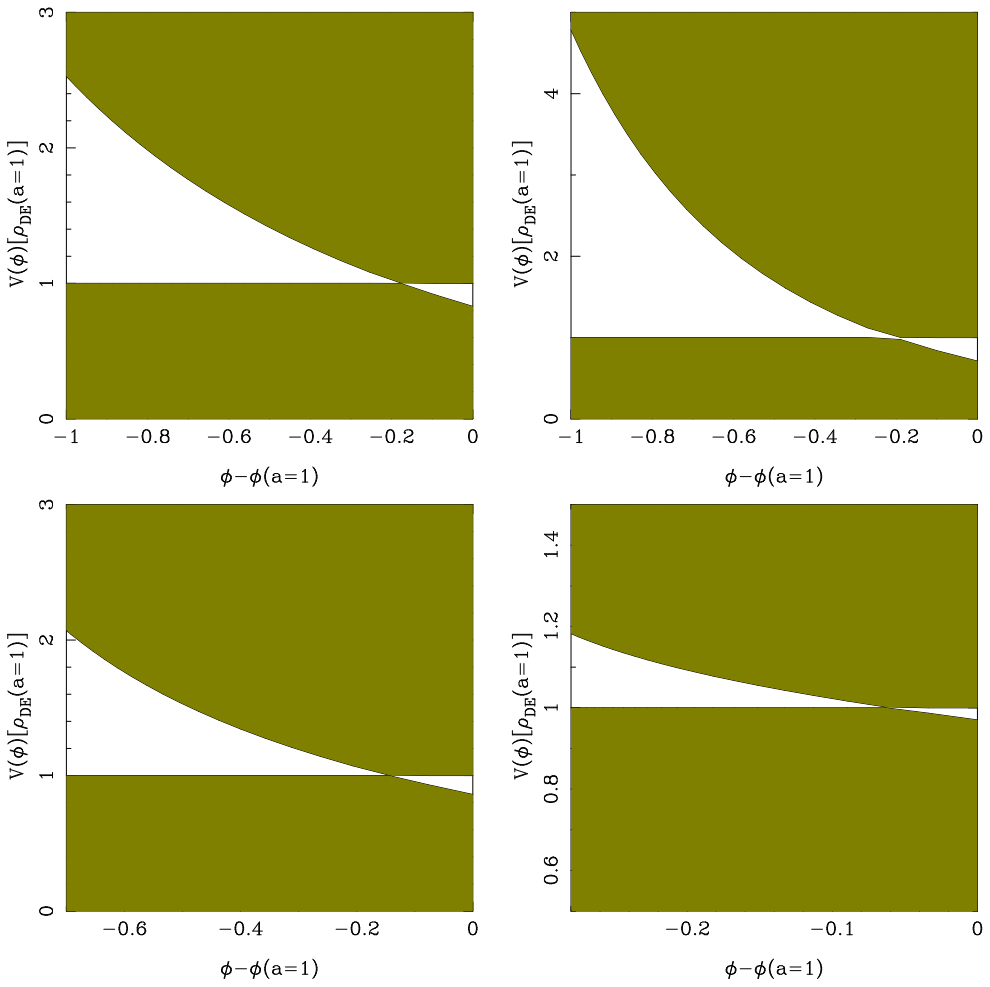

Figure 4.5: The plots show allowed regions at the 3σ level for the quintessence scalar field potential $V(\phi)$ as a function of the field ϕ reconstructed from the wCDM model. The first and second plots in the first row are the results obtained from the analysis of SNIa, BAO and the plots in second row are results obtained from H(z) and combined datasets respectively. We have taken the envelope of the family of curves corresponding to different values of the equation of state parameter.

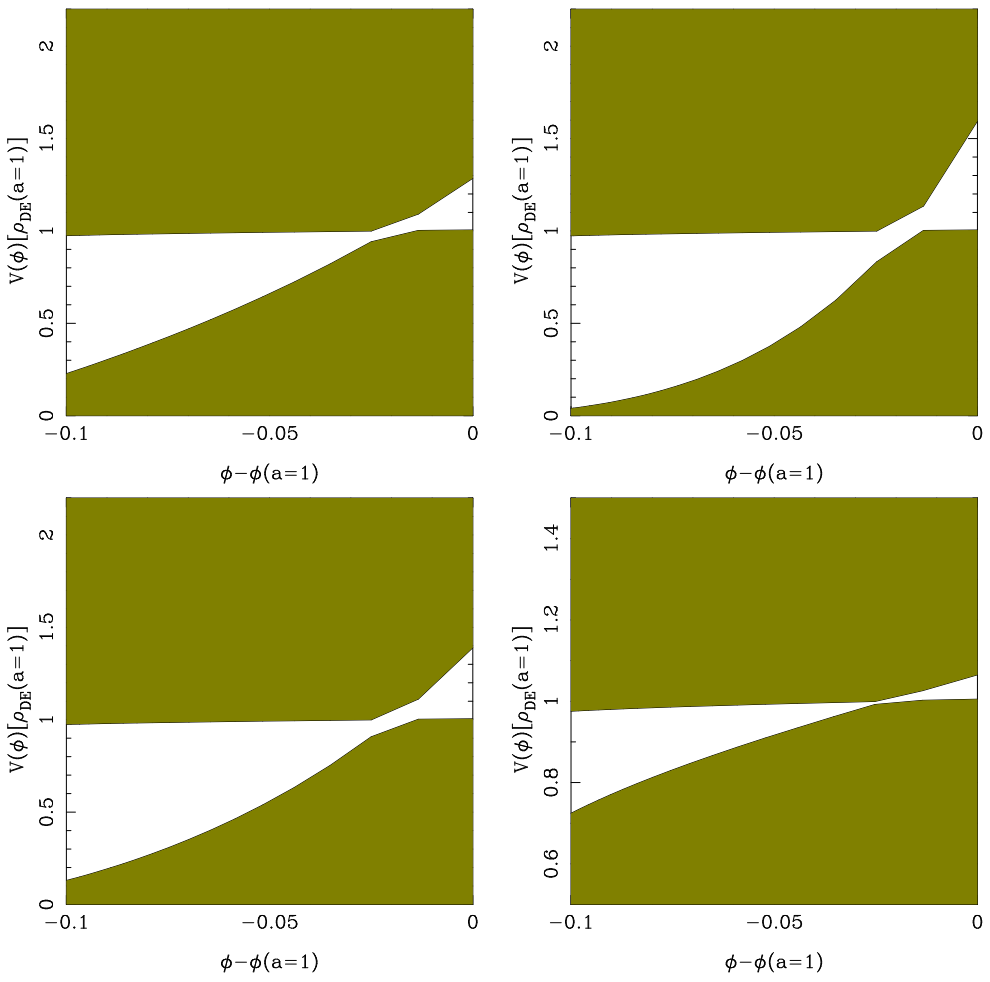

Figure 4.6: The plots show allowed regions at the 3σ level for the phantom scalar field potential $V(\phi)$ as a function of the field ϕ reconstructed from the wCDM model. The order in which the plots are presented is the same as in 4.5.

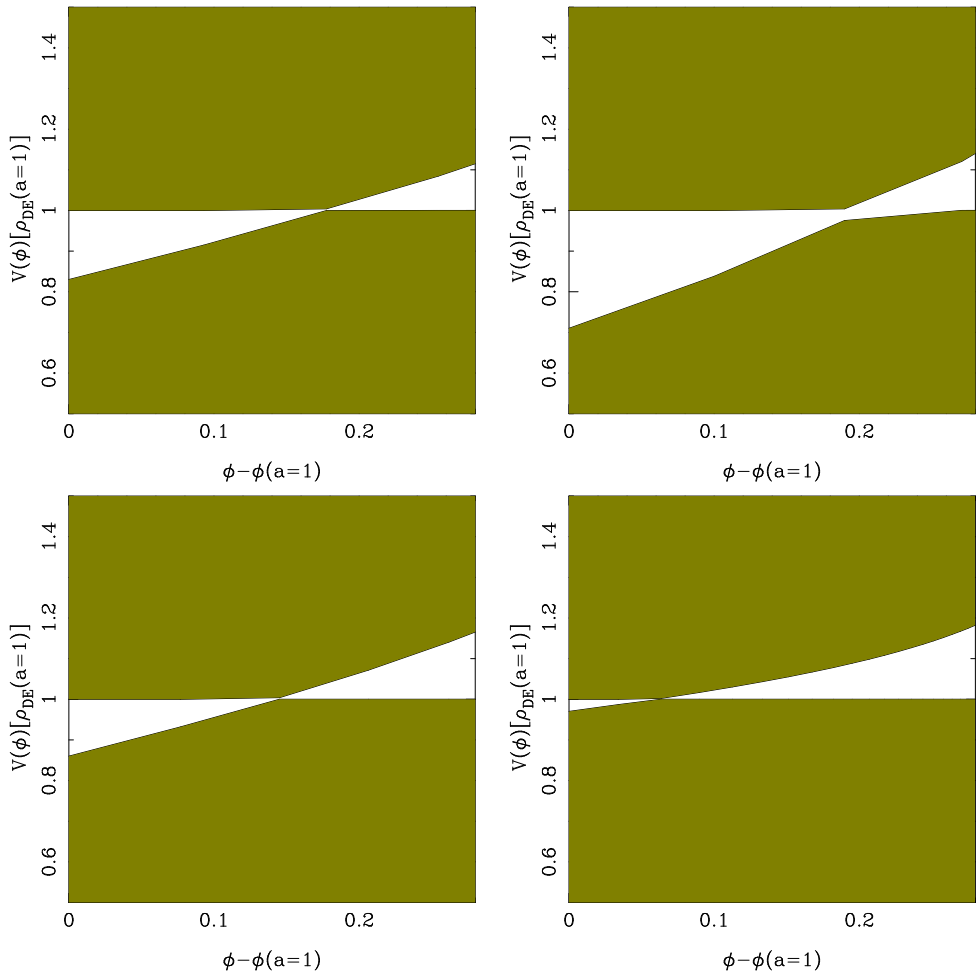

Figure 4.7: The plots show 3σ allowed regions for field potential $V(\phi)$ versus field ϕ reconstructed from wCDM model for the branch where $d\phi/da$ is negative. The plots are obtained for quintessence scalar field potential. The sequence is same as in figure 4.5.

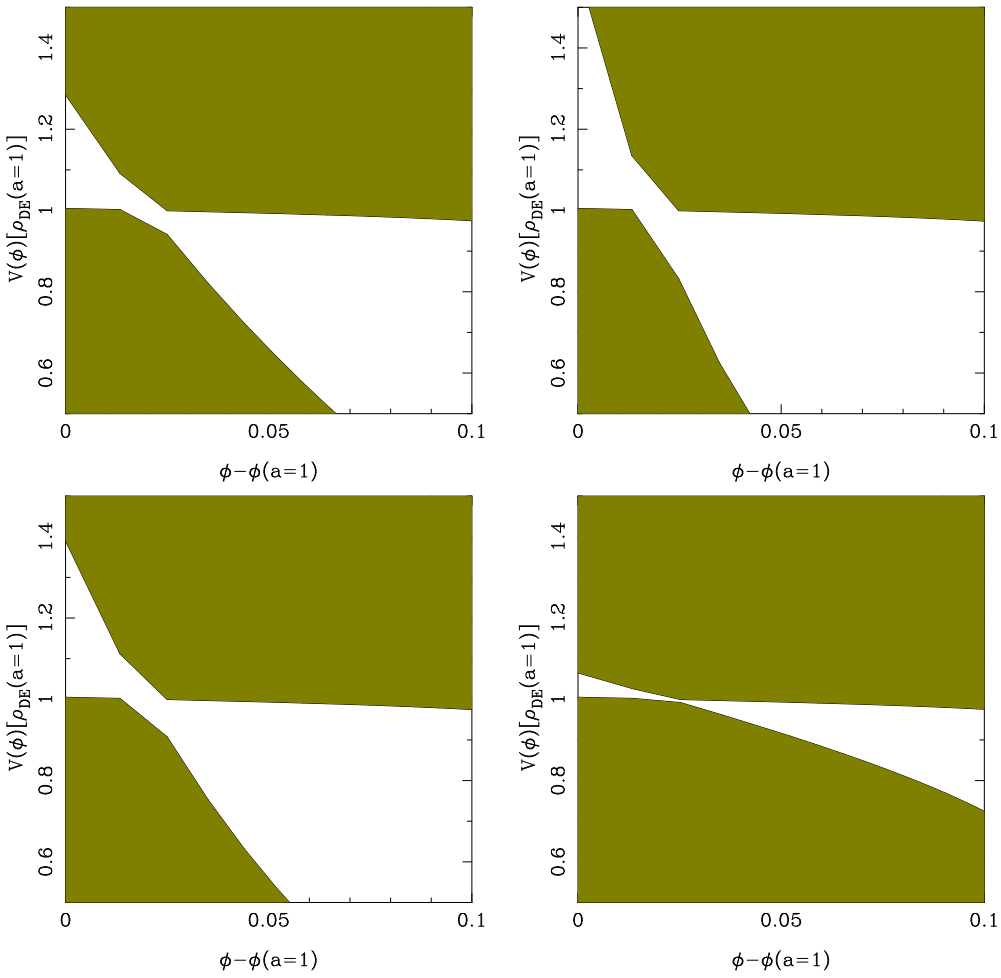

Figure 4.8: The plots show 3σ allowed regions for phantom scalar field potential $V(\phi)$ versus field ϕ reconstructed from wCDM model for the branch where $d\phi/da$ is negative. The sequence is same as in figure 4.5.

field ϕ, this potential takes the exponential form. The functional form of this potential (equation 4.15), take the the same form as in a purely dark energy universe. Therefore, safe to assume that the potential can be reconstructed in a dark energy only universe.

We now consider the models where the equation of state parameter is a function of time. We first consider the CPL parameterization (4.3) which is the parameterization employed in most dark energy studies. It has been pointed out that barotropic fluids are not consistent with a freezing type behaviour [100, 101] in general and in particular for the CPL parameterization which is the scenario we will discuss next.

The variation of the scalar field (ϕ) as a function of the scale factor a for the CPL parameterization can be expressed as,

$$\left[\frac{d\phi}{da}\right]^2 = \pm\frac{[1+w_0+w'(1-a)]\rho_{DE}}{a^2H^2}. \tag{4.16}$$

Here again, the plus sign is for a quintessence field and the negative sign is for a phantom field. For further discussion we have considered $\frac{d\phi}{da}$ to be positive. The conditions for the CPL parameterization to emulate quintessence like behaviour are $w_0 + w' \geq -1$ and $w_0 > -1$. These conditions ensure that the equation of state parameter, $w(a)$ is always greater than -1 at all times. On the other hand, the condition $w_0 + w' < -1$, along with $w_0 < -1$, ensures that the equation of state parameter, $w(a)$, is less than -1, for all values of a and hence the equation of state parameter is phantom like at all times.

In the low redshift regime, when the dark energy density is the dominant factor in the total energy of the universe, the scalar field potential can be expressed as,

$$\tilde{V}(a) = \frac{1}{2}[1-w_0-w'(1-a)]a^{-3(1+w_0+w')}e^{-3w'(1-a)} \tag{4.17}$$

and scalar field is given as

$$\begin{aligned}\tilde{\phi}-\tilde{\phi}_0 \quad &= 2\sqrt{3}\Bigg[\sqrt{\pm(1+w_0+w'(1-a))}-\sqrt{\pm(1+w_0)} \\ &+\frac{\sqrt{\pm(1+w_0+w')}}{2}ln\left\{\frac{\sqrt{\pm(1+w_0+w'(1-a))}-\sqrt{\pm(1+w_0+w')}}{\sqrt{\pm(1+w_0+w'(1-a))}+\sqrt{\pm(1+w_0+w')}}\right\} \\ &-\frac{\sqrt{\pm(1+w_0+w')}}{2}ln\left\{\frac{\sqrt{\pm(1+w_0)}-\sqrt{\pm(1+w_0+w')}}{\sqrt{\pm(1+w_0)}+\sqrt{\pm(1+w_0+w')}}\right\}\Bigg].\end{aligned} \tag{4.18}$$

Since the equation of state parameter is an expansion about its present day value, it is expected that the reconstructed potential is close to that of the case with a constant w

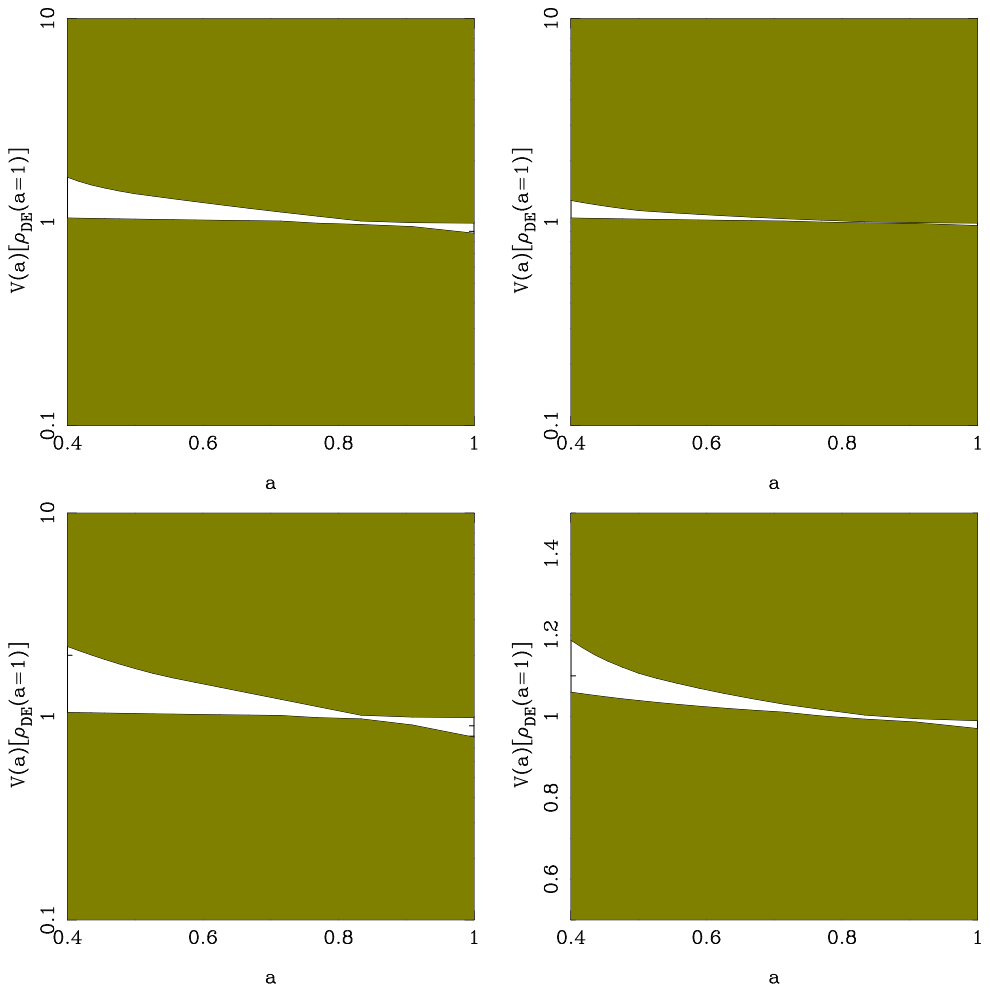

Figure 4.9: The plots in the rows represent 3σ allowed regions for quintessence scalar field potential reconstructed from $w(a) = w_0 + w'(1-a)$ parameterization as a function of scale factor. As before, the potential is scaled by present value of the dark energy density $[\rho_{DE}(a=1)]$. The plots in first rows are obtained for SNIa and BAO data and the plots in second row resulted from the analysis of H(z) data and combined analysis of the three data sets.

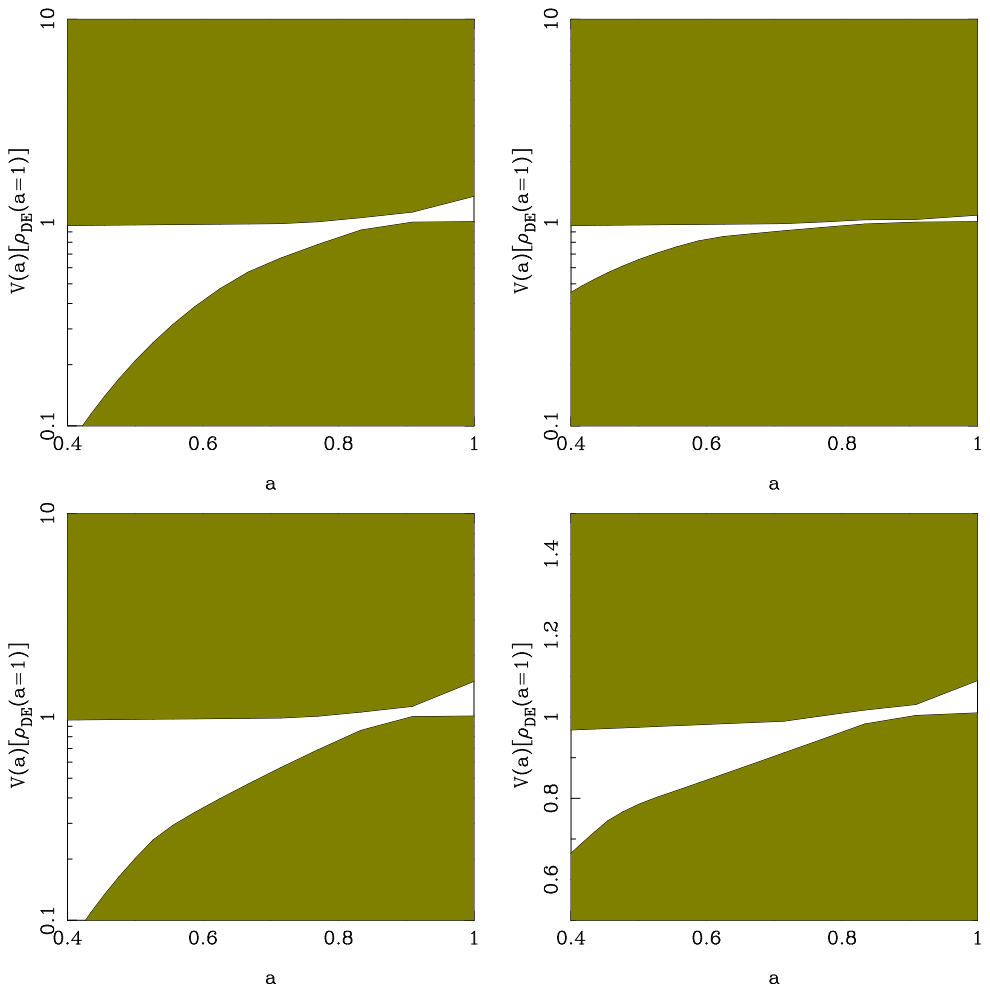

Figure 4.10: The plots in the rows represent 3σ allowed regions for potential reconstructed from $w(a) = w_0 + w'(1-a)$ parameterization as a function of scale factor. The potential is scaled by present value of the dark energy density $[\rho_{DE}(a=1)]$. The order of plots is same as in fig. 4.9. The plots are obtained for phantom field.

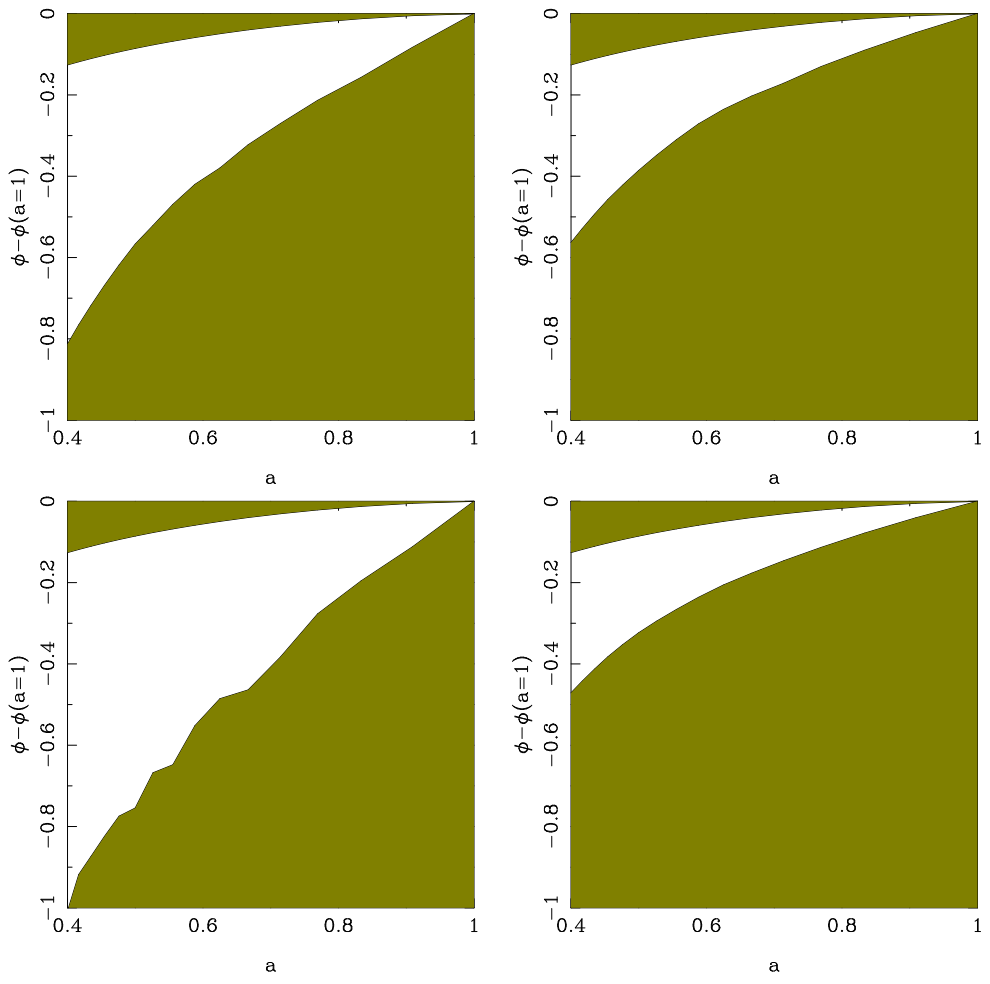

Figure 4.11: The figure represents 3σ allowed regions for quintessence field ϕ versus scale factor reconstructed from $w(a) = w_0 + w'(1-a)$ parameterization. The plots are shown in the same order as in fig. 4.9.

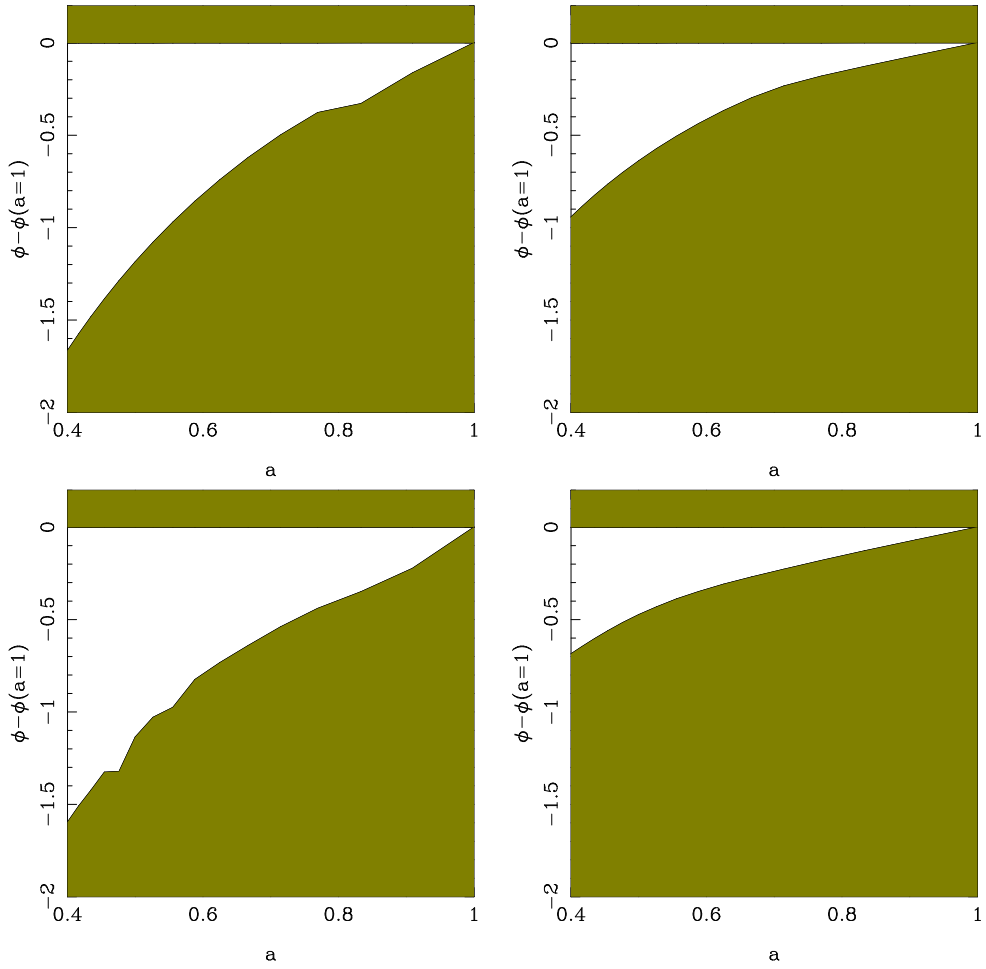

Figure 4.12: The figure represents 3σ allowed regions for phantom scalar field ϕ versus scale factor reconstructed from $w(a) = w_0 + w'(1-a)$ parameterization.

with a slight increase in the allowed range of parameters. We explore this aspect in the next section.

We now consider the scenario where the equation of state parameter is a function of the logarithm of redshift or the scale factor. The variation of the scalar field ϕ with the scale factor in this case is expressed as,

$$\left[\frac{d\phi}{da}\right]^2 = \pm\frac{[1+w_0-w'log(a)]\rho_{DE}}{a^2H^2} \tag{4.19}$$

Since dark is dominant in the low redshift regime, we have neglected the contribution of matter, and for the scalar field potential can then be expressed as

$$\tilde{V}(a) = \frac{1}{2}[1-w_0+w'log(a)]a^{-3(1+w_0-w'log(a)/2)} \tag{4.20}$$

and quintessence scalar field is given as

$$\tilde{\phi}-\tilde{\phi}_0 = -\frac{2}{\sqrt{3}}\left[\frac{(1+w_0-w'log(a))^{3/2}}{w'}-\frac{(1+w_0)^{3/2}}{w'}\right], \tag{4.21}$$

with the corresponding expression for a phantom scalar field given by

$$\tilde{\phi}-\tilde{\phi}_0 = \frac{2}{\sqrt{3}}\left[\frac{(w'log(a)-w_0-1)^{3/2}}{w'}-\frac{(-w_0-1)^{3/2}}{w'}\right]. \tag{4.22}$$

In this case, we can obtain a closed form for the scalar field potential, and the expression for quintessence scalar field potential is given by

$$\begin{aligned}\tilde{V}(\tilde{\phi}) &= \tfrac{1}{2}\left[2-\left\{(1+w_0)^{3/2}-\tfrac{3w'}{2\sqrt{3}}(\tilde{\phi}-\tilde{\phi}_0)\right\}^{2/3}\right] \\ &exp\left[-\tfrac{3}{2w'}\left\{(1+w_0)^2-\left[(1+w_0)^{3/2}-\tfrac{3w'}{2\sqrt{3}}(\tilde{\phi}-\tilde{\phi}_0)\right]^{4/3}\right\}\right]\end{aligned} \tag{4.23}$$

and phantom scalar field potential in terms of $\tilde{\phi}$ is given by

$$\begin{aligned}\tilde{V}(\tilde{\phi}) &= \tfrac{1}{2}\left[2+\left\{\tfrac{3w'}{2\sqrt{3}}(\tilde{\phi}-\tilde{\phi}_0)+(-w_0-1)^{3/2}\right\}^{2/3}\right] \\ &exp\left[-\tfrac{3}{2w'}\left\{(1+w_0)^2-\left[\tfrac{3w'}{2\sqrt{3}}(\tilde{\phi}-\tilde{\phi}_0)+(-w_0-1)^{3/2}\right]^{4/3}\right\}\right].\end{aligned} \tag{4.24}$$

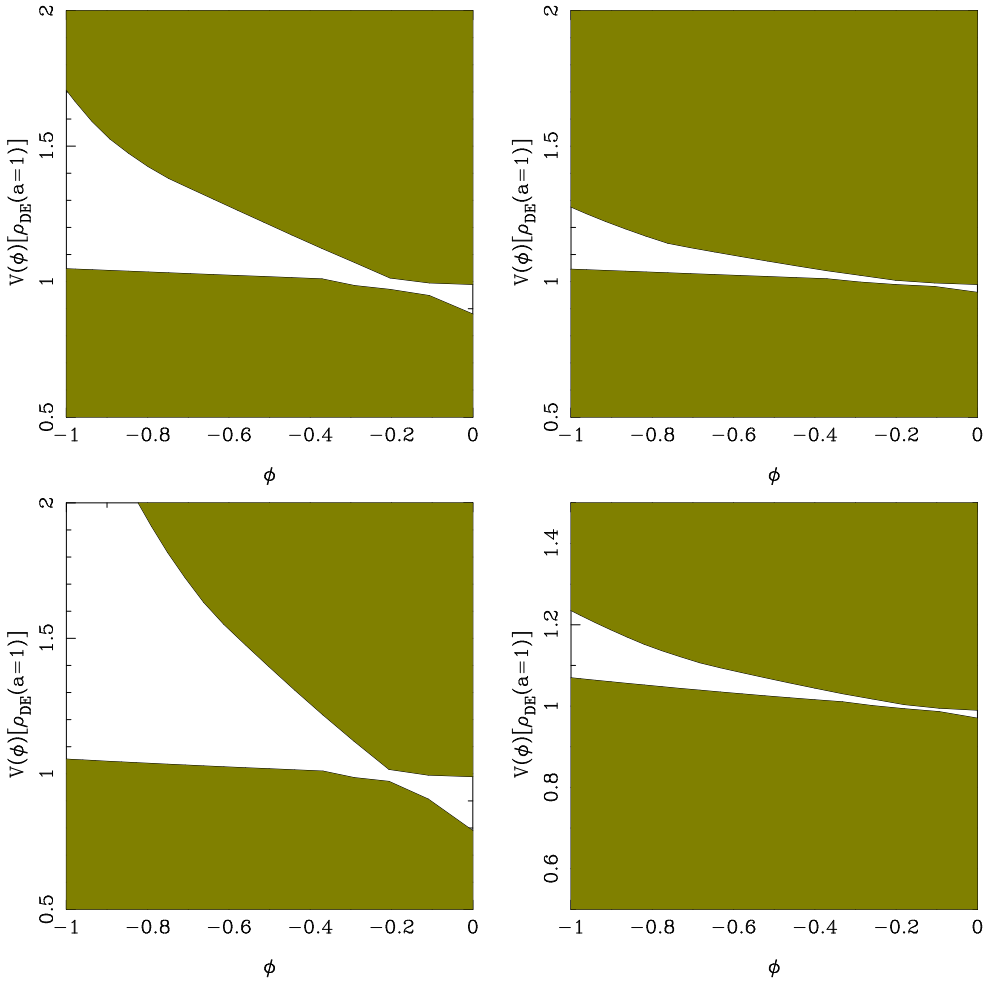

Figure 4.13: The plots in the rows show 3σ allowed regions for quintessence field potential $V(\phi)$, scaled by the present dark energy density $[\rho_{DE}(a=1)]$ versus field ϕ reconstructed from $w(a) = w_0 + w'(1-a)$ parameterization. The plots in both first row represent the results obtained from SNIa and BAO. The result from the analysis of H(z) and combined data sets is shown in plots in second row.

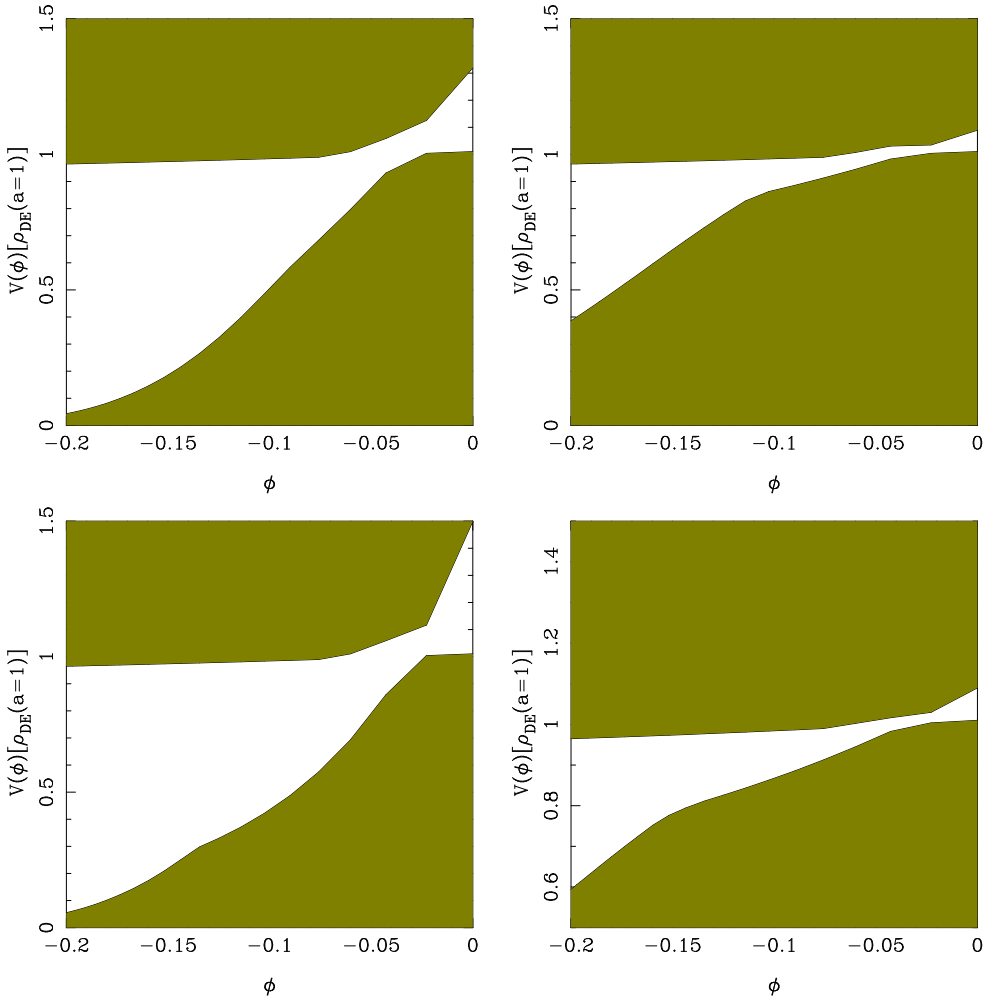

Figure 4.14: The plots in the rows show 3σ allowed regions for phantom scalar field potential $V(\phi)$ versus field ϕ reconstructed from $w(a) = w_0 + w'(1-a)$ parameterization. The phantom potential is scaled by the present dark energy density $[\rho_{DE}(a=1)]$. The plots in both the rows are in same order as in Fig. 4.13.

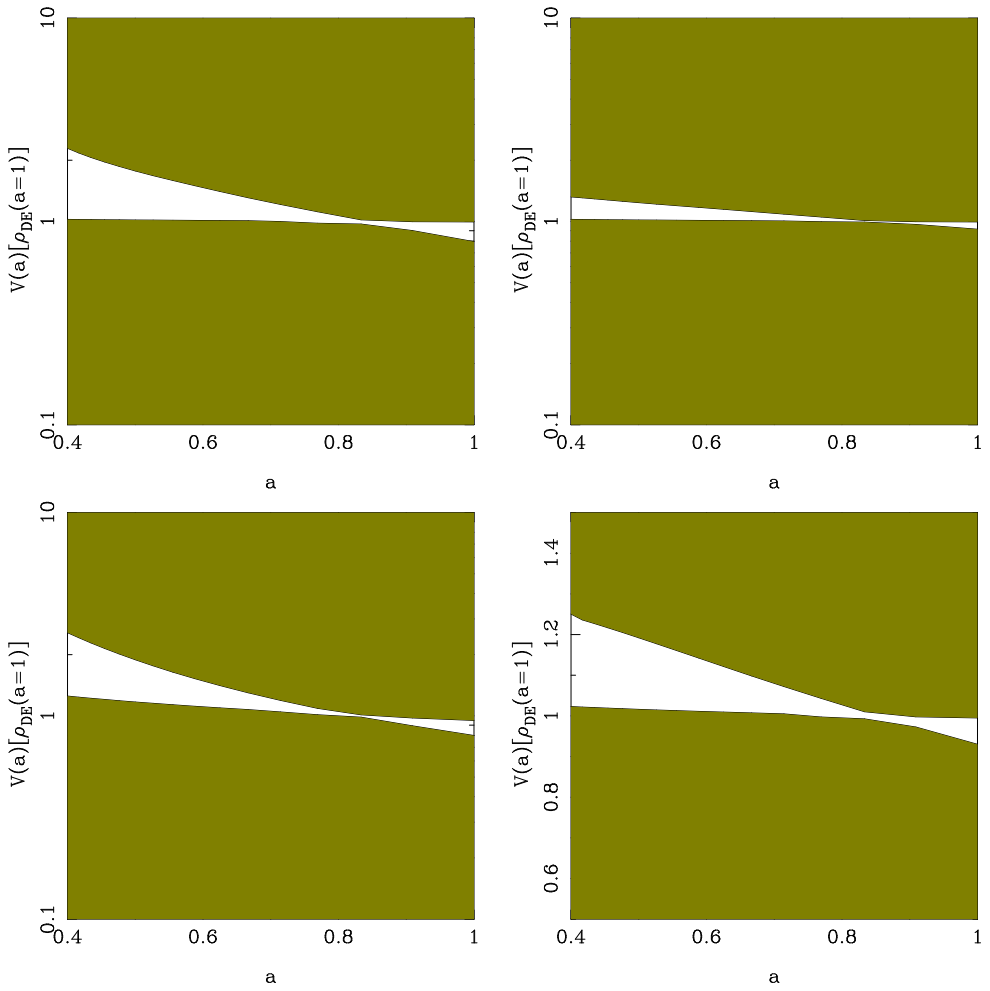

Figure 4.15: The plots in the rows represent 3σ allowed regions for quintessence scalar field potential, scaled by the present dark energy density $[\rho_{DE}(a = 1)]$, reconstructed from $w(a) = w_0 - w' \log(a)$ parameterization versus scale factor. The sequence of plots is the same as before.

4.3 Constraints from different datasets

In this section, we discuss the observational constraints on the variation of the reconstructed scalar field potential from different data sets and on the reconstructed scalar field potentials as a function of the field corresponding to a fluid dark energy equation of state. The individual data sets allow a higher range of variation and when combined, the resulting allowed range is significantly narrower as a result of tighter constraints on parameters.

In Fig. 4.1, we have plotted the 3σ allowed regions for the reconstructed potential as a function of the scale factor a, for the constant equation of state parameter (wCDM) model. We have plotted $V(a)/\rho_{DE_0}$ vs a for quintessence (the first row) and phantom

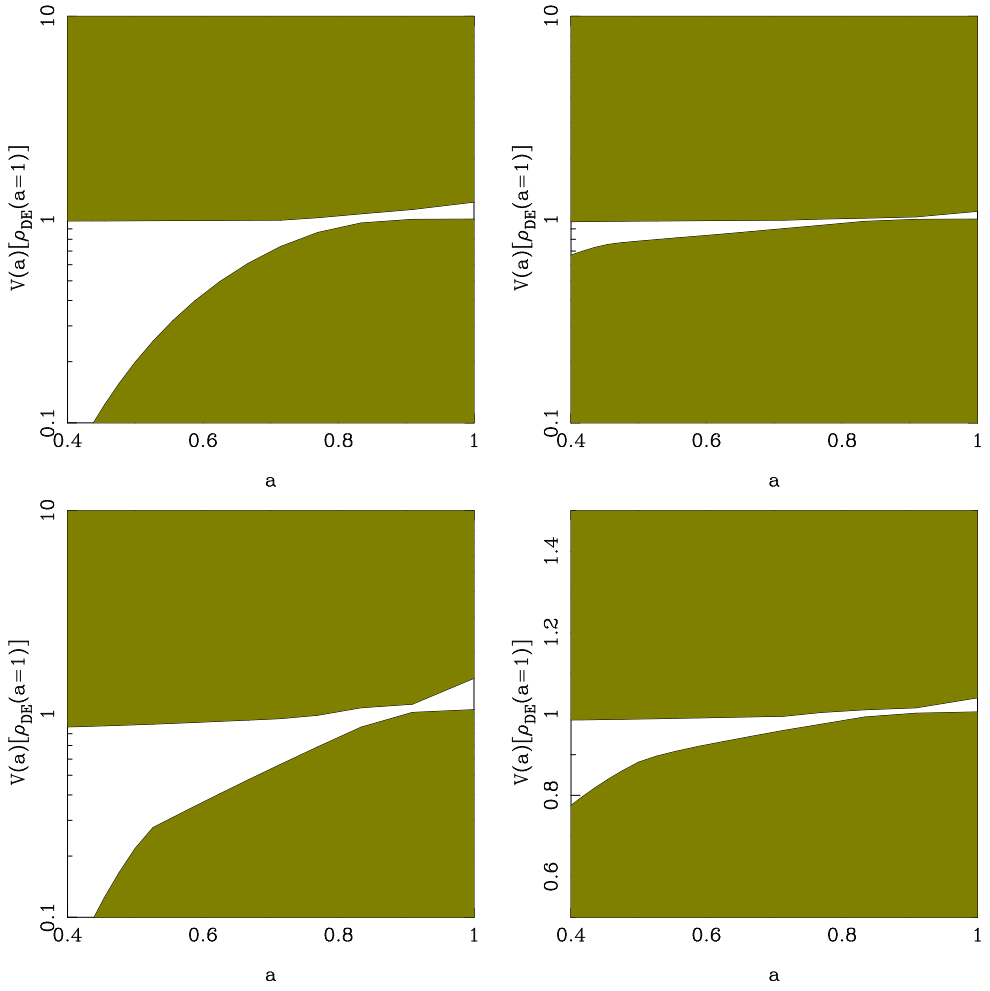

Figure 4.16: The plots in the rows represent 3σ allowed regions for phantom field potential versus scale factor. The potential is reconstructed from $w(a) = w_0 - w' \log(a)$ parameterization and scaled by the present dark energy density $[\rho_{DE}(a = 1)]$. The sequence of plots is the same as before.

(the second row). For quintessence, the allowed range lies below unity when $a > 0.8$ and for $a < 0.8$, this range lies above $V(a)/\rho_{DE_0}$ =1 line.

As the value of a decreases from one, the allowed range begins to get narrower till it reaches $a \sim 0.8$, where it is narrowest. With further decrease in a, the allowed range starts increasing again. The phantom potential shows a behaviour opposite to that of quintessence field but with a similar switch in allowed range at $a \sim 0.8$.

In Fig. 4.5, we show the 3σ allowed regions for reconstructed potentials as a function of scalar field, ϕ, for the wCDM model. We have plotted $V(\phi)/\rho_{DE_0}$ vs ϕ, where ϕ is in units of $\sqrt{8\pi G}$. In Fig. 4.3, we show the 3σ allowed regions for scalar field ϕ as a function of scale factor, a, for wCDM model. The value of the scalar field is in units of M_{pl}^{-1}. The plots in the two rows of Fig. 4.3 shows the results obtained from the analysis of SNIa, BAO and H(z) data sets respectively. As before, the plots in first row are for a quintessence field and plots in the second row shows allowed range for a phantom field and the results from the combined analysis. In the case of a varying equation of state parameter, the allowed range of the dark energy density variation increases as compared to the wCDM model. The family of curves representing the scalar field potential as a function of the field have a fairly restricted range of variation for the quintessence models. For phantom like models, the allowed range increases as compared to the wCDM case. Here we have plotted the envelope of family of curves corresponding to the allowed range in w, the curve is defined by the function $V(\phi)$ and the constants.

In Fig. 4.13 we show the variation of scalar field potential $V(\phi)$ as a function of the field ϕ for the CPL scenario. These solution are valid only under the assumption that the scale factor is very close to its present day value, i.e., valid at late times. In Fig. 4.9, 3σ allowed region is shown for potentials reconstructed from CPL model. The phantom potential shows a similar behaviour as in the wCDM case. The Fig. 4.15 shows the allowed range of potential for the logarithmic parameterization. In this case also, the narrowest range is obtained from BAO data sets which when combined with other data sets restricts the range further. The corresponding field versus scale factor plots for scalar field, derived from CPL model, are shown in Fig. 4.11.

Fig. 4.13 represents the 3σ allowed regions for the reconstructed potential as a function of scalar field, ϕ, for the CPL model. Fig. 4.17 shows the results obtained for logarithmic parameterization. The allowed ranges obtained for the logarithmic parameterization from the individual datasets and combined analysis are shown in Fig. 4.19. The plots show that the profiles of uncertainty associated with the best fit curves of the

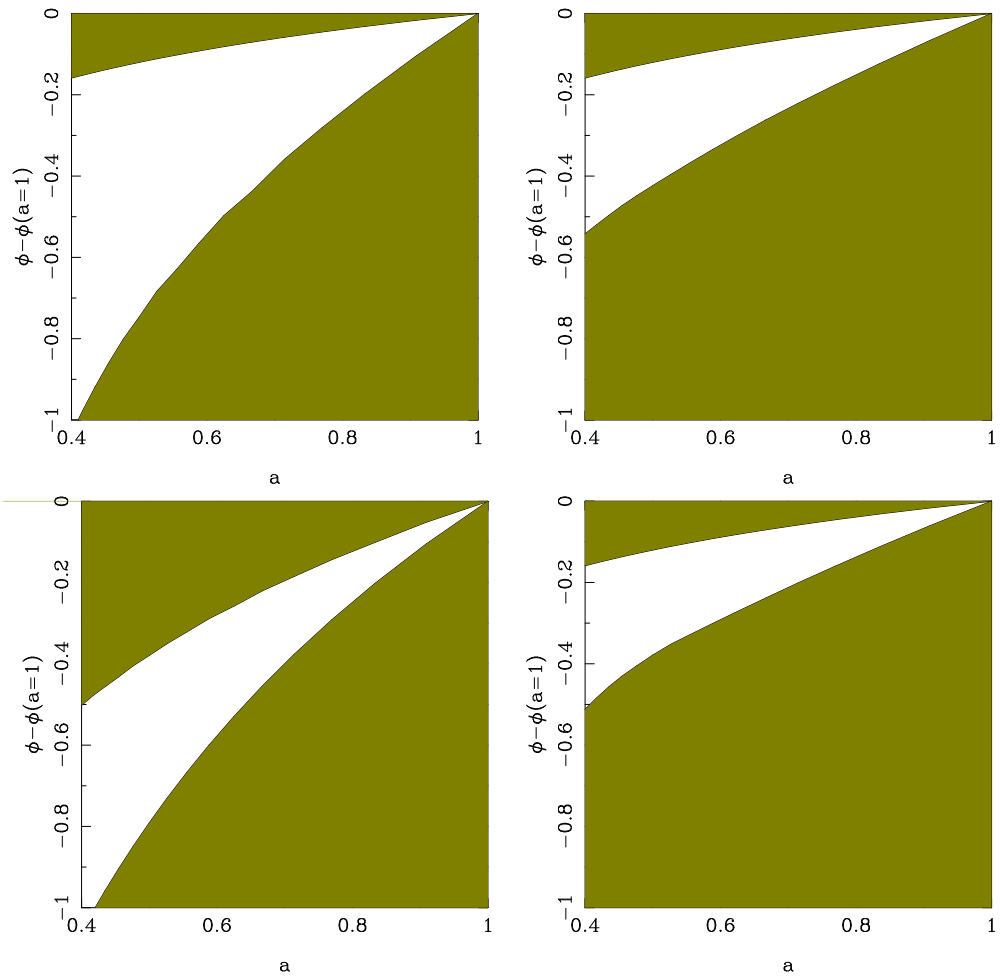

Figure 4.17: The plots in the rows represent 3σ allowed regions for quintessence scalar field ϕ versus scale factor reconstructed from the CPL parameterization. The order of plots is same as before.

scalar field for these two models are different. The dark energy potential shows similar behaviour for these models.

In all the models considered above, the results in general are similar to each other. The most stringent constraints on the variation of the scalar field as a function of scale factor are due to the BAO data and as a result the combination of different datasets allows for a limited range too. More data at different redshifts will further limit this range.

We attempted to connect two alternate explanations of dark energy, namely barotropic fluid models and scalar field models by way of reconstructing scalar field potentials which emulate the barotropic equation of state. We assume a constant dark energy equation of state parameter, a slowly varying function of redshift and a logarithmic growth with

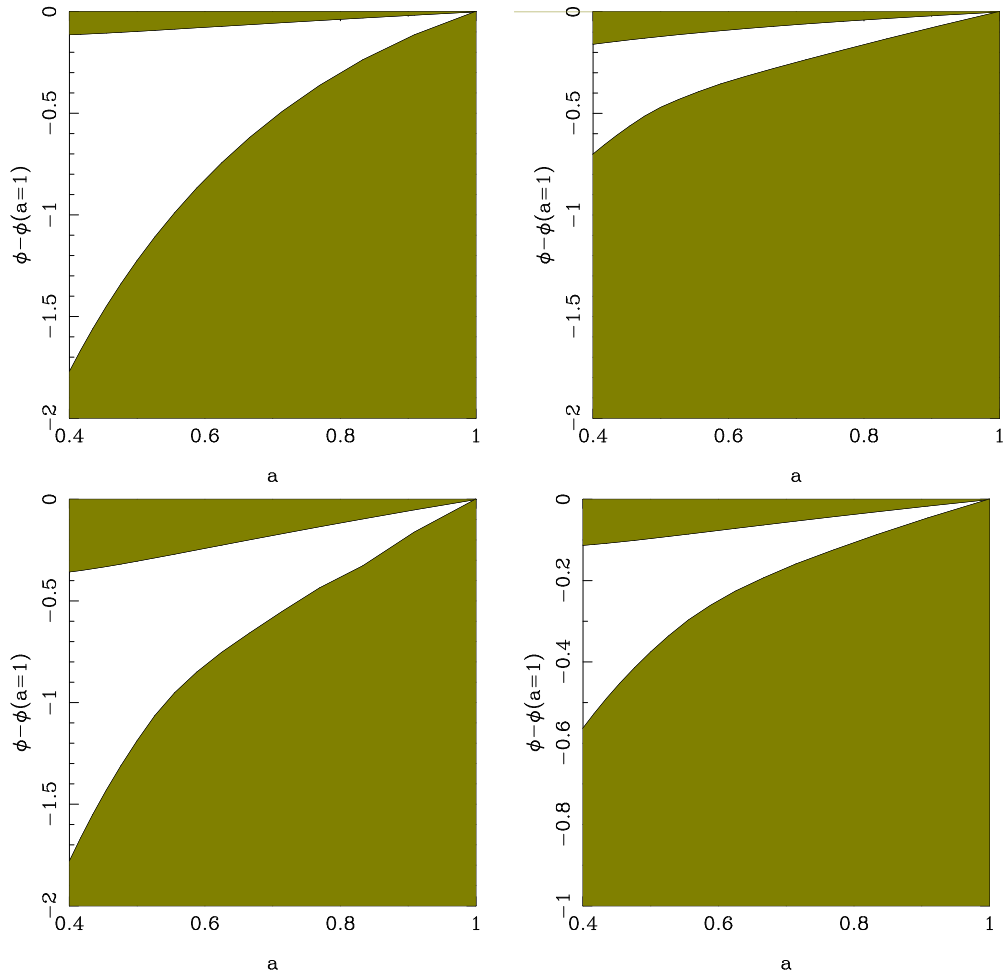

Figure 4.18: The plots in the rows represent 3σ allowed regions for phantom scalar field ϕ as a function of scale factor reconstructed from the CPL parameterization. The sequence of plots is the same as before.

respect to the the redshift for this reconstruction. The assumptions are reasonable as a combination of low redshift observations, restrict the allowed range of the evolution of dark energy density. Since it is straightforward to parametrize the dark energy equation of state and constrain its parameters, therefore, we constrain the cosmological parameters and using parameters allowed by individual and combined datasets, we obtain a range in variation of the scalar field potential. We study quintessence and phantom nature of dark energy and reconstruct the respective potentials for these models and obtain semi-analytical forms for the scalar field potentials. In this context, it is worth mentioning that for fluid models, a transition from quintessence to phantom like behaviour is straightforward as both the behaviours are described by the same equation of state. This is not the case for scalar field models as the equations describing the dynamics are fundamentally different from each other. Because the dynamics of the two scalar fields are different, we use different priors for quintessence and phantom field, namely we assume the parameter sets such that the evolution of the equation of state parameter does not cross over the $w = -1$ (the phantom) divide. The energy density for quintessence scalar field decays with the scale factor, and in the case of phantom field the behaviour is opposite to that of a quintessence field.

The evolution of the scalar field has very similar behaviour for both, quintessence and phantom. The uncertainty in the reconstructed potential is much higher when the analysis is carried out with individual data sets and the evolution of the potential is well constrained in the combined analysis with the data sets, namely SNIa, BAO and H(z) data. The allowed range is obtained to be minimum at $0.8 < a < 0.9$, and it slightly increases at $a \sim 1$. This profile of uncertainty of the reconstructed potential is very similar for all the three models considered in this paper.

The potential for the wCDM model (scaled by its present day value) remains close to the value of unity, which is the boundary between the quintessence and phantom class of dark energy. The constant equation of state parameter model accommodates an exponential potential, belonging to thawing class of models. The slope of the potential and its amplitude depends on the equation of state of the dark energy fluid. If the matter contribution is also taken into account, the potential also accommodates a slow-rolling nature. For both the scenarios, namely the quintessence and phantom models of dark energy, the evolution of the potential tends to converge to a narrow range. For scenarios with varying dark energy parameterizations, the observations restrict the variation significantly. To study dark energy perturbations, the sound speed is considered as a parameter in fluid models of dark energy. Since the pressure gradients are more easily computed in scalar field models, the reconstructed potentials are hence of help in studying perturbations in

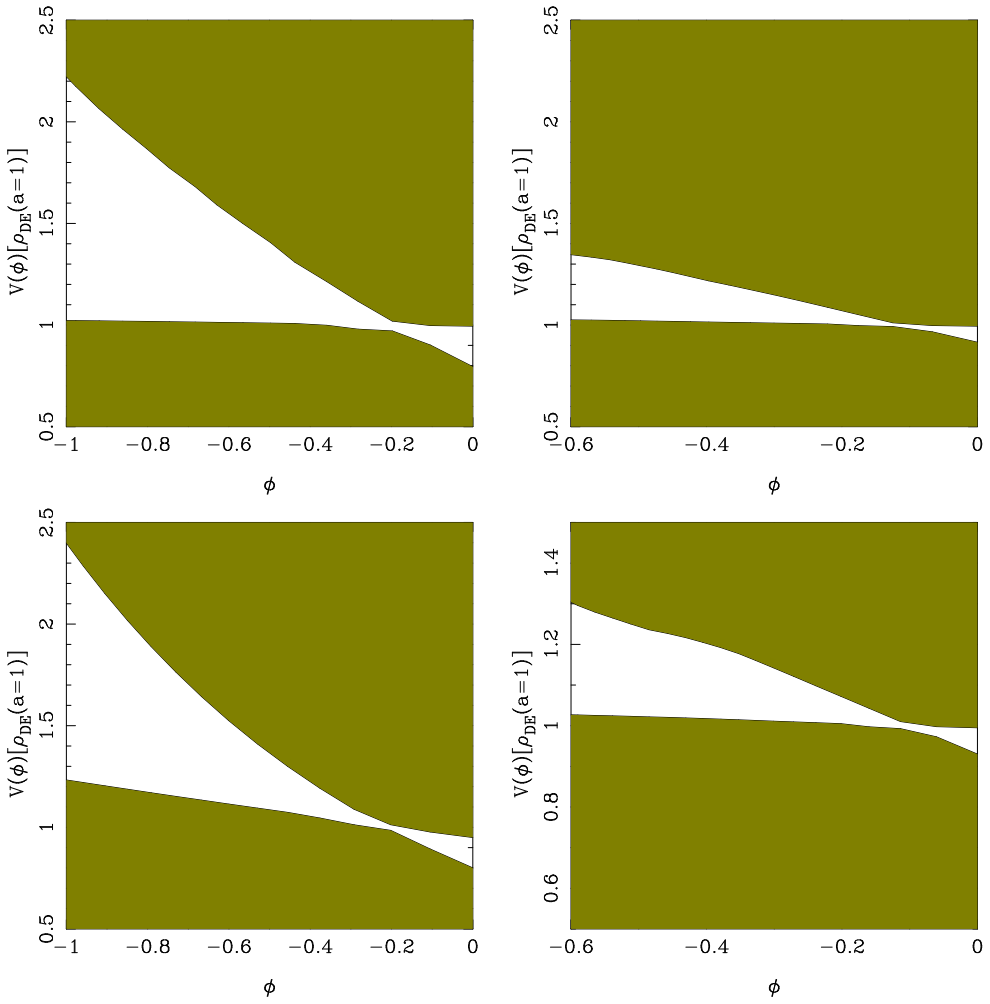

Figure 4.19: The plots show 3σ allowed regions for quintessence scalar field potential $V(\phi)$ versus field ϕ. The potential is reconstructed from $w(a) = w_0 - w' \log(a)$ parameterization and scaled by the present dark energy density $[\rho_{DE}(a = 1)]$.

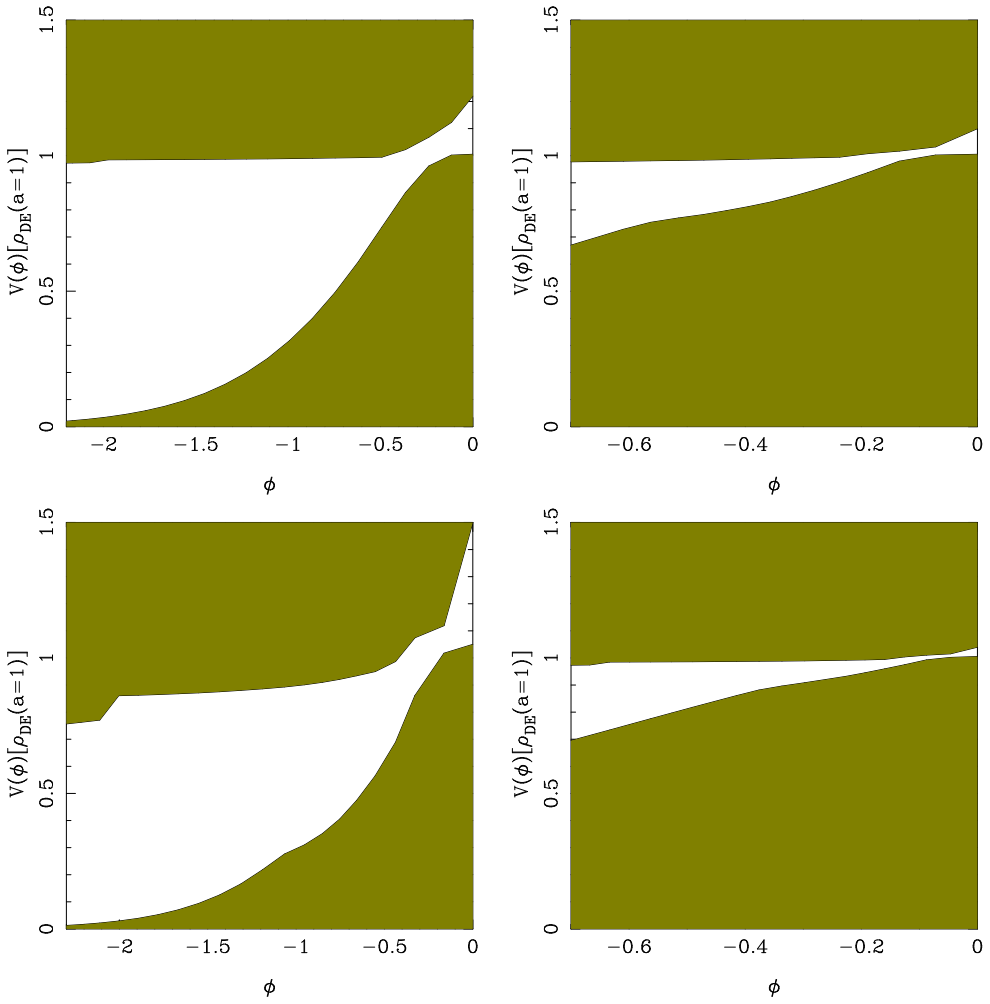

Figure 4.20: The plots show 3σ allowed regions for field potential $V(\phi)$, scaled by the present dark energy density $[\rho_{DE}(a = 1)]$, versus field ϕ reconstructed from $w(a) = w_0 - w' \log(a)$ parameterization.

these scenarios. The large scale structure data would further rule out models using data in addition to distance measurements. Fluid models are effectively used as a representation for dark energy, and analytical connection between common parameterizations and scalar field models is therefore of significance for further studies.

Chapter 5

Summary and future directions

In this thesis we discuss various observational constraints on cosmological parameters. We are especially interested in studing properties of fluid models and scalar field models of dark energy.

We begin with a discussion of the basic concepts that we need to understand cosmology. Observational evidence indicates that the expansion of the Universe at present is an accelerating one. The known non-relativistic matter as well as the relativistic matter provides only a decelerating expansion, which was the nature of expansion in the past. Thus, to account for the observed accelerating expansion, one assumes the presence of dark energy. The component has large negative pressure. The energy density of the universe and its expansion rate depends upon the contribution of each of these components. Earlier the relativistic component was dominant, followed by non-relativistic component, and recently the dark energy component became the dominant component, accelerating the expansion of the universe. The different cosmological constraints (studied in this thesis) are due to distance measurements. The distances measured are the luminosity distance to a standard candles, or the angular diameter distance to an object with a known angular size. The supernovae data is sensitive to the luminosity distance and the BAO data is a function of the angular diameter distance. We review these observations and also those of direct measurements of the Hubble parameter. These observations are used to constrain the cosmological parameters of interest for models considered in this work.

We next consider a fluid model of dark energy and tried to constrain the cosmological parameters. Models base on isotropic fluids provide a description of dark energy which can account for the late time acceleration of the universe as far as determination of dark

energy parameters are concerned. For an isotropic fluid, the equation of state is same in all directions. The equation of state is given by $p = w\rho$, where p, ρ denotes the energy density and pressure and w is the equation of state parameter. We ignore the contribution of relativistic term as we are interested in late time evolution of the universe and we consider a flat universe. We considered two types of model in this chapter: first model has a constant equation of state and in the second type the equation of state parameter is a function of time. The first model where w is considered to be a constant, is the simplest model where dark energy is dynamical. This model is described by two parameters; Ω_m and w. We find that the ΛCDM model is consistent with all the observations. Constraints from BAO are orthogonal to that of SNIa and H(z) data. As a result, constraints obtained from the analysis of combination of datasets provides tighter constraints. For a varying equation of state models, we consider two parameter descriptions of $w(z)$. The three different parametrizations are considered in this category; I) CPL parametrization, II) JBP parametrization, and III) Logarithmic parametrization. The models in this case are described by three parameters: Ω_m, w_0 and $w'(z = 0)$. Here, Ω_m is the energy density parameter for non-relativistic matter at present, w_0 is the equation of state at present, and $w'(z = 0)$ is the first derivative of equation of state parameter at present. Performing χ^2 analysis and using the three datasets we present constraints on these parameters. To obtain the contours corresponding to 67%, 95% and 99% between any two parameters, we marginalize over the third parameter. For CPL and JBP parametrizations, we find that on marginalization over $w'(z = 0)$, SNIa observations prefer higher values of Ω_m as compared the other two datasets. The SNIa data prefers dark energy of phantom origin. Other data sets, BAO and H(z) data, however prefer quintessence like models and are consistent with $w = -1$. BAO and H(z) data sets also allows the decelerating models for these two parametrizations. In case of logarithmic parametrization, all the three models are in good agreement with ΛCDM model. When all the observation are combined and analysis is done, the resultant allowed range of parameters is lower as compared to that of individual datasets. When no marginalization is performed on any parameters, all the datasets for the three parametrizations are consistent with a cosmological constant description.

Scalar fields provide another description of dark energy where the late time acceleration can be a manifestation of the form of the potential considered. The equation of state of the field is a function of time and space. The evolution of field is described by the form of potential considered. If we consider a slow rolling potential, it would lead to late time acceleration, where the onset of acceleration depends upon the initial conditions. We consider a canonical scalar field called quintessence which is minimally coupled to

gravity. We consider thawing scalar field models. In thawing scalar field, the field is frozen because of the large Hubble damping term at earlier times. This causes the kinetic term to be very small, which can be neglected as compared to potential term. The model in this case behaves live cosmological constant model. Later, when the mass of the field becomes comparable to the Hubble parameter, the field starts evolving, moving towards the minimum of the potential. At this stage, the contribution of the kinetic term becomes finite and the equation of state starts evolving away from -1 towards a larger value of w. For this case we considered two types of potentials. We use χ^2 technique for the analysis and constrain the parameters of the models considered. The cosmological constant model is consistent with the observations and BAO observations provide the most stringent constraints on parameters, followed by SNIa and H(z) data respectively. None of the datasets provide lower limit on equation of state parameter in both the models considered. We also study other parameters specific to a particular potential and constrain them. For the model parameters at present, tight constraints are obtained, however, we don't obtain any evidence that these models are inconsistent, therefore, we cannot rule out any of the models. We can constrain their parameters with better precision.

We then proceed to reconstruct the form of scalar field potentials which are consistent with the different parametrizations considered in the fluid model of dark energy. For this we consider quintessence scalar field model and the phantom scalar field models. The equation of state parameter is greater than -1 in case of quintessence field and less than -1 for phantom fields. The kinetic energy is negative for phantom scalar fields while it is positive for quintessence. We study the evolution of the scalar field and obtain the functional and semi-functional form of the potentials. We use χ^2 minimization analysis and the three observations mentioned earlier to constrain the potentials and the scalar field parameters. The scenarios we have considered are w =constant, CPL and logarithmic parametrizations. For w =constant parametrization, if we consider the contribution of dark energy/scalar field only, we get an exponential potential which is of the same form as studied in the quintessence case. It belongs to the thawing scalar field potential, where $w = -1$ at earlier times but grows less negative as the field evolves. We consider the case when the Universe consists of both dark energy as well as non-relativistic matter. We find the function form of the reconstructed potential. If the value of scalar field is large than this potential takes the form of the exponential potentials, behaving as if only scalar field contributes to the total energy of the universe. In the constraints on scalar field parameter, we find that the potential for quintessence decays as the filed evolves from past to present and the value of scale factor approaches the $a = 1$. Similar results, albeit with an opposite sign is obtained for phantom potential where the

field grows as scale factor approaches unity and the field evolves to its present value. The allowed range of quintessence scalar field is found to increase as we go into the past and value of scale factor decreases. For the CPL parametrization and the logarithmic parametrization, we consider a universe dominated by scalar field only and ignored the contribution from other components. In these cases we obtained the functional form of scalar field potential and studied the allowed range of scalar field parameters. The results that we obtain are similar to that of w =constant parametrization. The thawing class of scalar fields are preferred by the observations.

This thesis contains a detailed study of the constraints on various dark energy models. To constrain the parameter, we used recent observational data. We consider different types of models which leads to late time acceleration of the universe. We studied the fluid model and quintessence scalar field models in detail. The constraints are obtained on various parameters which describe the models. We reconcile the fluid model of dark energy and scalar field models and constrain the resulting reconstructed potentials. In this work, we have restricted ourselves to canonical description of scalar fields. A natural extension of this work is a detailed studies of non-canonical scalar fields. Prominent among the non-canonical models is the tachyon fields, where the dynamics are governed by runaway potentials. More importantly, better precision observations will lead to stringent constraints and potentially rule out various models. The equivalence principle implies that the dynamical dark energy needs to be clustered. A study of dark energy perturbations and its implications will allow us to go beyond distance measurements. As more surveys are employed, different data sensitive to different cosmological quantities will be an interesting subject of future study.

Appendix A

χ^2 minimization technique

In data analysis, we consider an observable quantity $X_{i,ob}$ at a known redshift z_i. The observed quantity in our analysis is the luminosity distance, the angular diameter distence and the Hubble parameter. We consider a model and calculate the value of the same observable theoretically $X_{i,th}$ at reddhift z_i. We compare the theoretically calculated and the observed quantities and find the best fit model parameters. The χ^2 analysis tell us about the goodness of the fit, i.e., how much the observables vary from the theoretically calculated one. We draw confidence contours that gives us a certain percentage of total probability distribution for model parameters. The shape of the contours is given by constant χ^2 boundary [102, 103, 104]. We study and compare the confidence contours corresponding to different models, to see if observations favour one model over others.

A.0.1 χ^2 and Likelihood Function

A cosmological data set contains N independent measurements $X_{i,ob}$ measure at redshifts z_i and standard deviations σ_i. For a theoretical model, χ^2 is defined as:

$$\chi^2 = \sum_{i=1}^{N} \frac{\left[X_{th}(z_i) - X_{i,ob}\right]^2}{\sigma_i^2}. \tag{A.1}$$

For a model, χ^2 measures the difference between theoretically predicted values and observations.

χ^2 is zero if observed and expected values are the same, it event is extremely unlikely. Small values of χ^2 corresponds to a good fit between observed data and predicted value.

A large value of χ^2 indicates a poor fit between the model prediction and the observations. The parameters corresponding to the minimum value of χ^2 are called best-fit parameters, and χ^2.In cosmology, the observations $X_{i,ob}$ are independent of each other, giving us a simplified expression for χ^2 A.1. In general, the observations can be dependent, and χ^2 in this case is given by

$$\chi^2 = \left[\boldsymbol{X_{th}} - \boldsymbol{X_{i,ob}}\right]^T V^{-1} \left[\boldsymbol{X_{th}} - \boldsymbol{X_{i,ob}}\right], \tag{A.2}$$

where $\boldsymbol{X_{i,ob}}$ denotes the vector of observations, $\boldsymbol{X_{th}}$ is the vector of the predicted values for a model, and V is the covariance for the measurements. For real cases when observations are independent of each other, V is a diagonal matrix only.

For a cosmological model, the likelihood function $\mathcal{L}$ is given by

$$\begin{aligned} \mathcal{L} &= \exp\left[-\frac{1}{2}\chi^2\right] \\ &= \exp\left[-\frac{1}{2}\left[\boldsymbol{X_{th}} - \boldsymbol{X_{i,ob}}\right]^T V^{-1} \left[\boldsymbol{X_{th}} - \boldsymbol{X_{i,ob}}\right]\right]. \end{aligned} \tag{A.3}$$

We maximize the likelihood function (in other words, minimize χ^2) to find the most probable values of model parameters. Values of the parameters that result in a higher value of the likelihood function are more likely to be true parameters [105]. For this we obtain confidence ranges for the best fit parameters.

Bibliography

[1] P. J. E. Peebles. *Principles of physical cosmology.* Princeton University Press, 1993.

[2] Lee C. Loveridge. Physical and geometric interpretations of the riemann tensor, ricci tensor, and scalar curvature. *General Relativity and Gravitation*, 45(2):167–256, 2003.

[3] K.S. C.W. Misner, Thorne and J.A. Wheeler. *Gravitation.* W. H. Freeman, 1973.

[4] Sean Carroll. *Spacetime and Geometry: An Introduction to General Relativity.* Addison-Wesley, 2003.

[5] E. Hubble. A Relation between Distance and Radial Velocity among Extra-Galactic Nebulae. *Proceedings of the National Academy of Science*, 15:168–173, March 1929.

[6] G. Chen, J. R. Gott, III, and B. Ratra. Non-Gaussian Error Distribution of Hubble Constant Measurements. *PASP*, 115:1269–1279, November 2003.

[7] G. Chen and B. Ratra. Median Statistics and the Hubble Constant. *PASP*, 123:1127, September 2011.

[8] B.S. Ryden. *Introduction to cosmology.* Addison-Wesley, 2002.

[9] A.R. Liddle. *An introduction to modern cosmology.* Wiley, 2003.

[10] D.J. Raine and E.G. Thomas. *An introduction to the science of cosmology.* Series in Astronomy and Astrophysics - Institute of Physics. Institute of Physics Publishing, 2001.

[11] S. Perlmutter, G. Aldering, G. Goldhaber, R. A. Knop, P. Nugent, P. G. Castro, S. Deustua, S. Fabbro, A. Goobar, D. E. Groom, I. M. Hook, A. G. Kim, M. Y. Kim, J. C. Lee, N. J. Nunes, R. Pain, C. R. Pennypacker, R. Quimby, C. Lidman, R. S. Ellis, M. Irwin, R. G. McMahon, P. Ruiz-Lapuente, N. Walton, B. Schaefer, B. J. Boyle, A. V. Filippenko, T. Matheson, A. S. Fruchter, N. Panagia, H. J. M.

Newberg, W. J. Couch, and T. S. C. Project. Measurements of Ω and Λ from 42 High-Redshift Supernovae. *ApJ*, 517:565–586, June 1999.

[12] A. G. Riess, A. V. Filippenko, P. Challis, A. Clocchiatti, A. Diercks, P. M. Garnavich, R. L. Gilliland, C. J. Hogan, S. Jha, R. P. Kirshner, B. Leibundgut, M. M. Phillips, D. Reiss, B. P. Schmidt, R. A. Schommer, R. C. Smith, J. Spyromilio, C. Stubbs, N. B. Suntzeff, and J. Tonry. Observational Evidence from Supernovae for an Accelerating Universe and a Cosmological Constant. *The Astronomical Journal*, 116:1009–1038, September 1998.

[13] N. A. Bahcall, J. P. Ostriker, S. Perlmutter, and P. J. Steinhardt. The Cosmic Triangle: Revealing the State of the Universe. *Science*, 284:1481, May 1999.

[14] Steven Weinberg. The cosmological constant problem. *Rev. Mod. Phys.*, 61:1–23, Jan 1989.

[15] Michel Chevallier and David Polarski. Accelerating universes with scaling dark matter. *Int. J. Mod. Phys.*, D10:213–224, 2001.

[16] Eric V. Linder. Exploring the expansion history of the universe. *Phys. Rev. Lett.*, 90:091301, 2003.

[17] H. K. Jassal, J. S. Bagla, and T. Padmanabhan. WMAP constraints on low redshift evolution of dark energy. *Mon. Not. Roy. Astron. Soc.*, 356:L11–L16, 2005.

[18] Lei Feng and Tan Lu. A new equation of state for dark energy model. *Journal of Cosmology and Astroparticle Physics*, 2011(11):034, 2011.

[19] Ruth Lazkoz, Vincenzo Salzano, and Irene Sendra. Oscillations in the dark energy equation of state: New mcmc lessons. *Physics Letters B*, 694(3):198 – 208, 2010.

[20] Asantha R. Cooray and Dragan Huterer. Gravitational lensing as a probe of quintessence. *Astrophys. J.*, 513:L95–L98, 1999.

[21] Chao-Jun Feng, Xian-Yong Shen, Ping Li, and Xin-Zhou Li. A New Class of Parametrization for Dark Energy without Divergence. *JCAP*, 1209:023, 2012.

[22] C. Wetterich. Cosmology and the Fate of Dilatation Symmetry. *Nucl. Phys.*, B302:668–696, 1988.

[23] Bharat Ratra and P. J. E. Peebles. Cosmological Consequences of a Rolling Homogeneous Scalar Field. *Phys. Rev.*, D37:3406, 1988.

[24] Yasunori Fujii. Origin of the Gravitational Constant and Particle Masses in Scale Invariant Scalar - Tensor Theory. *Phys. Rev.*, D26:2580, 1982.

[25] L. H. Ford. COSMOLOGICAL CONSTANT DAMPING BY UNSTABLE SCALAR FIELDS. *Phys. Rev.*, D35:2339, 1987.

[26] Yasunosi Fujii and Tsuyoshi Nishioka. Model of a Decaying Cosmological Constant. *Phys. Rev.*, D42:361–370, 1990.

[27] Takeshi Chiba, Naoshi Sugiyama, and Takashi Nakamura. Cosmology with x matter. *Mon. Not. Roy. Astron. Soc.*, 289:L5–L9, 1997.

[28] Sean M. Carroll. Quintessence and the rest of the world. *Phys. Rev. Lett.*, 81:3067–3070, 1998.

[29] R. R. Caldwell. A Phantom menace? *Phys. Lett.*, B545:23–29, 2002.

[30] T. Padmanabhan and T. Roy Choudhury. Can the clustered dark matter and the smooth dark energy arise from the same scalar field? *Phys. Rev.*, D66:081301, 2002.

[31] T. Padmanabhan. Accelerated expansion of the universe driven by tachyonic matter. *Phys. Rev.*, D66:021301, 2002.

[32] Ashoke Sen. Tachyon matter. *JHEP*, 07:065, 2002.

[33] Ashoke Sen. Rolling tachyon. *JHEP*, 04:048, 2002.

[34] E. Komatsu, J. Dunkley, M. R. Nolta, C. L. Bennett, B. Gold, G. Hinshaw, N. Jarosik, D. Larson, M. Limon, L. Page, D. N. Spergel, M. Halpern, R. S. Hill, A. Kogut, S. S. Meyer, G. S. Tucker, J. L. Weiland, E. Wollack, and E. L. Wright. Five-Year Wilkinson Microwave Anisotropy Probe Observations: Cosmological Interpretation. *ApJS*, 180:330–376, February 2009.

[35] Mike Guidry and Bronson Messer. The physics and astrophysics of type ia supernova explosions. *Frontiers of Physics*, 8(2):111–115, Apr 2013.

[36] M. Sullivan. *Type Ia Supernovae and Cosmology*, pages 59–97. Springer Berlin Heidelberg, Berlin, Heidelberg, 2010.

[37] M. M. Phillips. The absolute magnitudes of Type IA supernovae. *ApJL*, 413:L105–L108, August 1993.

[38] R. Tripp. A two-parameter luminosity correction for Type IA supernovae. *A&A*, 331:815–820, March 1998.

[39] N. Suzuki, D. Rubin, C. Lidman, G. Aldering, R. Amanullah, K. Barbary, L. F. Barrientos, J. Botyanszki, M. Brodwin, N. Connolly, K. S. Dawson, A. Dey, M. Doi, M. Donahue, S. Deustua, P. Eisenhardt, E. Ellingson, L. Faccioli, V. Fadeyev, H. K. Fakhouri, A. S. Fruchter, D. G. Gilbank, M. D. Gladders, G. Goldhaber, A. H. Gonzalez, A. Goobar, A. Gude, T. Hattori, H. Hoekstra, E. Hsiao, X. Huang, Y. Ihara, M. J. Jee, D. Johnston, N. Kashikawa, B. Koester, K. Konishi, M. Kowalski, E. V. Linder, L. Lubin, J. Melbourne, J. Meyers, T. Morokuma, F. Munshi, C. Mullis, T. Oda, N. Panagia, S. Perlmutter, M. Postman, T. Pritchard, J. Rhodes, P. Ripoche, P. Rosati, D. J. Schlegel, A. Spadafora, S. A. Stanford, V. Stanishev, D. Stern, M. Strovink, N. Takanashi, K. Tokita, M. Wagner, L. Wang, N. Yasuda, H. K. C. Yee, and T. Supernova Cosmology Project. The Hubble Space Telescope Cluster Supernova Survey. V. Improving the Dark-energy Constraints above z $>$ 1 and Building an Early-type-hosted Supernova Sample. *ApJ*, 746:85, February 2012.

[40] Bruce A. Bassett and Renee Hlozek. Baryon Acoustic Oscillations. 2009.

[41] D. J. Eisenstein and W. Hu. Baryonic Features in the Matter Transfer Function. *ApJ*, 496:605–614, March 1998.

[42] E. Komatsu, J. Dunkley, M. R. Nolta, C. L. Bennett, B. Gold, G. Hinshaw, N. Jarosik, D. Larson, M. Limon, L. Page, D. N. Spergel, M. Halpern, R. S. Hill, A. Kogut, S. S. Meyer, G. S. Tucker, J. L. Weiland, E. Wollack, and E. L. Wright. Five-Year Wilkinson Microwave Anisotropy Probe Observations: Cosmological Interpretation. *ApJS*, 180:330–376, February 2009.

[43] Masatoshi Shoji, Donghui Jeong, and Eiichiro Komatsu. Extracting Angular Diameter Distance and Expansion Rate of the Universe from Two-dimensional Galaxy Power Spectrum at High Redshifts: Baryon Acoustic Oscillation Fitting versus Full Modeling. *Astrophys. J.*, 693:1404–1416, 2009.

[44] Daniel J. Eisenstein, Idit Zehavi, David W. Hogg, Roman Scoccimarro, Michael R. Blanton, Robert C. Nichol, Ryan Scranton, Hee-Jong Seo, Max Tegmark, Zheng Zheng, Scott F. Anderson, Jim Annis, Neta Bahcall, Jon Brinkmann, Scott Burles, Francisco J. Castander, Andrew Connolly, Istvan Csabai, Mamoru Doi, Masataka Fukugita, Joshua A. Frieman, Karl Glazebrook, James E. Gunn, John S. Hendry, Gregory Hennessy, Zeljko Ivezi, Stephen Kent, Gillian R. Knapp, Huan Lin, Yeong-Shang Loh, Robert H. Lupton, Bruce Margon, Timothy A. McKay, Avery Meiksin, Jeffery A. Munn, Adrian Pope, Michael W. Richmond, David Schlegel, Donald P. Schneider, Kazuhiro Shimasaku, Christopher Stoughton, Michael A. Strauss, Mark SubbaRao, Alexander S. Szalay, Istvn Szapudi, Douglas L. Tucker, Brian Yanny,

and Donald G. York. Detection of the baryon acoustic peak in the large-scale correlation function of sdss luminous red galaxies. *The Astrophysical Journal*, 633(2):560, 2005.

[45] Will J. Percival, Shaun Cole, Daniel J. Eisenstein, Robert C. Nichol, John A. Peacock, Adrian C. Pope, and Alexander S. Szalay. Measuring the Baryon Acoustic Oscillation scale using the SDSS and 2dFGRS. *Mon. Not. Roy. Astron. Soc.*, 381:1053–1066, 2007.

[46] W. J. Percival, B. A. Reid, D. J. Eisenstein, N. A. Bahcall, T. Budavari, J. A. Frieman, M. Fukugita, J. E. Gunn, Ž. Ivezić, G. R. Knapp, R. G. Kron, J. Loveday, R. H. Lupton, T. A. McKay, A. Meiksin, R. C. Nichol, A. C. Pope, D. J. Schlegel, D. P. Schneider, D. N. Spergel, C. Stoughton, M. A. Strauss, A. S. Szalay, M. Tegmark, M. S. Vogeley, D. H. Weinberg, D. G. York, and I. Zehavi. Baryon acoustic oscillations in the Sloan Digital Sky Survey Data Release 7 galaxy sample. *MNRAS*, 401:2148–2168, February 2010.

[47] F. Beutler, C. Blake, M. Colless, D. H. Jones, L. Staveley-Smith, L. Campbell, Q. Parker, W. Saunders, and F. Watson. The 6dF Galaxy Survey: baryon acoustic oscillations and the local Hubble constant. *MNRAS*, 416:3017–3032, October 2011.

[48] C. Blake, E. A. Kazin, F. Beutler, T. M. Davis, D. Parkinson, S. Brough, M. Colless, C. Contreras, W. Couch, S. Croom, D. Croton, M. J. Drinkwater, K. Forster, D. Gilbank, M. Gladders, K. Glazebrook, B. Jelliffe, R. J. Jurek, I.-H. Li, B. Madore, D. C. Martin, K. Pimbblet, G. B. Poole, M. Pracy, R. Sharp, E. Wisnioski, D. Woods, T. K. Wyder, and H. K. C. Yee. The WiggleZ Dark Energy Survey: mapping the distance-redshift relation with baryon acoustic oscillations. *MNRAS*, 418:1707–1724, December 2011.

[49] N. G. Busca, T. Delubac, J. Rich, S. Bailey, A. Font-Ribera, D. Kirkby, J.-M. Le Goff, M. M. Pieri, A. Slosar, É. Aubourg, J. E. Bautista, D. Bizyaev, M. Blomqvist, A. S. Bolton, J. Bovy, H. Brewington, A. Borde, J. Brinkmann, B. Carithers, R. A. C. Croft, K. S. Dawson, G. Ebelke, D. J. Eisenstein, J.-C. Hamilton, S. Ho, D. W. Hogg, K. Honscheid, K.-G. Lee, B. Lundgren, E. Malanushenko, V. Malanushenko, D. Margala, C. Maraston, K. Mehta, J. Miralda-Escudé, A. D. Myers, R. C. Nichol, P. Noterdaeme, M. D. Olmstead, D. Oravetz, N. Palanque-Delabrouille, K. Pan, I. Pâris, W. J. Percival, P. Petitjean, N. A. Roe, E. Rollinde, N. P. Ross, G. Rossi, D. J. Schlegel, D. P. Schneider, A. Shelden, E. S. Sheldon, A. Simmons, S. Snedden, J. L. Tinker, M. Viel, B. A. Weaver, D. H. Weinberg,

M. White, C. Yèche, and D. G. York. Baryon acoustic oscillations in the Lyα forest of BOSS quasars. *A&A*, 552:A96, April 2013.

[50] C. Blake, S. Brough, M. Colless, C. Contreras, W. Couch, S. Croom, D. Croton, T. M. Davis, M. J. Drinkwater, K. Forster, D. Gilbank, M. Gladders, K. Glazebrook, B. Jelliffe, R. J. Jurek, I.-h. Li, B. Madore, D. C. Martin, K. Pimbblet, G. B. Poole, M. Pracy, R. Sharp, E. Wisnioski, D. Woods, T. K. Wyder, and H. K. C. Yee. The WiggleZ Dark Energy Survey: joint measurements of the expansion and growth history at z < 1. *MNRAS*, 425:405–414, September 2012.

[51] Omer Farooq, Sara Crandall, and Bharat Ratra. Binned Hubble parameter measurements and the cosmological deceleration-acceleration transition. *Phys. Lett.*, B726:72–82, 2013.

[52] Omer Farooq and Bharat Ratra. Hubble parameter measurement constraints on the cosmological deceleration-acceleration transition redshift. *Astrophys. J.*, 766:L7, 2013.

[53] Joan Simon, Licia Verde, and Raul Jimenez. Constraints on the redshift dependence of the dark energy potential. *Phys. Rev.*, D71:123001, 2005.

[54] D. Stern, R. Jimenez, L. Verde, S. A. Stanford, and M. Kamionkowski. Cosmic Chronometers: Constraining the Equation of State of Dark Energy. II. A Spectroscopic Catalog of Red Galaxies in Galaxy Clusters. *ApJS*, 188:280–289, May 2010.

[55] M. Moresco, A. Cimatti, R. Jimenez, L. Pozzetti, G. Zamorani, M. Bolzonella, J. Dunlop, F. Lamareille, M. Mignoli, H. Pearce, P. Rosati, D. Stern, L. Verde, E. Zucca, C. M. Carollo, T. Contini, J.-P. Kneib, O. Le Fèvre, S. J. Lilly, V. Mainieri, A. Renzini, M. Scodeggio, I. Balestra, R. Gobat, R. McLure, S. Bardelli, A. Bongiorno, K. Caputi, O. Cucciati, S. de la Torre, L. de Ravel, P. Franzetti, B. Garilli, A. Iovino, P. Kampczyk, C. Knobel, K. Kovač, J.-F. Le Borgne, V. Le Brun, C. Maier, R. Pelló, Y. Peng, E. Perez-Montero, V. Presotto, J. D. Silverman, M. Tanaka, L. A. M. Tasca, L. Tresse, D. Vergani, O. Almaini, L. Barnes, R. Bordoloi, E. Bradshaw, A. Cappi, R. Chuter, M. Cirasuolo, G. Coppa, C. Diener, S. Foucaud, W. Hartley, M. Kamionkowski, A. M. Koekemoer, C. López-Sanjuan, H. J. McCracken, P. Nair, P. Oesch, A. Stanford, and N. Welikala. Improved constraints on the expansion rate of the Universe up to z ˜ 1.1 from the spectroscopic evolution of cosmic chronometers. *J. Cosmology Astropart. Phys.*, 8:006, August 2012.

[56] Kyle M. Wilson, Gang Chen, and Bharat Ratra. Supernova ia and galaxy cluster gas mass fraction constraints on dark energy. *Mod. Phys. Lett.*, A21:2197–2204, 2006.

[57] C.-H. Chuang and Y. Wang. Modelling the anisotropic two-point galaxy correlation function on small scales and single-probe measurements of H(z), D_A(z) and f(z)σ_8(z) from the Sloan Digital Sky Survey DR7 luminous red galaxies. *MNRAS*, 435:255–262, October 2013.

[58] Ashutosh Tripathi, Archana Sangwan, and H. K. Jassal. Dark energy equation of state parameter and its evolution at low redshift. *JCAP*, 1706(06):012, 2017.

[59] Pedro G. Ferreira and Michael Joyce. Structure formation with a selftuning scalar field. *Phys. Rev. Lett.*, 79:4740–4743, 1997.

[60] Edmund J. Copeland, Andrew R Liddle, and David Wands. Exponential potentials and cosmological scaling solutions. *Phys. Rev.*, D57:4686–4690, 1998.

[61] R. R. Caldwell, Rahul Dave, and Paul J. Steinhardt. Cosmological imprint of an energy component with general equation of state. *Phys. Rev. Lett.*, 80:1582–1585, 1998.

[62] Ivaylo Zlatev, Li-Min Wang, and Paul J. Steinhardt. Quintessence, cosmic coincidence, and the cosmological constant. *Phys. Rev. Lett.*, 82:896–899, 1999.

[63] Takeshi Chiba, Takahiro Okabe, and Masahide Yamaguchi. Kinetically driven quintessence. *Phys. Rev.*, D62:023511, 2000.

[64] C. Armendariz-Picon, Viatcheslav F. Mukhanov, and Paul J. Steinhardt. A Dynamical solution to the problem of a small cosmological constant and late time cosmic acceleration. *Phys. Rev. Lett.*, 85:4438–4441, 2000.

[65] Archana Sangwan, Ankan Mukherjee, and H. K. Jassal. Reconstructing the dark energy potential. *JCAP*, 1801(01):018, 2018.

[66] Alexander Yu. Kamenshchik, Ugo Moschella, and Vincent Pasquier. An Alternative to quintessence. *Phys. Lett.*, B511:265–268, 2001.

[67] Kazuharu Bamba, Salvatore Capozziello, Shin'ichi Nojiri, and Sergei D. Odintsov. Dark energy cosmology: the equivalent description via different theoretical models and cosmography tests. *Astrophys. Space Sci.*, 342:155–228, 2012.

[68] Archana Sangwan, Ashutosh Tripathi, and H. K. Jassal. Observational constraints on quintessence models of dark energy. 2018.

[69] R. J. Scherrer and A. A. Sen. Thawing quintessence with a nearly flat potential. *Phys. Rev. D*, 77(8):083515, April 2008.

[70] Sourish Dutta and Robert J. Scherrer. Slow-roll freezing quintessence. *Phys. Lett.*, B704:265–269, 2011.

[71] Paul J. Steinhardt, Li-Min Wang, and Ivaylo Zlatev. Cosmological tracking solutions. *Phys. Rev.*, D59:123504, 1999.

[72] Gaveshna Gupta, Raghavan Rangarajan, and Anjan A. Sen. Thawing quintessence from the inflationary epoch to today. *Phys. Rev.*, D92(12):123003, 2015.

[73] Takeshi Chiba. Slow-Roll Thawing Quintessence. *Phys. Rev.*, D79:083517, 2009. [Erratum: Phys. Rev.D80,109902(2009)].

[74] Robert J. Scherrer. Dark energy models in the w-w' plane. *Phys. Rev.*, D73:043502, 2006.

[75] Carlo Schimd, Ismael Tereno, Jean-Philippe Uzan, Yannick Mellier, Ludovic van Waerbeke, Elisabetta Semboloni, Henk Hoekstra, Liping Fu, and Alain Riazuelo. Tracking quintessence by cosmic shear - constraints from virmos-descart and cfhtls and future prospects. *Astron. Astrophys.*, 463:405–421, 2007.

[76] Martin Sahlen, Andrew R Liddle, and David Parkinson. Quintessence reconstructed: New constraints and tracker viability. *Phys. Rev.*, D75:023502, 2007.

[77] Takeshi Chiba. W and w' of scalar field models of dark energy. *Phys. Rev.*, D73:063501, 2006. [Erratum: Phys. Rev.D80,129901(2009)].

[78] Pedro G. Ferreira and Michael Joyce. Cosmology with a primordial scaling field. *Phys. Rev.*, D58:023503, 1998.

[79] Renata Kallosh, Jan Kratochvil, Andrei D. Linde, Eric V. Linder, and Marina Shmakova. Observational bounds on cosmic doomsday. *JCAP*, 0310:015, 2003.

[80] Andrei D. Linde. Axions in inflationary cosmology. *Phys. Lett.*, B259:38–47, 1991.

[81] Andrei D. Linde. Hybrid inflation. *Phys. Rev.*, D49:748–754, 1994.

[82] Emilio Elizalde, Shin'ichi Nojiri, Sergei D. Odintsov, Diego Saez-Gomez, and Valerio Faraoni. Reconstructing the universe history, from inflation to acceleration, with phantom and canonical scalar fields. *Phys. Rev.*, D77:106005, 2008.

[83] Edmund J. Copeland, M. Sami, and Shinji Tsujikawa. Dynamics of dark energy. *Int. J. Mod. Phys.*, D15:1753–1936, 2006.

[84] Bruce A. Bassett, Pier Stefano Corasaniti, and Martin Kunz. The Essence of quintessence and the cost of compression. *Astrophys. J.*, 617:L1–L4, 2004.

[85] A. de la Macorra and G. Piccinelli. General scalar fields as quintessence. *Phys. Rev.*, D61:123503, 2000.

[86] S. C. C. Ng, N. J. Nunes, and Francesca Rosati. Applications of scalar attractor solutions to cosmology. *Phys. Rev.*, D64:083510, 2001.

[87] Pier Stefano Corasaniti and E. J. Copeland. A Model independent approach to the dark energy equation of state. *Phys. Rev.*, D67:063521, 2003.

[88] R. R. Caldwell and Eric V. Linder. The Limits of quintessence. *Phys. Rev. Lett.*, 95:141301, 2005.

[89] Eric V. Linder. The paths of quintessence. *Phys. Rev.*, D73:063010, 2006.

[90] Robert R. Caldwell, Marc Kamionkowski, and Nevin N. Weinberg. Phantom energy and cosmic doomsday. *Phys. Rev. Lett.*, 91:071301, 2003.

[91] Parampreet Singh, M. Sami, and Naresh Dadhich. Cosmological dynamics of phantom field. *Phys. Rev.*, D68:023522, 2003.

[92] M. Sami and Alexey Toporensky. Phantom field and the fate of universe. *Mod. Phys. Lett.*, A19:1509, 2004.

[93] Mariusz P. Dabrowski, Tomasz Stachowiak, and Marek Szydlowski. Phantom cosmologies. *Phys. Rev.*, D68:103519, 2003.

[94] Jian-Gang Hao and Xin-zhou Li. Phantom cosmic dynamics: Tracking attractor and cosmic doomsday. *Phys. Rev.*, D70:043529, 2004.

[95] Shin'ichi Nojiri and Sergei D. Odintsov. Quantum de Sitter cosmology and phantom matter. *Phys. Lett.*, B562:147–152, 2003.

[96] and. On the avoidance of singularities in c-field cosmology. *Proceedings of the Royal Society of London A: Mathematical, Physical and Engineering Sciences*, 278(1375):465–478, 1964.

[97] and. The c-field as a direct particle field. *Proceedings of the Royal Society of London A: Mathematical, Physical and Engineering Sciences*, 282(1389):178–183, 1964.

[98] H. A. Rizwan ul and S. Unnikrishnan. Effect of dark energy sound speed and equation of state on CDM power spectrum. *J. Phys. Conf. Ser.*, 484:012048, 2014.

[99] Bharat Ratra. Inflation in an Exponential Potential Scalar Field Model. *Phys. Rev.*, D45:1913–1952, 1992.

[100] Robert J. Scherrer. Mapping the Chevallier-Polarski-Linder parametrization onto Physical Dark Energy Models. *Phys. Rev.*, D92(4):043001, 2015.

[101] G. Pantazis, S. Nesseris, and L. Perivolaropoulos. Comparison of thawing and freezing dark energy parametrizations. *Phys. Rev.*, D93(10):103503, 2016.

[102] F. James. *Statistical Methods in Experimental Physics*. World Scientific, 2006.

[103] L. Verde. Statistical Methods in Cosmology. In G. Wolschin, editor, *Lecture Notes in Physics, Berlin Springer Verlag*, volume 800 of *Lecture Notes in Physics, Berlin Springer Verlag*, pages 147–177, March 2010.

[104] William H. Press, Brian P. Flannery, Saul A. Teukolsky, and William T. Vetterling. *Numerical Recipes in C: The Art of Scientific Computing*. Cambridge University Press, New York, NY, USA, 1988.

[105] Muhammad Omer Farooq. *Observational constraints on dark energy cosmological model parameters*. PhD thesis, Kansas State U., 2013.